Department of Physics and Astronomy
Ruperto-Carola University of Heidelberg

MASTER THESIS

in Physics

submitted by

Maximilian Papst

born in Mannheim

2019

Development of a method for quantitative imaging of air-water gas exchange

This Master thesis has been carried out by Maximilian Papst
at the Institute for Environmental Physics and
the Heidelberg Collaboratory for Image Processing
under the supervision of
Prof. Dr. Bernd Jähne

Abstract

Using a fluorescent pH indicator (pyranine), a new measurement method to investigate the exchange of a soluble alkaline gas (ammonia) from air to water was developed. Key feature of the method is that a linear relationship between the concentrations of the dissolved gas and the alkaline form of the indicator, that is selectively excited to fluorescence in the water-side mass boundary layer, is established by using a high total concentration of the indicator (10^{-4} mol/l) and a pH value of 6. This relationship was verified with experiments at the Heidelberg linear wind-wave tunnel at a fixed wind speed. For different, constant gas fluxes into the water, the intensity of the fluorescence induced by LED illumination on a two-dimensional patch of the wind-driven, wavy water surface was imaged at 400 Hz by three cameras from below and one camera from above with a spatial resolution of 140 µm/px and 167 µm/px, respectively. With the verified relationship, the fluorescence signal could be used to obtain horizontally resolved, quantitative information on local changes in the concentration of a dissolved gas in the water-side mass boundary layer for the first time. During the experiments, also a fluorescence profile created by a focused laser beam was imaged at 800 Hz by a camera with a spatial resolution of 5.8 µm/px to observe vertical transport processes.

Zusammenfassung

Unter Verwendung eines fluoreszierenden pH-Indikators (Pyranin) wurde eine neue Messmethode zur Untersuchung des Austauschs eines wasserlöslichen alkalischen Gases (Ammoniak) von Luft zu Wasser entwickelt. Kernelement dieser Methode ist, dass eine lineare Beziehung zwischen den Konzentrationen des gelösten Gases und der alkalischen Form des Indikators, die in der wasserseitigen Massengrenzschicht selektiv zur Fluoreszenz angeregt wird, durch eine hohe Gesamtkonzentration des Indikators (10^{-4} mol/l) und einen pH Wert von 6 hergestellt wird. Diese Beziehung wurde mit Experimenten am linearen Wind-Wellen Kanal in Heidelberg bei einer festen Windgeschwindigkeit verifiziert. Mithilfe von drei Kameras unterhalb und einer Kamera oberhalb des Kanals mit einer räumlichen Auflösung von je 140 µm/px und 167 µm/px wurden bei einer Frequenz von 400 Hz Bilder der Fluoreszenz, angeregt durch LED Beleuchtung der windgetriebenen welligen Wasseroberfläche, für unterschiedliche, konstante Gasflüsse in das Wasser aufgezeichnet. Mithilfe der verifizierten Beziehung konnten aus dem Fluoreszenzsignal erstmals horizontal aufgelöste, quantitative Informationen über lokale Konzentrationsänderungen eines gelösten Gases in der wasserseitigen Massengrenzschicht gewonnen werden. In den Experimenten wurden zudem mithilfe einer Kamera mit einer Auflösung von 5.8 µm/px Bilder eines von einem fokussierten Laserstrahl erzeugten Fluoreszenzprofils bei einer Frequenz von 800 Hz aufgenommen, um vertikale Transportprozesse zu beobachten.

Contents

1. Introduction

The exchange of gases between the oceans and the atmosphere of the earth plays a key role in the understanding and the prediction of the global climate. The radiative budget of the earth's atmosphere is directly linked to its chemical composition [Myhre, 2013]. In this context, the greenhouse gas carbon dioxide (CO_2) is of special importance. The oceans constitute a huge reservoir for atmospheric CO_2 and act also as a net sink by taking up 30% to 40% of the fossil fuel-produced carbon dioxide [Donelan and Wanninkhof, 2002]. The uptake leads to an increasing acidification of the oceans with consequences for the aquatic ecosystems like the die off of coral reefs [Richmond and Wolanski, 2011]. Thus, the knowledge of gas exchange processes between the oceans and the atmosphere, that are part of global chemical cycles, contributes to the prediction of environmental changes.

The gas exchange at the ocean surface is controlled by the concentration difference between the air and the water side and the transfer velocity which is a measure for the speed with which gases are transported through a thin ($50\,\mu m - 200\,\mu m$) water-side mass boundary layer. The transfer velocity is influenced by a variety of different factors. Wind blowing over the water surface generates waves and near-surface turbulence including the breaking of waves and bubble entrainment, which greatly enlarge the transfer velocity (see e.g. [Wanninkhof et al., 2009]). Other influencing factors are the distance over which the wind has blown and the presence of surface films which damp waves. Due to the complexity of the gas exchange process, an universal physically-based model still does not exist. As wind speed data are globally available, semi-empirical parameterizations of the transfer velocity as a function of the wind speed are used in climate models [T. Ho et al., 2011].

Experiments on the ocean are challenging because of a high spatial and temporal variability of the wind speed and the wave field. In contrast, gas exchange can be investigated in a wind-wave tunnel under controlled conditions. A common approach to infer the transfer velocity is to measure the air-side and the water-side concentrations of the trace gas that is exchanged, making use of mass balance methods. Besides, imaging techniques based on fluorescent pH indicators, that are dissolved in the water, are powerful to obtain local information on the exchange processes. The used indicators have typically an acidic and an alkaline form of which one is selectively excited to fluorescence. The exchange of a gas that reacts in the water as an acid or a base and changes the pH value is made visible by the fluorescence of the excited form of the indicator. Two important measurement techniques that make use of such indicators have been established.

For the so called boundary layer imaging (BLI) method developed by [Kräuter et al., 2014], the water surface is illuminated horizontally such that the water-side mass boundary layer is made visible by the fluorescence of the excited form of the indicator. The depth-integrated fluorescence is imaged by cameras. The method is designed such that the fluorescence intensity is constant over depth within the boundary layer thickness, independent of the concentration of the trace gas, and zero outside. With this method, the small-scale turbulent processes close to the water surface, that influence the gas exchange, were investigated by [Kräuter, 2015] and [Klein, 2019] in wind-wave tunnels.

For the laser-induced fluorescence (LIF) method (see e.g. [Herzog, 2010]), a vertical laser beam is used to excite fluorescence close to the water surface. A high-resolution camera images the resulting fluorescence profile in the mass boundary layer from the side to infer vertical concentration profiles of the trace gas.

The novel measurement method developed in this study is based on the previously employed BLI method and aims to image air-water gas transfer quantitatively at a wind-driven, wavy water surface. The total concentration of the used fluorescent pH indicator is adjusted such that the fluorescence intensity over depth now depends on the local concentration of the trace gas. This enables one not only to observe the turbulent processes and to determine where the gas has entered the water, as it was possible previously, but also allows for the acquisition of quantitative information on the concentration of the gas. The present thesis focuses on the experimental verification of the method using imaging and spectroscopic techniques, so that the method is ready to use for further experiments. Apart from an imaging setup for the realization of the modified BLI method, also a LIF setup is employed to gain information on vertical transport processes.

Chapter 2 gives a theoretical introduction to air-water gas exchange. As the fluorescent pH indicator and its optical properties play a central role, basics on chemical reactions as well as on absorption and fluorescence are given. In Chap. 3 the developed measurement method is presented and the used chemical components are introduced. Moreover, mass balance methods are addressed. In Chap. 4, details on the the wind-wave tunnel used for the gas exchange experiments are given. The imaging setups for the BLI and the LIF method are discussed. The calibration of the measurement setup is presented in Chap. 5. It is shown how the concentration of the form of the indicator that is excited to fluorescence can be related to the fluorescence intensity. In Chap. 6, the conducted gas exchange experiments are addressed. The processing of the images recorded with the BLI and the LIF setup is explained in Chap. 7. In Chap. 8, the results of the experiments are presented. Chapter 9 comprises a summary of the obtained results and conclusions for future experiments.

2. Theoretical background

This chapter provides an overview of the most important concepts and mathematical descriptions concerning air-water exchange processes. First of all, the underlying mechanisms governing the transport of trace gas particles as well as quantities like momentum and heat are discussed. The next section addresses air-water gas transfer in more detail by introducing basic quantities to parametrize the relevant processes. After that, basic terms concerning chemical reactions are introduced, where special emphasis is put on pH indicators and the influence of reactions on the solubility of a gas. Finally, a macroscopic description of light absorption is given and the phenomenon of fluorescence is explained conceptually.

2.1 Transport phenomena

Fundamentally, the transfer of particles, momentum or heat in a fluid medium can be caused by directed motion called advection or by random motion including molecular diffusion and turbulent flow. In the following, molecular diffusion and advection will be addressed first, while turbulence, which requires a separate treatment, will be discussed afterwards. Throughout this section, the fluid is assumed to be incompressible and to have a non-vanishing viscosity.

2.1.1 Molecular diffusion and advection

Considering the mass transport of particles, molecular diffusion results from the random movement of particles due to their thermal energy, which exhibits the stochastic nature of the random walk [Pearson, 1905]. The process is driven by spatial concentration differences and gives rise to a net flux density $\boldsymbol{j}_{\mathrm{c,diff}}$ from regions of higher to regions of lower concentration. This relation is described by the following diffusion equation, known as **Fick's first law** [Fick, 1855]:

$$\boldsymbol{j}_{\mathrm{c,diff}} = -D\boldsymbol{\nabla}c. \tag{2.1}$$

The concentration gradient is denoted by $\boldsymbol{\nabla}c$. The diffusion constant D can be expressed as

$$D = \frac{1}{3}vl. \tag{2.2}$$

It depends on the mean thermal velocity v and the mean free path l of the diffusing particles. The prefactor of 1/3 reflects the isotropy of the diffusion process in three spatial dimensions.

The temporal variation of the concentration c can be derived from the continuity equation without any sources and sinks

$$\frac{\partial c}{\partial t} + \boldsymbol{\nabla} \cdot \boldsymbol{j}_\mathrm{c} = 0, \tag{2.3}$$

by setting $\boldsymbol{j}_\mathrm{c} = \boldsymbol{j}_\mathrm{c,diff}$ to give

$$\frac{\partial c}{\partial t} = D\nabla^2 c, \tag{2.4}$$

with the Laplace operator ∇^2. Eq. 2.4 is known as **Fick's second law** [Fick, 1855]. If the fluid is in motion, an advective flux term $\boldsymbol{j}_\mathrm{c,adv} = \boldsymbol{u}c$, which is associated with the macroscopic (mean) flow of the fluid given by the velocity field $\boldsymbol{u}$, is added such that $\boldsymbol{j}_\mathrm{c} = \boldsymbol{j}_\mathrm{c,diff} + \boldsymbol{j}_\mathrm{c,adv}$. Under the assumption of an incompressible fluid with $\boldsymbol{\nabla} \cdot \boldsymbol{u} = 0$, this changes Eq. 2.4 to

$$\frac{\partial c}{\partial t} + \boldsymbol{u} \cdot \boldsymbol{\nabla} c = D\nabla^2 c, \tag{2.5}$$

which is also known as the **advection-diffusion equation**.

Remarkably, the transport of heat and momentum can be treated in analogy to Eq. 2.1 and Eq. 2.4 [Jähne and Haußecker, 1998]. The corresponding equations for heat read

$$\boldsymbol{j}_\mathrm{h,diff} = -\lambda_\mathrm{h} \boldsymbol{\nabla} T, \tag{2.6a}$$

$$\frac{\partial T}{\partial t} = \chi \nabla^2 T, \tag{2.6b}$$

with the thermal conductivity coefficient λ_h, the temperature T and the thermal diffusivity $\chi = \lambda_\mathrm{h}/(c_p \rho)$, where c_p denotes the specific heat at constant pressure and ρ the density of the fluid medium. Eq. 2.6a is called **Fourier's law**. If the fluid is in motion, an advective term is added in Eq. 2.6b as in Eq. 2.5.

To describe the diffusive momentum flux of an incompressible fluid, a one-dimensional flow in horizontal x-direction with a velocity gradient in vertical z-direction is considered. Due to the viscosity of the fluid, frictional forces are present, which allow vertical transport of horizontal momentum. This momentum flux $j_{\mathrm{m,diff},zx}$ is equivalent to shear stress in the fluid τ_{zx}, which is related to the vertical velocity gradient

by **Newton's law of viscosity**

$$\tau_{zx} = j_{\mathrm{m,diff},zx} = -\nu \frac{\partial(\rho u_x)}{\partial z} \tag{2.7}$$

in analogy to Eq. 2.1. The kinematic viscosity is denoted by ν. A general formulation of momentum transport and related (shear) stress is given by the stress tensor [Kundu et al., 2012]. The law of momentum conservation in a fluid is given by the **Navier-Stokes equation** [Roedel, 2000], here shown for incompressible fluids:

$$\frac{\partial \boldsymbol{u}}{\partial t} + (\boldsymbol{u} \cdot \boldsymbol{\nabla})\boldsymbol{u} = -\frac{1}{\rho}\boldsymbol{\nabla} p + \boldsymbol{f} + \nu \nabla^2 \boldsymbol{u}. \tag{2.8}$$

The acceleration of the fluid, expressed by the left-hand side of this equation, can be caused by pressure gradients $\boldsymbol{\nabla} p$ as well as external forces and shear stress, that are represented by the terms $\boldsymbol{f}$ and $\nu \nabla^2 \boldsymbol{u}$, respectively. Assuming no pressure gradients and no external forces, Eq. 2.8 simplifies to

$$\frac{\partial \boldsymbol{u}}{\partial t} + (\boldsymbol{u} \cdot \boldsymbol{\nabla})\boldsymbol{u} = \nu \nabla^2 \boldsymbol{u}, \tag{2.9}$$

which is equivalent to Eq. 2.5.

To compare the diffusion of momentum with the diffusion of a gas, the dimensionless **Schmidt number** is introduced as

$$\mathrm{Sc} = \frac{\nu}{D}. \tag{2.10}$$

Similarly, the dimensionless **Prandtl number** is defined as

$$\mathrm{Pr} = \frac{\nu}{\chi} \tag{2.11}$$

to quantify the difference in the effectiveness of momentum and heat transport. For most substances in air, the Sc and Pr numbers are about one. In water this is typically different. For instance, the Pr numbers in air and water are 0.71 and 7 [Schimpf, 2000], respectively. The Sc numbers of ammonia at 25 °C are 0.62 (air) and 610 (water) [Fogg and Sangster, 2003], differing by three orders of magnitude.

2.1.2 Turbulence and turbulent diffusion

From a macroscopic point of view, turbulent motion of a fluid medium can be characterized as chaotic, irregular and unpredictable in position and time. Typically, turbulent flow is associated with random fluctuations of the velocity field. Thus, it is enormously sensitive to initial and boundary conditions. A detailed mathematical description of turbulent motion is obviously difficult. A common approach is the

concept of eddies which occur at different length scales, ranging from a macroscale at which the fluid bulk is mixed by large streams to a microscale in the order of millimeters. According to Kolmogorov's theory on turbulence ([Kolmogorov, 1941], [Kolmogorov, 1962]) energy is passed in a cascade from larger to smaller eddies. The motion of the largest eddies at the macroscale supply energy, which is eventually dissipated by molecular friction due to viscosity at the microscale, represented by the smallest eddies. The range of scales between these to extrema where energy is neither produced nor annihilated, but transferred from larger to smaller scales is called **inertial subrange**.

A measure for the level of turbulent behavior is the **Reynolds number**

$$\mathrm{Re} = \frac{ul}{\nu}, \tag{2.12}$$

where u is the mean velocity, l a characteristic length scale, that needs to be defined in dependence of the considered system or problem, and ν the kinematic viscosity of the fluid [Stokes, 1850]. The Reynolds number represents the ratio of inertial forces to viscous forces. If the Reynolds number is smaller than a critical value $\mathrm{Re}_{\mathrm{crit}}$, which depends on the problem, the fluid flow is laminar overall. Turbulent behavior can still occur to some small degree, but is clearly suppressed in this regime. The smaller Re, the faster turbulent structures decay. If $\mathrm{Re} > \mathrm{Re}_{\mathrm{crit}}$, laminar flow becomes very sensitive to small disturbances, which build up and lead to a change into turbulent flow, where the velocity field is instationary.

In the following, it will be shown that turbulent transport can be described in analogy to molecular diffusion (Sec. 2.1.1), known as **turbulent diffusion**. However, it has to be noted that this is only valid under certain circumstances, e.g. close to boundaries, and if steady-state problems are considered or the flow is averaged over a long time period [Kundu et al., 2012]. Considering again the transport of gas and momentum, the concentration c and the velocity field $\boldsymbol{u}$ are split into a temporally averaged part, indicated by angle brackets with subscript t, and a fluctuating part, denoted by a prime symbol:

$$c = \langle c \rangle_t + c', \tag{2.13a}$$

$$\boldsymbol{u} = \langle \boldsymbol{u} \rangle_t + \boldsymbol{u}'. \tag{2.13b}$$

This is called **Reynolds decomposition**. For sufficiently long time periods, it can be assumed that the mean of the fluctuations vanishes, i.e. $\langle c' \rangle_t = 0$ and $\langle \boldsymbol{u}' \rangle_t = 0$. Similar considerations and the following derivation can be done for the turbulent transport of heat as well.

Considering a one-dimensional constant flow in horizontal x-direction and non-vanishing gradients only along the vertical z-direction, the following equations are obtained by

inserting Eqs. 2.13a and 2.13b into Eqs. 2.5 and 2.9, respectively:

$$0 = \frac{\partial \langle c \rangle_t}{\partial t} = \frac{\partial}{\partial z}\left(D \frac{\partial \langle c \rangle_t}{\partial z} - \langle c' u_z' \rangle_t \right), \tag{2.14a}$$

$$0 = \frac{\partial \langle u_x \rangle_t}{\partial t} = \frac{\partial}{\partial z}\left(\nu \frac{\partial \langle u_x \rangle_t}{\partial z} - \langle u_x' u_z' \rangle_t \right). \tag{2.14b}$$

A detailed derivation can be found in [Pope, 2009]. By setting the temporal derivatives of the averaged quantities to zero, a steady state is assumed. By combining these relations with the continuity equation Eq. 2.3, it follows that

$$j_{\mathrm{c},z} = -D \frac{\partial \langle c \rangle_t}{\partial z} + \langle c' u_z' \rangle_t, \tag{2.15a}$$

$$j_{\mathrm{m},zx} = \rho \left(-\nu \frac{\partial \langle u_x \rangle_t}{\partial z} + \langle u_x' u_z' \rangle_t \right) \tag{2.15b}$$

for the concentration and the momentum flux densities. If compared to Eqs. 2.1 and 2.7, where only molecular diffusion was considered, it becomes clear that the terms $\langle c' u_z' \rangle_t$ and $\rho \langle u_x' u_z' \rangle_t$ represent the turbulent part of the transport. This motivates the definition of **turbulent diffusion coefficients**

$$K_{\mathrm{c}}(z) = -\langle c' u_z' \rangle_t \Big/ \left(\frac{\partial \langle c \rangle_t}{\partial z} \right), \tag{2.16a}$$

$$K_{\mathrm{m}}(z) = -\langle u_x' u_z' \rangle_t \Big/ \left(\frac{\partial \langle u_x \rangle_t}{\partial z} \right), \tag{2.16b}$$

which can be used to rewrite Eqs. 2.15a and 2.15b in a unified form

$$j_{\mathrm{c},z} = -(D + K_{\mathrm{c}}(z)) \frac{\partial \langle c \rangle_t}{\partial z}, \tag{2.17a}$$

$$j_{\mathrm{m},zx} = -\rho(\nu + K_{\mathrm{m}}(z)) \frac{\partial \langle u_x \rangle_t}{\partial z}. \tag{2.17b}$$

In analogy to molecular diffusion a **turbulent Schmidt number** can be defined as

$$\mathrm{Sc}_{\mathrm{turb}} = \frac{K_{\mathrm{m}}}{K_{\mathrm{c}}}. \tag{2.18}$$

Without any boundaries, turbulent transport processes are generally much more efficient than molecular diffusion.

2.2 Air-water gas exchange

This section addresses the transport of a trace gas and momentum between air and water. The description presented in the following relies on the assumptions made in Sec. 2.1.2 concerning turbulent transport and the Eqs. 2.17a and 2.17b, where only the average of the concentration c and the velocity u_x is relevant. Therefore, the concentration and the velocity are understood to be averaged in the following, so that notation can be simplified by dropping the angle brackets. First, basic concepts and dominant transport mechanisms are discussed. After that, the most important parameters to quantify the transport are introduced, followed by a brief discussion on wind stress and waves. Moreover conceptual gas exchange models are presented.

2.2.1 Basic concepts

For the discussion of the gas exchange between air and water the (dimensionless Ostwald's) solubility α of a gas is introduced. This quantity is given by the ratio of the water-side concentration $c_{\mathrm{w,eq}}$ to the air-side concentration $c_{\mathrm{a,eq}}$ of a gas in thermodynamic equilibrium

$$\alpha = \frac{c_{\mathrm{w,eq}}}{c_{\mathrm{a,eq}}}. \tag{2.19}$$

This relation is also known as **Henry's law**. A solubility of $\alpha > 1$ is assumed in the following. As in Sec. 2.1.2, the problem is reduced to one dimension, given by the vertical z-direction and a situation $\alpha c_{\mathrm{a,b}} > c_{\mathrm{w,b}}$ outside the equilibrium is considered, where the air-side and the water-side bulk concentrations of the gas far away from the water surface are denoted by $c_{\mathrm{a,b}}$ and $c_{\mathrm{w,b}}$, respectively. Obviously, the concentration difference gives rise to a net concentration flux from the air phase across the water surface to the water phase. Under the assumption of a temporally constant concentration profile, as shown in Fig. 2.1 (a), the flux is constant over depth due to mass conservation. Since the flux is directed from air to water, the described process is called invasion, while the opposite situation where $\alpha c_{\mathrm{a,b}} < c_{\mathrm{w,b}}$ is known as evasion. The water surface at $z = 0$ represents an interface, which imposes a boundary condition on the concentration, relating the water-side surface concentration $c_{\mathrm{w,s}}$ to the air-side surface concentration $c_{\mathrm{a,s}}$ by Henry's law

$$c_{\mathrm{w,s}} = \alpha c_{\mathrm{a,s}}. \tag{2.20}$$

The requirement of thermodynamic equilibrium is justified by the constant concentration flux. The condition in Eq. 2.20 results in a jump of the concentration profile at the water surface.

The central idea for the description of the exchange process is that far away from the air-water interface the air bulk and the water bulk are well mixed by turbulence.

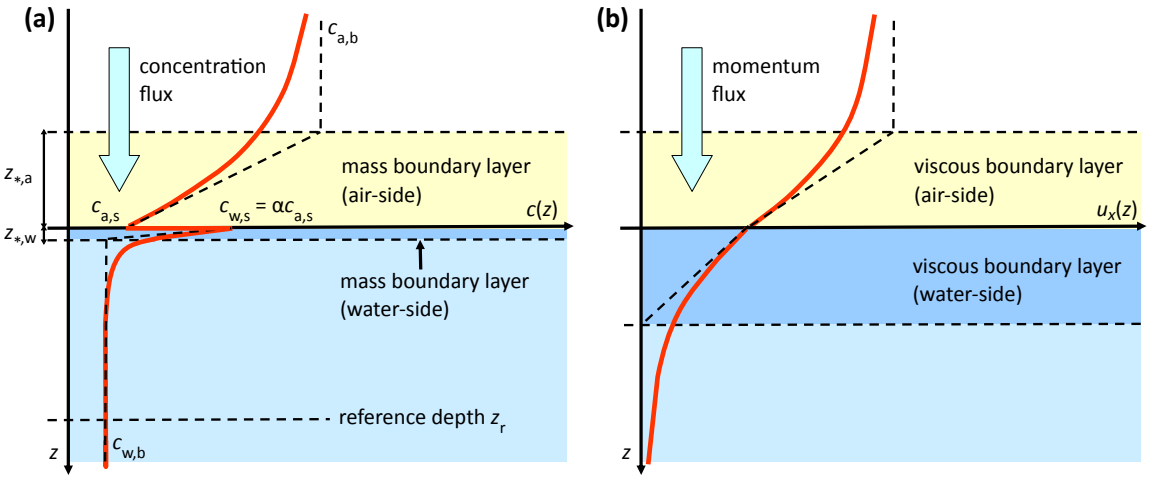

Fig. 2.1: Scheme of the air-water gas (a) and momentum (b) exchange, showing the arising air- and water-side boundary layer (modified after [Degreif, 2006]). (a) Typical concentration profile $c(z)$ of an invasion experiment, where the exchanged gas has a solubility $\alpha > 1$, which leads to a jump of the concentration at the water surface. (b) Velocity profile $u_x(z)$ associated with momentum flux from air to water.

As a consequence, a homogeneous concentration distribution quantified by $c_{\mathrm{a,b}}$ and $c_{\mathrm{w,b}}$ can be assumed here. It is common to define a reference depth z_{r} on the water side with the property that for $z > z_{\mathrm{r}}$ the concentration is assumed to be $c_{\mathrm{w,b}}$. In the bulk regions, turbulent transport is much more effective than molecular transport (see. Sec. 2.1.2), which means that $K_c \gg D$, where it has to be noted that in general these coefficients have different values in the air and in the water phase. The dominance of turbulent diffusion is reduced close to the so called **mass boundary layer**, which forms on each side of the water surface. With decreasing distance to the air-water interface, the size of turbulent eddies becomes smaller, as they cannot penetrate the interface because of the large difference in the densities of water and air ($\rho_{\mathrm{w}}/\rho_{\mathrm{a}} \approx 830$). Turbulent transport becomes less effecitve with decreasing eddy size and as a consequence must vanish at the water surface, which can be expressed as $K_{\mathrm{c}}(z = 0) = 0$ [Prandtl, 1957].

The boundary layers are defined as the regions where molecular diffusion becomes the dominant transport mechanism, i.e. $D > K_{\mathrm{c}}$. The distance from the interface to the region where $D \approx K_{\mathrm{c}}$ marks the transition between molecular and turbulent diffusion as the dominant transport process and is equivalent to the **mass boundary layer thickness** of the water- and air-side mass boundary layer, denoted by $z_{*,\mathrm{w}}$ and $z_{*,\mathrm{a}}$, respectively. A more precise definition will be given in Sec. 2.2.2. On the water side, the boundary layer has a typical thickness of $z_{*,\mathrm{w}} \approx 20\,\mu\mathrm{m} - 200\,\mu\mathrm{m}$ [Jähne et al., 1987]. Since molecular diffusion is less effective than turbulent trans-

port outside the boundary layers, it becomes clear that the largest part of the resistance to the flux lies in the boundary layers near the water surface. By looking at Eq. 2.17a and bearing in mind that the flux is constant over depth for a temporally constant concentration profile, it can be concluded that in these regions the concentration gradients are the largest. Consequently, the transport through the boundary layers controls the whole gas exchange process.

A typical velocity profile u_x for momentum flux directed from air to water is shown in Fig. 2.1 (b). As mentioned above in Sec. 2.1.1, momentum flux is equivalent to shear stress τ in a fluid medium. In the particular situation shown in Fig. 2.1 (b) tangential forcing, generated e.g. by wind blowing over the water surface, forms shear layers, which effectively transport horizontal momentum downwards into the water bulk. The corresponding shear stress τ_{zx} is given as the tangential force F_x per area A

$$\tau_{zx} = \frac{F_x}{A}. \tag{2.21}$$

Because of the no-slip condition, the velocity u_x is continuous across the water surface, while the transported momentum is not because the density of air is much smaller than the density of water ($\rho_\mathrm{a} \ll \rho_\mathrm{w}$). In analogy to the exchange of a gas, **viscous boundary layers** form on both sides of the water surface when momentum is transported. Both of them have a thickness of typically 600 µm − 2000 µm [Jähne and Haußecker, 1998], which is different from the gas exchange, where the thicknesses of the air-side and water-side mass boundary layer clearly differ by several orders of magnitude. The reason for this will become clear in the next section.

2.2.2 Gas exchange parameters

Starting from Eq. 2.17a, integration along the vertical concentration profile between two points z_1 and z_2 separated by $\Delta z = z_2 - z_1$ gives

$$\Delta c = c(z_2) - c(z_1) = -j_\mathrm{c} \int_{z_1}^{z_2} \frac{1}{D + K_\mathrm{c}(z)}\,\mathrm{d}z. \tag{2.22}$$

The quotient of the concentration difference and the flux density is interpreted as the **transfer resistance**

$$R = \frac{\Delta c}{j_\mathrm{c}} = -\int_{z_1}^{z_2} \frac{1}{D + K_\mathrm{c}(z)}\,\mathrm{d}z \tag{2.23}$$

in analogy to Ohm's law for electric circuits. The transfer resistance has units of time per distance and is a measure of the time which a gas needs to be transported

through a layer with thickness Δz. It can be directly seen from the definition in Eq. 2.23 that the transfer resistances of several neighboring layers are summed up to get the total resistance. For the resistances of the layers between $z_1 \leq z_2 \leq z_3$, this reads e.g.

$$R_{3,1} = R_{3,2} + R_{2,1}. \tag{2.24}$$

The mean velocity at which a gas is transported through the layer Δz is called **transfer velocity** k. It is given by the inverse of the transfer resistance R. With the definition of these two parameters, the concentration flux is commonly written as

$$j_\mathrm{c} = k\Delta c = \frac{\Delta c}{R}. \tag{2.25}$$

Using Eq. 2.24, it becomes clear that transfer velocities are added reciprocally

$$\frac{1}{k_{3,1}} = \frac{1}{k_{3,2}} + \frac{1}{k_{2,1}}. \tag{2.26}$$

By looking at Eq. 2.23 and following the argumentation concerning the relative dominance of molecular and turbulent diffusion in Sec. 2.2.1, it follows that on each side of the air-water interface the main transfer resistance lies in the mass boundary layer. Therefore, it is reasonable to look at the concentration differences between the bulk and the surface for each side of the interface to capture the main contribution to the resistance. Equating the fluxes $j_\mathrm{c,a}$ and $j_\mathrm{c,w}$ on the air and the water side

$$j_\mathrm{c,a} = \frac{c_\mathrm{a,b} - c_\mathrm{a,s}}{R_\mathrm{a}} = \frac{c_\mathrm{w,s} - c_\mathrm{w,b}}{R_\mathrm{w}} = j_\mathrm{c,w} \tag{2.27}$$

leads to

$$\frac{c_\mathrm{a,b} - c_\mathrm{w,b}/\alpha}{R_\mathrm{a} + R_\mathrm{w}/\alpha} = \frac{\alpha c_\mathrm{a,b} - c_\mathrm{w,b}}{R_\mathrm{w} + \alpha R_\mathrm{a}}, \tag{2.28}$$

by using the boundary condition Eq. 2.20. The left hand side of Eq. 2.28 represents the total flux across the interface from the air-side perspective, while the right hand side gives the water-side perspective on the flux. In the air-side view, the concentration of the water bulk is reduced by the factor α, while from the water-side point of view the concentration of the air bulk is magnified by α. Thus, it can be concluded that the total transfer resistances seen from the air and water phase are given by

$$R_\mathrm{tot,a} = R_\mathrm{a} + R_\mathrm{w}/\alpha, \tag{2.29a}$$

$$R_\mathrm{tot,w} = R_\mathrm{w} + \alpha R_\mathrm{a}, \tag{2.29b}$$

respectively. Analogously, the total transfer velocities are written as

$$k_\mathrm{tot,a} = \left(\frac{1}{k_\mathrm{a}} + \frac{1}{\alpha k_\mathrm{w}}\right)^{-1}, \tag{2.30a}$$

$$k_\mathrm{tot,w} = \left(\frac{1}{k_\mathrm{w}} + \frac{\alpha}{k_\mathrm{a}}\right)^{-1}. \tag{2.30b}$$

Now the importance of the solubility α for the air-water gas exchange becomes clear. For high solubilities $\alpha > 500$ the total transfer resistance is dominated by the air-side resistance. This is e.g. the case for ammonia (NH_3) and water vapor. However, most gases are sparingly soluble like carbon dioxide (CO_2), oxygen (O_2), and dinitrogen monoxide (N_2O). As a consequence, their transfer is controlled by the water side. There are also gases which are equally controlled by the air and the water phase. Besides, the solubility of some gases can be enlarged by water-side chemical reactions. More details on this will be given in Sec. 2.3. The solubility and the water-side Schmidt number are plotted in Fig. 2.2 for different gases as well as for heat and momentum.

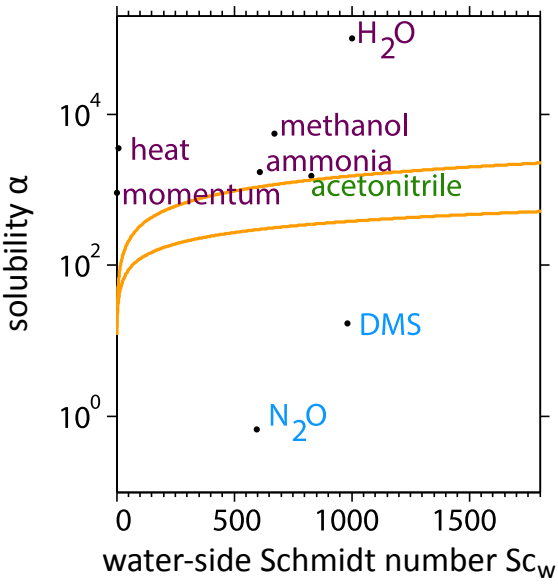

Fig. 2.2: Diagram showing the solubility α and the water-side Schmidt number Sc_w for different transported quantities (adapted from [Kräuter, 2015]). Quantities marked in purple are mainly controlled by the air side, while blue marked quantities are mainly controlled by the water side. The orange lines mark the transition zone lying in between, where quantities are equally controlled by the air and the water side. The upper and the lower line represent the limiting cases of a smooth and a rough water surface, respectively

Apart from the transfer resistance and transfer velocity, the mass boundary layer thickness z_*, which was already mentioned in the last section, is an important parameter for describing the air-water gas exchange. It is defined by

$$z_* = \left| \frac{c_s - c_b}{\frac{\partial c}{\partial z}\big|_{z=0}} \right| = D\frac{\Delta c}{j_c} = \frac{D}{k}, \tag{2.31}$$

with the (absolute) concentration difference Δc between the surface (c_s) and the bulk concentration (c_b). Moreover, the fact was used that at the interface ($z = 0$) only molecular diffusion contributes to the transport, which is described by Fick's first law (see Eq. 2.1 and the discussion in Sec. 2.2.1), resulting in a constant concentration gradient

$$\left.\frac{\partial c}{\partial z}\right|_{z=0} = -\frac{j_c}{D}. \tag{2.32}$$

Geometrically, z_* is given as the intercept between a constant line at the bulk concentration and the tangent of the concentration profile at the interface. This construction is indicated by the dashed lines in Fig. 2.1. The definitions of the transfer velocity and the boundary layer thickness motivate to introduce the **transfer time**

$$t_* = \frac{z_*}{k} = \frac{D}{k^2} \tag{2.33}$$

which a gas needs to cross the boundary layer. It is important to note that the parameters defined here are independent of explicit model considerations and only rely on the assumption that turbulent transport vanishes at the interface. Moreover, for characterizing the exchange process of a gas it is sufficient to know one of the quantities k, z_* and t_*. With the knowledge of the diffusion constant, they can be converted into each other. Analogous parameters that characterize the transport as well as solubilities can be defined for momentum and heat [Jähne and Haußecker, 1998].

According to Eq. 2.31, the boundary layer thickness is directly related to the diffusion constant. For most gases, the diffusion constants in air D_a and water D_w differ significantly by several orders of magnitude ($D_\mathrm{a} \approx 10^{-1}\,\mathrm{cm^2/s}$, $D_\mathrm{w} \approx 10^{-5}\,\mathrm{cm^2/s}$ [Yaws, 1999]), so that the water-side mass boundary layer thickness is typically much smaller than the air-side one. Furthermore, it was stated at the end of Sec. 2.1.1 that for most substances in air, the Schmidt number is about one, i.e. the kinematic viscosity ν_a and the diffusion constant D_a of most gases are roughly within the same order of magnitude. Thus, the air-side boundary layer thicknesses for momentum and gas transport are also similar. In water, Schmidt numbers are typically much larger ($\mathrm{Sc_w} \approx 10^3$). This is mainly caused by the difference of the diffusion constants in water and air, since the kinematic viscosity of water $\nu_\mathrm{w} \approx 1\,\mathrm{mm^2/s}$ [Lide and Frederikse, 1995] is only by a factor of about 10 smaller than the one of air $\nu_\mathrm{a} \approx 15\,\mathrm{mm^2/s}$ [Lide and Frederikse, 1995] (respectively at ambient pressure and temperature). As a consequence, the thicknesses of the viscous boundary layer in the water and the air phase are comparable.

2.2.3 Wind stress and waves

Wind stress acting on the water surface has an important influence on the air-water exchange processes by producing small-scale turbulence, which is confirmed by experiments [Walker and Peirson, 2008] and numerical simulations [Tsai et al., 2005]. In this context the wind speed and the distance over which the wind has blown, called fetch, are important parameters that can be adjusted in a wind-wave tunnel. An essential parameter to quantify the transport of momentum is the **friction velocity**

$$u_* = \sqrt{\frac{\tau}{\rho}}, \tag{2.34}$$

with the shear stress $\tau = j_\mathrm{m}$ (see. Eqs. 2.7 and 2.21) and the density of the fluid ρ. A temporally constant transport of momentum across the water surface, as depicted in Fig. 2.1 (b), implies the equation of the water-side and air-side stress

$$\tau_\mathrm{w} = \tau_\mathrm{a}, \tag{2.35}$$

leading to the following relation between the respective friction velocities:

$$u_{*,\mathrm{w}} = \sqrt{\frac{\rho_\mathrm{a}}{\rho_\mathrm{w}}} u_{*,\mathrm{a}}. \tag{2.36}$$

In the fully turbulent regime, the friction velocity is given by

$$u_* = \sqrt{\langle u_x' u_z' \rangle_t} \tag{2.37}$$

(cf. Eq. 2.15b).

In Sec. 2.2.1 it was already discussed that the relevance of the viscous term in Eq. 2.17b reduces with increasing distance from the air-water interface. This reasoning is incorporated in the following ansatz for the wind profile above the water surface

$$\frac{\mathrm{d}u_x}{\mathrm{d}z} \propto \frac{u_{*,\mathrm{a}}}{z} \Rightarrow u_x(z) = \frac{u_{*,\mathrm{a}}}{\kappa_\mathrm{Kar}} \ln(z/z_0), \tag{2.38}$$

with the reference height z_0, also called roughness length, and Kármán's constant $\kappa_\mathrm{Kar} \simeq 0.41$. This velocity profile is the well known **logarithmic wind profile** (for details see e.g. [Roedel, 2000]). A common reference wind speed is defined at a height of 10 m above the water surface by $u_{10} = u_x(z = 10\,\mathrm{m})$.

Wind blowing over the water surface generates Kelvin-Helmholtz instabilities, which result in surface displacements and the build up of waves. Given a free water surface, linear wave theory yields for the surface displacement

$$\eta(x,t) = \eta_\mathrm{max} \sin(kx - \omega t) \tag{2.39}$$

a sinusoidal wave as the fundamental solution. Here, η_max denotes the amplitude, $\omega = 2\pi/T$ the angular frequency and $k = 2\pi/\lambda$ the wave number with the period T and the wavelength λ. The dispersion relation of such a wave reads

$$\omega(k) = \sqrt{k\left(g + \frac{\sigma k^2}{\rho_\mathrm{w}}\right)\tanh(kh)} \approx \sqrt{k\left(g + \frac{\sigma k^2}{\rho_\mathrm{w}}\right)} \tag{2.40}$$

[Kundu et al., 2012]. Here, g is the gravitational acceleration, σ the surface tension and h the water depth. The approximation done in Eq. 2.40 is valid for a large water depth $h > \lambda/2$ and will be used in the following. The waves characterized by this dispersion relation are called **gravity waves** or **capillary waves** depending

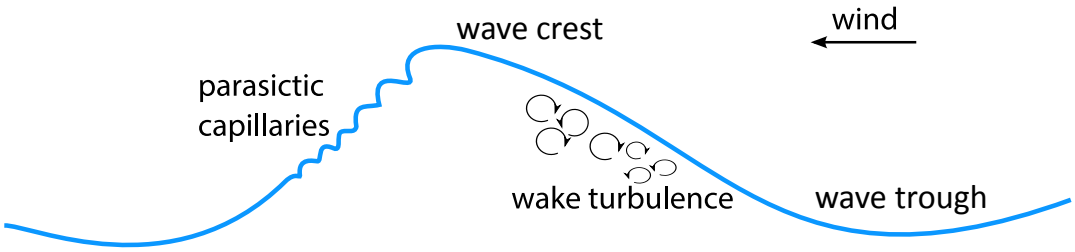

Fig. 2.3: Sketch of a gravity wave with parasitic capillaries at the leeward and wake turbulence at the windward side of the wave crest (modified after [Jessup et al., 1997])

on whether the dominant restoring force is given by gravity or by surface tension, respectively. The phase velocity

$$c_{\mathrm{ph}} = \frac{\omega}{k} = \sqrt{\frac{g}{k} + \frac{\sigma k}{\rho_{\mathrm{w}}}} \tag{2.41}$$

can be correspondingly approximated by $c_{\mathrm{ph,grav}} \propto 1/\sqrt{k}$ for longer and $c_{\mathrm{ph,cap}} \propto \sqrt{k}$ for smaller wavelengths. At intermediate wavelengths, where both terms in Eq. 2.41 are relevant, parasitic capillaries can form on the leeward side of a gravity wave crest, as sketched in Fig. 2.3.

Depending on the magnitude and the duration of wind stress, a variety of different turbulent structures and events near the water surface are generated. This includes e.g. the breaking of waves, which occurs at a critical wind stress, microscale wave breaking and Langmuir circulation. Since for this thesis only moderate wind speeds were used, wave breaking, which is usually accompanied by the production of droplets and bubbles, enlarging the gas exchange rate significantly [Mischler et al., 2015], is not of relevance for the conducted measurements. Langmuir circulation [Langmuir, 1938] is associated with the emergence of convergence and divergence zones at the water surface, which Langmuir concluded from his observation of the accumulation of seaweed and foam in the form of streaks along the wind direction. This flow pattern is related to counter-rotating vortices called Langmuir cells (see Fig. 2.4). Also a dissolved gas accumulates in streaks close to the water surface as shown e.g. by [Kräuter, 2015] and [Klein, 2019].

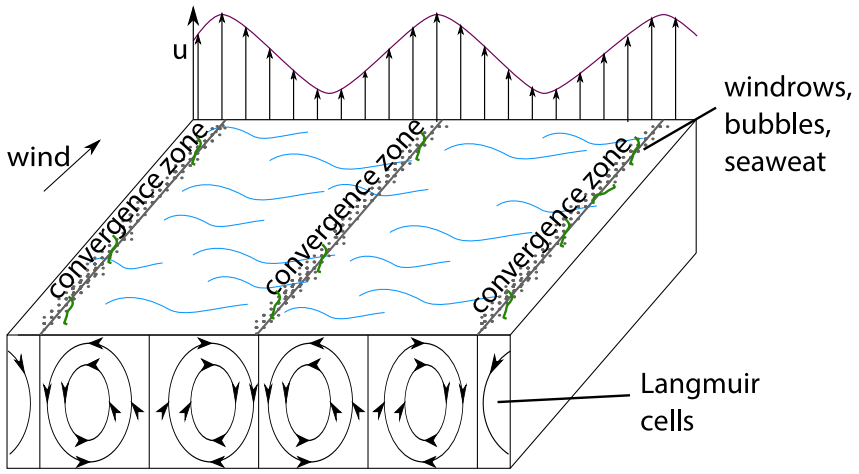

Fig. 2.4: Sketch of idealized Langmuir circulation showing the Langmuir cells and the convergence zones. The surface velocity u is displayed in the upper part of the figure (modified after [Thorpe, 2004]).

2.2.4 Gas exchange models

This section addresses the most important semi-empirical models which aim at predicting a mean concentration profile and a relation between the transfer resistance and the Schmidt number. The following discussion will focus on the water-side processes of gas transfer.

Film model

The film model, proposed by [Whitman, 1923], divides the water phase strictly into two layers. Within the boundary layer, which represents the film, the transport process is only governed by molecular diffusion, while below $z = z_*$ the water is assumed to be well mixed by turbulence, such that only turbulent diffusion is present. As a consequence the concentration profile is linear in the mass boundary layer. Integrating Eq. 2.23 with $K_c(0 \leq z \leq z_*) = 0$ yields a linearity between the transfer resistance and the Schmidt number

$$R = \frac{z_*}{D} \Rightarrow R \propto \mathrm{Sc}. \tag{2.42}$$

Even though the assumption of an abrupt change between the turbulent and the mass boundary layer is an oversimplification of the problem, the film model can be used for approximations. The model provides an upper limit for the transfer resistance as it ignores small eddies that contribute to the transport through the boundary layer, which was also shown experimentally [Jähne, 1980].

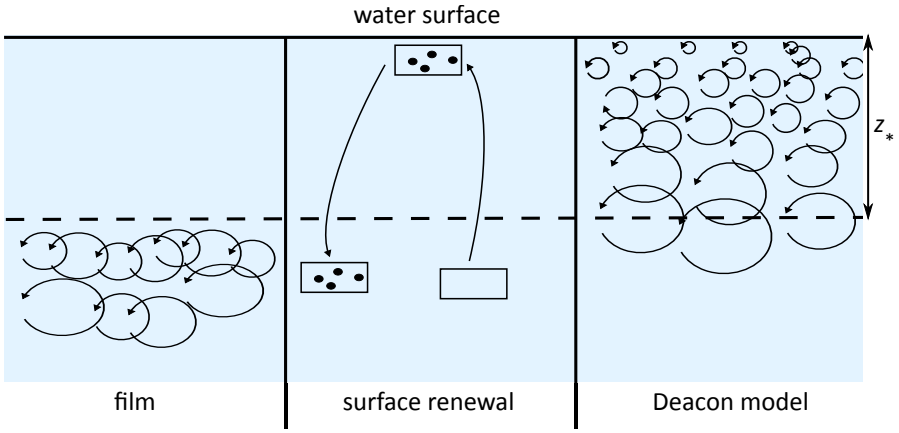

Fig. 2.5: Schematic illustration of turbulent structures which are assumed to govern the turbulent contribution to the water-side transport in the film, surface renewal and Deacon model. The water surface is represented as the top solid line, while the mass boundary layer thickness z_* is indicated by the dashed line (modified after [Kräuter, 2015]).

Deacon model

The model formulated by [Deacon, 1977] follows a more realistic concept that was already suggested in the discussion in Sec. 2.2.1. Instead of the step-like behavior of the turbulent diffusion coefficient, used in the film model, $K_c(z)$ is assumed to be a continuous function of the depth, related to a gradually decreasing eddy size towards the water surface where $K_c(z = 0) = 0$. Starting from a formulation of the velocity profile in turbulent flows at a wall proposed by [Reichardt, 1951], [Deacon, 1977] arrived at a semi-empirical parametrization of K_c for a smooth water surface. Assuming $\mathrm{Sc}_{\mathrm{turb}} = 1$ for simplicity, Eq. 2.23 can be solved numerically to give

$$R = \frac{15.2}{u_*}\mathrm{Sc}^{0.61} \quad (0.6 < \mathrm{Sc} < 10), \tag{2.43a}$$

$$R = \frac{12.1}{u_*}\mathrm{Sc}^{2/3} + 2.7 \cdot \log_{10}(\mathrm{Sc}) + 2.9 \quad (\mathrm{Sc} > 10). \tag{2.43b}$$

These equations are in good agreement with experiments at low wind speeds $u_{10} < 3.5\,\mathrm{m/s}$ with a smooth water surface. However, at higher wind speeds, where the assumption of a smooth water surface is not sufficiently fulfilled, the values of the measured transfer resistance are systematically lower than expected from the calculation. For higher Schmidt numbers $\mathrm{Sc} > 60$, the transfer resistance according to the model by Deacon can be approximated by

$$R \simeq \frac{12.1}{u_*}\mathrm{Sc}^{2/3} \quad (\mathrm{Sc} > 60) \tag{2.44}$$

(see [Jähne, 1980]).

Surface renewal model

The surface renewal model developed by [Higbie, 1935] and [Danckwerts, 1951] assumes that the gas transport on the water side is driven by stochastic renewal events where turbulent eddies penetrate the boundary layer and transport water packages with the surface concentration downwards into the water bulk. Simultaneously, water containing the bulk concentration is brought to the water surface. Between the renewal events, which occur at a certain rate γ_0, the gas transport is assumed to be dominated by molecular diffusion. These considerations lead to the following averaged transport equation (cf. Eq. 2.14a)

$$0 = D\frac{\partial^2 c}{\partial z^2} - \gamma_0 c, \tag{2.45}$$

which is solved by

$$c(z) = c_{\mathrm{w,s}} \exp\left(\frac{-z}{\sqrt{D/\gamma_0}}\right) \tag{2.46}$$

with $c_{\mathrm{w,s}} = c(z = 0)$. These relations are valid for a free or wavy water surface. The model was generalized by [Jähne, 1985] by introducing a depth dependence of the renewal rate $\gamma = \gamma_0 z^p$ $(p \geq 0)$. Solving the transport equation for a free $(p = 0)$ and a rigid water surface $(p = 1)$, leads to the following Schmidt number dependence of the transfer resistance

$$R \propto \frac{1}{u_*}\mathrm{Sc}^{\frac{p+1}{p+2}} \tag{2.47}$$

with a Schmidt number exponent of 1/2 and 2/3, respectively [Jähne et al., 1989].

Summary

The Schmidt number dependence of the transfer resistance is of great importance, since it relates properties of the transported quantity to parameters which are essential to characterize air-water exchange processes. A general, model-independent form of this relation was proposed by [Jähne, 1985]

$$R = \frac{\beta(\mathrm{bc})}{u_*}\mathrm{Sc}^{n(\mathrm{bc})}, \tag{2.48}$$

with a dimensionless scaling parameter β and the Schmidt number exponent n, which both depend on the boundary conditions (bc) at the water surface. In accordance with model predictions experiments showed that the Schmidt number exponent takes values between 1/2 ([Higbie, 1935], [Lamont and Scott, 1970]) for a free and 2/3 for a smooth water surface ([Deacon, 1977], [Jähne et al., 1989]). Furthermore a gradual transition between these two extreme cases could be observed experimentally ([Jähne et al., 1984], [Krall, 2013]).

2.3 Chemical reactions

The following section addresses some basics on chemical reactions (see e.g. [Riedel and Janiak, 2011]), which are relevant for this thesis, including reaction equilibria and acid-base reactions in aqueous solutions. After that, pH indicators are introduced and the implications of chemical reactions on the solubility are given.

Reaction equilibrium

Most reactions can be described as a reaction equilibrium of the form

$$\nu_A A + \nu_B B \rightleftharpoons \nu_C C + \nu_D D, \tag{2.49}$$

involving, for instance, substances A, B, C, D and their stoichiometric numbers ν_A, ν_B, ν_C, ν_D. The arrows in both directions illustrate a dynamic equilibrium which is maintained by the forward and the backward reaction with reaction rates

$$r_f = k_f \cdot [A]^{\nu_A}[B]^{\nu_B}, \tag{2.50a}$$

$$r_b = k_b \cdot [C]^{\nu_C}[D]^{\nu_D}, \tag{2.50b}$$

where k_f and k_b denote the corresponding reaction rate constants and the square brackets indicate the concentration of a substance. In equilibrium $r_f = r_b$, which gives rise to the equilibrium constant

$$K_{eq} = \frac{k_f}{k_b} = \frac{[C]^{\nu_C}[D]^{\nu_D}}{[A]^{\nu_A}[B]^{\nu_B}}. \tag{2.51}$$

This relation is called the **law of mass action**.

Acid-base reaction

A general acid-base reaction can be written as

$$AH + B \rightleftharpoons A^- + BH^+, \tag{2.52}$$

where the dissociation of a proton turns the acid AH to its conjugate base A^-. The proton is received by the base B to become its conjugate acid BH^+. A special acid-base reaction is the autoprotolysis of water

$$2\,H_2O \rightleftharpoons OH^- + H_3O^+, \tag{2.53}$$

which results in the formation of hydroxide (OH^-) and hydronium ions (H_3O^+). Applying the law of mass action (Eq. 2.51) to this reaction gives

$$K'_w = \frac{[H_3O^+] \cdot [OH^-]}{[H_2O]^2} \Rightarrow K_w = [H_3O^+] \cdot [OH^-], \tag{2.54}$$

where in the last step the fact was used that the concentration of water stays nearly constant, since most water molecules do not dissociate. At a temperature of 25 °C the **ion product of water** is $K_w \simeq 10^{-14}\,\mathrm{M}^2$ [Lide and Frederikse, 1995], where M = mol/l is used as a unit of concentration. The value of the ion product does not vary significantly within the ambient temperature range between 20 °C and 25 °C.

The acidity of a solution is characterized by the negative decadic logarithm of the hydronium concentration

$$\mathrm{pH} = -\lg([\mathrm{H_3O^+}]), \tag{2.55}$$

known as the (dimensionless) pH value. By definition units are dropped when taking the logarithm of concentrations or products of concentrations in the context of pH values and dissociation constants, which will be introduced in the next paragraph. Taking the negative decadic logarithm of Eq. 2.54 gives

$$\mathrm{pH} + \mathrm{pOH} = \mathrm{pK_w} = 14. \tag{2.56}$$

The usual pH scale therefore ranges from 0 to 14. Pure water has pH = 7 at 25 °C as charge neutrality requires pH = pOH. A solution with pH < 7 (pH > 7) is called acidic (alkaline).

In aqueous solutions, the strength of an acid or a base is quantified by its **acid dissociation constant** K_a. The strength of an acid is its tendency to dissociate a proton, while the strength of a base is its tendency to accept a proton. The reaction equation of water reacting with an acid A

$$\mathrm{H_2O} + \mathrm{AH} \rightleftharpoons \mathrm{H_3O^+} + \mathrm{A^-} \tag{2.57}$$

leads to the following expression for its acid dissociation constant

$$K_a(\mathrm{A}) = \frac{[\mathrm{H_3O^+}] \cdot [\mathrm{A^-}]}{[\mathrm{AH}]}, \tag{2.58}$$

where the concentration of water is already included in the constant. The $\mathrm{pK_a}$ value defined as the decadic logarithm of K_a

$$\mathrm{pK_a}(\mathrm{A}) = -\lg(K_a(\mathrm{A})) = \lg\left(\frac{[\mathrm{AH}]}{[\mathrm{A^-}]}\right) + \mathrm{pH} \tag{2.59}$$

is more commonly used. The reaction of a base B with water

$$\mathrm{H_2O} + \mathrm{B} \rightleftharpoons \mathrm{OH^-} + \mathrm{BH^+} \tag{2.60}$$

can be equivalently expressed as

$$\mathrm{H_3O^+} + \mathrm{B} \rightleftharpoons \mathrm{H_2O} + \mathrm{BH^+} \tag{2.61}$$

to give

$$K_\mathrm{a}(\mathrm{B}) = \frac{[\mathrm{H_3O^+}] \cdot [\mathrm{B}]}{[\mathrm{BH^+}]}, \quad \mathrm{pK_a(B)} = -\lg(K_\mathrm{a}(\mathrm{B})), \tag{2.62}$$

in analogy to Eqs. 2.58 and 2.59. The stronger an acid, the lower is its $\mathrm{pK_a}$ value, while the strength of a base increases with the $\mathrm{pK_a}$ value. To give an example, hydrogen chloride (HCl) with $\mathrm{pK_a(HCl)} = -7$ at 25 °C [Riedel and Janiak, 2011] is a strong acid, which will practically always dissociate completely. An equivalent formulation can be done by introducing the **base dissociation constant** K_b and the $\mathrm{pK_b}$ value, where

$$\mathrm{pK_a} + \mathrm{pK_b} = \mathrm{pK_w} = 14 \tag{2.63}$$

for any acid or base. In the following, the acid dissociation constant and the $\mathrm{pK_a}$ value will be used synonymously and referred to as the dissociation constant.

pH indicators

A typical pH indicator dissolved in an aqueous solution indicates the pH by its optical appearance. The indicator I used in this study is a fluorescent dye which will be discussed in Sec. 3.2.1. It has an acidic form IH and a alkaline form $\mathrm{I^-}$. Their concentrations depend on the pH value of the solution. The indicator reacts as an acid with water according to

$$\mathrm{IH} + \mathrm{H_2O} \rightleftharpoons \mathrm{I^-} + \mathrm{H_3O^+}. \tag{2.64}$$

The total indicator concentration is given by $[\mathrm{I}]_\mathrm{tot} = [\mathrm{IH}] + [\mathrm{I^-}]$. At low pH values ($\mathrm{pH} < 5$) lots of hydronium ions are present which may protonate the indicator such it mainly stays in its acidic form. Correspondingly, the concentration of the alkaline form of the indicator dominates at high pH values ($\mathrm{pH} > 9$). Usually, a pH indicator is used in low concentrations ($[\mathrm{I}]_\mathrm{tot} \leq 10^{-7}\,\mathrm{M}$). In this case, the concentration of hydronium provided by the forward reaction in Eq. 2.64 is negligible such that the indicator itself does not influence the pH value. The ratio between the two indicator components is determined by the dissociation constant of the indicator

$$\mathrm{pK_a(I)} = \lg\left(\frac{[\mathrm{IH}]}{[\mathrm{I^-}]}\right) + \mathrm{pH} \tag{2.65}$$

(cf. Eq. 2.59). It follows that at the so called **equivalence point** $\mathrm{pH} = \mathrm{pK_a(I)}$ both components are present in the same concentration. Since the indicator is supposed to signal the acidity or the alkalinity relative to the neutral point $\mathrm{pH} = 7$, its dissociation constant should be favorably $\mathrm{pK_a(I)} \sim 7$. This ensures an immediate turnover of the indicator, if an acidic solution becomes alkaline or vice versa. Fig. 2.6 shows the relative concentrations of the two indicator components for $\mathrm{pK_a(I)} = 7.3$.

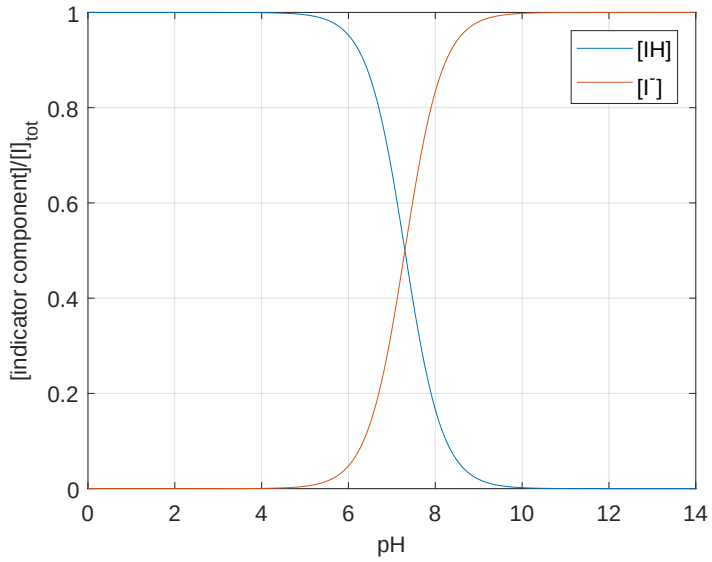

Fig. 2.6: Calculated concentrations of the two components IH and I^- of an indicator I with $pK_a(I) = 7.3$ as a function of the pH, based on Eq. 2.65. The total indicator concentration is denoted by $[I]_{tot}$.

Influence of chemical reactions on the solubility

The ability of a gas G to react as an acid or a base with water enlarges its solubility. As the water-side concentration of such a gas is effectively reduced by the reaction, more gas from the air side tends to dissolve in the water. This effect can be described by introducing an **effective solubility**

$$\alpha_{\mathrm{eff}}(\mathrm{G}) = \frac{[\mathrm{G}]_{\mathrm{w}}}{[\mathrm{G}]_{\mathrm{a}}} = \frac{[\mathrm{G}]_{\mathrm{w}}^{\mathrm{phys}} + [\mathrm{G}]_{\mathrm{w}}^{\mathrm{reac}}}{[\mathrm{G}]_{\mathrm{a}}} \tag{2.66}$$

with the total air-side equilibrium concentration $[\mathrm{G}]_{\mathrm{a}}$. The total water-side equilibrium concentration of the gas $[\mathrm{G}]_{\mathrm{w}}$ includes the concentration of the physically dissolved gas $[\mathrm{G}]_{\mathrm{w}}^{\mathrm{phys}}$ and the concentration of ions $[\mathrm{G}]_{\mathrm{w}}^{\mathrm{reac}}$, which result from acid-base reactions of the gas. Examples of reacting gases are CO_2, which is however still sparingly soluble due to slow reaction rates, as well as NH_3 and SO_2, which have high effective solubilities $> 10^3$.

2.4 Absorption and Fluorescence

This section aims to recapitulate a description of light absorption as it is typically used for spectroscopic measurements. Furthermore fluorescence is addressed following [Lakowicz, 2006].

Absorption

A common approach to describe the absorption of light of a certain wavelength λ passing a gaseous or liquid medium is given by the **Lambert–Beer law**. It states that the differential reduction of the transmitted intensity is proportional to the incident intensity I_0, the path length through the medium $\mathrm{d}z$ as well as the concentration $c(z)$ and the molar extinction coefficient $\epsilon_\mathrm{n}(\lambda)$ of the absorbing species

$$\mathrm{d}I_\mathrm{T}(\lambda) = -I_0(\lambda)\epsilon_\mathrm{n}(\lambda)c(z)\mathrm{d}z. \tag{2.67}$$

The differential reduction of the transmitted intensity is equivalent to the differential increase of the absorbed intensity $\mathrm{d}I_\mathrm{A}(\lambda) = -\mathrm{d}I_\mathrm{T}(\lambda)$. Assuming a total absorption length L, integration of Eq. 2.67 yields

$$I_\mathrm{T}(\lambda, L) = I_0(\lambda) \cdot e^{-\epsilon_\mathrm{n}(\lambda)\int_0^L c(z)\,\mathrm{d}z}, \tag{2.68a}$$

$$= I_0(\lambda) \cdot 10^{-\epsilon_\mathrm{d}(\lambda)\int_0^L c(z)\,\mathrm{d}z}, \tag{2.68b}$$

where the last expression represents the Lambert-Beer law written in the decadic basis, often used in chemistry. The different subscripts of the molar absorption coefficient indicate the natural and decadic basis with $\epsilon_\mathrm{n}(\lambda) = \epsilon_\mathrm{d}(\lambda)\ln(10)$. In a typical experimental setup $I_0(\lambda)$ represents the spectrum of the used light source. The **transmission** is defined as

$$T(\lambda, L) = \frac{I_\mathrm{T}(\lambda, L)}{I_0(\lambda)}. \tag{2.69}$$

With this, the **extinction** E and the **absorbance** A are introduced as the negative natural and decadic logarithm of the transmission

$$E(\lambda, L) = -\ln(T(\lambda, L)), \tag{2.70a}$$

$$A(\lambda, L) = -\lg(T(\lambda, L)), \tag{2.70b}$$

so that the equations in 2.68 can be conveniently written as

$$E(\lambda, L) = \epsilon_\mathrm{n}(\lambda) \int_0^L c(z)\,\mathrm{d}z, \tag{2.71a}$$

$$A(\lambda, L) = \epsilon_\mathrm{d}(\lambda) \int_0^L c(z)\,\mathrm{d}z. \tag{2.71b}$$

In the following, the absorbance and the decadic molar absorption coefficient will be used in the context of absorption if not stated otherwise. Eq. 2.71b is useful to measure mean concentrations $\bar{c}$ of a substance with known molar absorption coefficient along the absorption length L

$$A(\lambda, L) = \epsilon_{\mathrm{d}}(\lambda) \int_0^L c(z)\,\mathrm{d}z = \epsilon_{\mathrm{d}}(\lambda)\bar{c}L. \tag{2.72}$$

If M independent, absorbing species are present in the medium, Eq. 2.67 is generalized to

$$\mathrm{d}I_{\mathrm{T}}(\lambda) = -I_0(\lambda) \sum_{m=1}^{M} \ln(10)\epsilon_{\mathrm{d},m}(\lambda)c_m(z)\mathrm{d}z. \tag{2.73}$$

As a consequence, the absorbance reads

$$A(\lambda, L) = \sum_{m=1}^{M} \epsilon_{\mathrm{d},m}(\lambda) \int_0^L c_m(z)\,\mathrm{d}z. \tag{2.74}$$

For the evaluation of the absorption spectroscopy measurements performed for this thesis, a DOAS-like approach is employed by adding a polynomial to Eq. 2.74

$$A(\lambda, L) = \sum_{m=1}^{M} \epsilon_{\mathrm{d},m}(\lambda) \int_0^L c_m(z)\,\mathrm{d}z + \sum_n p_n\lambda^n, \tag{2.75}$$

which accounts for possible broadband changes in the measured absorption spectra due to changes of the lamp spectrum. The DOAS (**D**ifferential **O**ptical **A**bsorption **S**pectroscopy) method was developed by [Platt et al., 1979] to measure the concentration of several atmospheric trace gases simultaneously.

Fluorescence

Fluorescence is a type of photoluminescence, where an orbital electron of an atom or a molecule transitions from an excited state to its ground state by emitting a photon. Both electron states involved in this transition are singlet states (S) with zero total spin. A substance that can be excited optically to emit fluorescence light is called fluorophore. The process can be illustrated by a Jablonski diagram as shown in Fig. 2.7, where the vertical axis represents the energy of the ground state S_0 and the first two excited states S_1 and S_2. The three sublevels of each state indicate the vibrational energy levels, which an electron can occupy. Prior to fluorescence, a photon is absorbed which has an energy high enough to lift an electron from the lowest

vibrational level of the ground state $S_0(0)$ to an excited state. This process happens on a very short time scale of 10^{-15} s. Depending on the energy level the electron now occupies, two decay paths which finally lead to fluorescence are possible. If the electron sits in the lowest vibrational level of the first excited $S_1(0)$ a photon is emitted after a certain lifetime of typically 10^{-8} s leaving the electron in one of the vibrational levels of the ground state S_0. Otherwise the electron first loses energy via (non-radiative) vibrational relaxation, also known as internal conversion, until it reaches $S_1(0)$ within 10^{-12} s, before a photon is emitted. Because a significant number of vibration cycles occur during the lifetime of excited states, an electron most probably always undergoes complete vibrational relaxation to $S_1(0)$. Having reached a vibrational level of the ground state, the electron will quickly arrive at $S_0(0)$ by further relaxation. Besides, other non-radiative relaxation processes like intersystem crossing or collisions with other molecules are possible. These effects which reduce the fluorescence intensity are summarized by the term quenching. The term photobleaching describes the photochemical alteration or destruction of a fluorophore molecule such that it permanently loses its ability to fluoresce. In general, fluorescence light is emitted isotropically by a fluorophore molecule.

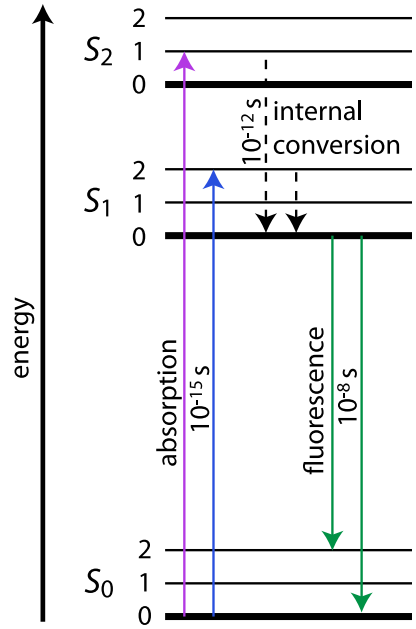

Fig. 2.7: Typical Jablonski diagram illustrating the singlet states (S) of an electron, which are involved in the process of fluorescence, including their vibrational sublevels. The time scales on which the different processes take place are shown (modified after [Friedl, 2013]).

Fluorescence light has less energy than the absorbed light. The associated wavelength difference is called **Stokes shift**. This shift is caused by energy losses due to internal conversion, as described above.

The **quantum yield** Φ_F of a fluorophore can be defined as the ratio of the number

of photons emitted N_e to the number of photons absorbed N_a

$$\Phi_F = \frac{N_e}{N_a}. \tag{2.76}$$

A high quantum yield implies that the non-radiative decay rate is small compared to the radiative decay rate.

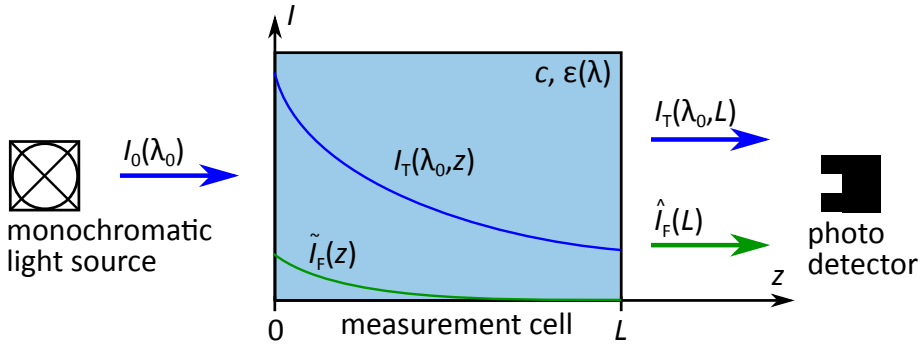

Fig. 2.8: Illustration of an experimental arrangement involving a monochromatic light source emitting $I_0(\lambda_0)$, a measurement cell with length L and a photo detector. The cell is filled with a solution containing a fluorophore in a concentration c. Its absorption coefficient is denoted by $\epsilon(\lambda)$. The intensity of the transmitted light $I_T(\lambda_0, L)$ and the fluorescence $\hat{I}_F(L)$ is measured with the detector. The respective profiles $I_T(\lambda_0, z)$ and $\tilde{I}_F(z)$ are sketched.

To explain the dependency of the fluorescence intensity on the excitation intensity, a typical experimental configuration is considered for illustrative purposes (see Fig 2.8). A solution containing a fluorophore in a concentration c is filled in a measurement cell with length L. The fluorophore has a molar absorption coefficient $\epsilon(\lambda)$ and an emission spectrum $I_F(\lambda)$. Monochromatic light $I_0(\lambda_0)$ is irradiated on one side of the cell. The fluorophore absorbs a fraction of the incident light and is excited to fluoresce. The transmitted light intensity $I_T(\lambda_0, L)$, given by Eq. 2.68b, and the fluorescence intensity $\hat{I}_F(L)$ are measured by a photo detector placed on the opposite side of the cell. The measured fluorescence signal is given by the fraction of emitted photons that reach the detector. It follows that

$$\hat{I}_F(L) \propto N_e, \tag{2.77}$$

where the fluorescence emission is assumed to be isotropic. In this way, the directed light of the source is converted into undirected fluorescence light. The total number of emitted and absorbed photons can be expressed as $N_e = \int_{-\infty}^{\infty} I_F(\lambda')\,\mathrm{d}\lambda'$ and $N_a = I_A(\lambda_0, L)$, respectively. Here, $I_A(\lambda_0, L)$ denotes the intensity of absorbed light given by

$$I_A(\lambda_0, L) = (I_0(\lambda_0) - I_T(\lambda_0, L)) = I_0(\lambda_0)(1 - 10^{-A(\lambda_0, L)}). \tag{2.78}$$

With the expressions for the number of photons and Eq. 2.76, Eq. 2.77 can be written as

$$\hat{I}_{\mathrm{F}}(L) \propto \Phi_{\mathrm{F}} \cdot I_0(\lambda_0)(1 - 10^{-A(\lambda_0, L)}). \tag{2.79}$$

If the absorbance is low ($A \leq 0.05$), the fluorescence intensity is linear to the concentration

$$\hat{I}_{\mathrm{F}}(L) \propto \Phi_{\mathrm{F}} \cdot I_0(\lambda_0) \ln(10) \epsilon(\lambda_0) c L. \tag{2.80}$$

The measured signal $\hat{I}_{\mathrm{F}}(L)$ corresponds to the fluorescence intensity integrated along the cell

$$\hat{I}_{\mathrm{F}}(L) = \int_0^L \tilde{I}_{\mathrm{F}}(z)\,\mathrm{d}z, \tag{2.81}$$

with the intensity profile $\tilde{I}_{\mathrm{F}}(z)$. In this thesis, the quantities $\hat{I}_{\mathrm{F}}(L)$ and $\tilde{I}_{\mathrm{F}}(z)$ will be referred to as the depth-integrated fluorescence intensity and the fluorescence profile, respectively. The fluorescence profile is proportional to the profile of the transmitted intensity $I_{\mathrm{T}}(\lambda_0, z)$, since at every z a fraction of the residual excitation light is converted into fluorescence emission. This proportionality is only valid for monochromatic light.

If a light source with an arbitrary spectrum $I_0(\lambda)$ is used, Eq. 2.79 changes to

$$\hat{I}_{\mathrm{F}}(L) \propto \Phi_{\mathrm{F}} \int_{-\infty}^{\infty} I_0(\lambda')(1 - 10^{-A(\lambda', L)})\,\mathrm{d}\lambda'. \tag{2.82}$$

The integral of the transmitted intensity spectrum $I_{\mathrm{T}}(\lambda, z)$ over all wavelengths is denoted by

$$\tilde{I}_{\mathrm{T}}(z) = \int_{-\infty}^{\infty} I_{\mathrm{T}}(\lambda', z)\,\mathrm{d}\lambda'. \tag{2.83}$$

3. Methods

This chapter aims to explain the new method developed in this study. First of all, the fundamental measurement principle is outlined. After that, the used chemical components including the fluorescent pH indicator and the alkaline gas are characterized. Subsequently, the new chemical system is discussed and illustrated by means of a calculation. Last but not least, mass balance methods are introduced.

3.1 Basic measurement principle

The key idea of the measurement method is to establish a direct relation between the concentrations of a trace gas and the alkaline form of a fluorescent pH indicator. The experiment is designed as the invasion of an alkaline gas R into acidic water where the pH indicator I is dissolved. The initial water-side concentration of the gas is zero. The intensity of the fluorescence emission of the alkaline indicator component serves as a measure of its concentration.

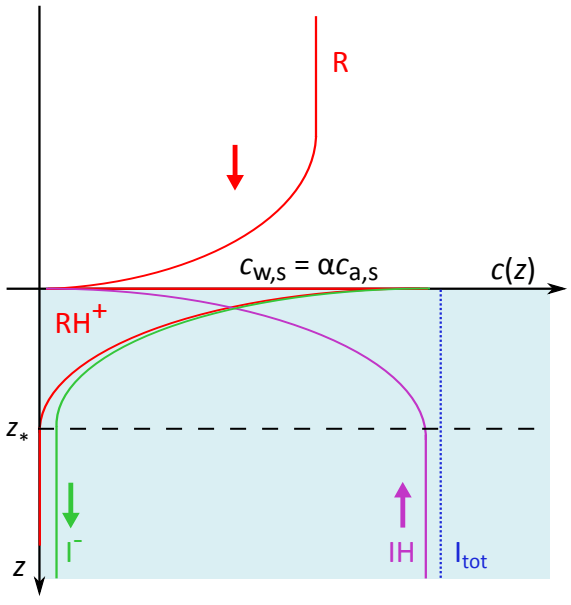

Fig. 3.1: Sketch of the concentration depth profile for the invasion of an alkaline gas R into slightly acidic water (pH = 6) with the water-side mass boundary layer thickness z_*. Due to the high indicator concentration $[\mathrm{I}]_{\mathrm{tot}} = [\mathrm{IH}] + [\mathrm{I}^-]$, the concentration of the water ions can be neglected such that the protonation of the gas is mainly caused by its reaction with IH resulting in an increase of $[\mathrm{I}^-]$. The arising concentration fluxes are indicated by arrows.

The reaction equilibria of the indicator and the dissolved gas can be written as

$$\mathrm{R} + \mathrm{H_3O^+} \rightleftharpoons \mathrm{RH^+} + \mathrm{H_2O}, \tag{3.1a}$$

$$\mathrm{IH} + \mathrm{H_2O} \rightleftharpoons \mathrm{I^-} + \mathrm{H_3O^+}. \tag{3.1b}$$

First, the indicator is assumed to be used in a low concentration ($[\mathrm{I}]_{\mathrm{tot}} \leq 10^{-7}\,\mathrm{M}$), as usual (see Sec. 2.3). If now the water-side concentration of the gas increases during the invasion, the concentration of hydronium decreases according to the forward reaction in Eq. 3.1a. To compensate this change, more molecules of the acidic form of the indicator IH tend to dissociate according to the forward reaction in Eq. 3.1b, ending up in their alkaline form I^-. Thus, the change of the pH caused by the invasion of the gas is detected by the indicator. By exciting only I^- molecules close to the water surface to fluorescence, the water-side mass boundary layer of the dissolved gas is made visible. This describes the principle of the boundary layer imaging (BLI) method, that was developed by [Kräuter et al., 2014]. With a low concentration of the indicator, nearly all indicator molecules turn locally into their alkaline form, where the gas enters the water. As a consequence, the fluorescence intensity is approximately constant over depth within the boundary layer thickness, independent of the concentration of the alkaline gas, and zero outside.

In this thesis, a new chemical system is employed by using a high concentration of the indicator $[\mathrm{I}]_{\mathrm{tot}} \geq 10^{-4}\,\mathrm{M}$. Moreover, the initial pH value of the water, before the gas is let into the air space, is set to $\simeq 6$. This implies $[\mathrm{H_3O^+}] \simeq 10^{-6}\,\mathrm{M}$ and $[\mathrm{OH^-}] \simeq 10^{-8}\,\mathrm{M}$. Thus, the concentrations of the water ions become negligible compared to the concentration of the indicator components such that the dissolved gas is mostly protonated by the acidic form of the indicator. Consequently, the reactions in Eq. 3.1, where water or water ions were the reaction partners of the gas and the indicator components, are combined to the effective reaction

$$\mathrm{IH} + \mathrm{R} \rightarrow \mathrm{I^-} + \mathrm{RH^+}. \tag{3.2}$$

This reaction describes the fundamental idea of the developed method. A sketch of the invasion experiment with the described setting is shown in Fig. 3.1. If the difference between the dissociation constant $\mathrm{pK_a(R)}$ of the gas and the pH value is larger, more gas molecules are protonated (cf. Eq. 2.59) and the protonation happens faster. For the method, a gas with $\mathrm{pK_a(R)} > 9$ is chosen, which ensures that gas molecules entering an acidic or neutral solution react to their protonated form immediately. As a consequence, the concentration of dissolved, unprotonated gas stays nearly zero. This means that $[\mathrm{R}]_{\mathrm{w,tot}} = [\mathrm{R}]_{\mathrm{w}} + [\mathrm{RH^+}] \approx [\mathrm{RH^+}]$, such that the air-side gas flux is unaffected by water-side transport processes and the air-water transfer process is controlled by the air side. However, the reaction of the gas close the water surface leads locally to a lack of IH and an excess of I^- molecules, which induces concentration fluxes of the two indicator components between the water bulk and the mass boundary layer. The flux of the acidic component from the bulk towards the boundary layer equals the flux of the alkaline component from the boundary layer towards the bulk. In the water bulk, the ratio $[\mathrm{IH}]/[\mathrm{I^-}]$ is controlled by the predefined pH. As a result, also water-side transport processes of the indicator components are of

relevance. In contrast to the previously employed BLI method, where the diffusion of the protonated gas RH^+ was dominant, the diffusion of the alkaline indicator component I^- has to be considered equally due to the high concentration of the indicator. This can be described by a coupled diffusion constant

$$D_{I^-,RH^+} = \frac{2}{1/D_{I^-} + 1/D_{RH^+}}. \tag{3.3}$$

For more details on this see [Cussler, 2009].

The charge conservation for the reaction in Eq. 3.2 is given by

$$[I^-] = [RH^+] + \text{const.}, \tag{3.4}$$

where the constant summarizes the concentrations of ions of fully dissociated salts, which do not participate in the reactions. With the approximation $[RH^+] \approx [R]_{w,tot}$, a direct proportionality between the concentrations of the alkaline form of the indicator and the gas entering the water phase

$$[I^-] \propto [R]_{w,tot} \tag{3.5}$$

is found, with a proportionality factor close to one. A more precise value will be estimated in Sec. 3.3. Thus, in regions where the gas enters the water the visible fluorescence intensity increases in way that the concentration change of the dissolved gas can be inferred. Equation 3.5 implies also a proportionality of the concentration fluxes

$$j_{a,R} = j_{w,R} \simeq j_{RH^+} \propto j_{I^-} = -j_{IH}, \tag{3.6}$$

where a constant gas flux on the air side was assumed.

In principle, the approximation $[I]_{tot} \gg [H_3O^+], [OH^-]$ is valid for $pH = 6 - 8$. The initial pH is set to ~ 6 because at higher pH values a significant fraction of the indicator molecules will already be in their alkaline form. This leads to a high background fluorescence of the water bulk such that changes of the fluorescence intensity caused by the gas invasion are difficult to observe. This thesis focuses on the experimental verification of the newly developed method, using the equations 3.5 and 3.6 as a first starting point.

3.2 Characterization of the chemicals

Since the method described above is based on the chemical reaction Eq. 3.2 and the associated approximations, a careful selection of the chemical components is crucial. In the following, the properties of the chosen dyes and the alkaline gas are presented and discussed with regard to the necessary requirements.

3.2.1 Dyes

Fluorescent pH indicator

As mentioned in Sec. 2.3, the $pK_a(I)$ value of the pH indicator should be favorably near the neutral point pH = 7. Considering the invasion experiment described in the last section, this ensures an immediate turnover from the acidic to the alkaline form, when the solution becomes alkaline. Moreover, the fluorescence intensity of the alkaline form I^- is supposed to be a measure of its concentration $[I^-]$. This requires that the absorption spectra of both forms are distinctly different.

The pH-dependent fluorescent dye **pyranine**, also known as HPTS (8-hydroxypyrene-1,3,6-trisulfonic acid), with the chemical formula $C_{16}H_7Na_3O_{10}S_3$ fulfills these requirements. It has a molar mass of $m_M = 524.4\,g/mol$ and is well soluble in water. According to [Wolfbeis et al., 1983], it has a protonation time of about 5.6 ns and its $pK_a(I)$ value ranges from 8.04 in the case of pure water to 7.29 in dependence of the concentration of additional salts in the solution. Because of the importance of the dissociation constant of pyranine and its variability with the ion concentration, its value was measured separately at a low ion concentration using a spectrophotometer (see. 5.1.1). The result $pK_a(I) = 7.68 \pm 0.03$ will be used as a reference in this thesis.

Figure 3.2 (a) shows the molar absorption coefficient of the two pyranine components. A blue light source will be used in this thesis that fits the absorption spectrum of I^-, which peaks at $\lambda = 455\,nm$. Both components have the same fluorescene emission spectrum that is also shown in Fig. 3.2 (a). The emission is highest at $\lambda = 512\,nm$. Apart from the possibility to excite one component selectively, pyranine has many advantages compared to other fluorescent indicators. Among 20 different pH indicators, [Wolfbeis et al., 1983] found pyranine to be the most suitable one for measurements close to neutral pH values. Due to its high quantum yield of almost 1 for excitation wavelengths $\lambda > 400\,nm$, nearly all absorbed light is emitted. Also very important is the large Stokes shift of about 60 nm, which allows a clear distinction between excitation and emission light. Further advantages are the stability against photobleaching, temperature changes and quenching by oxygen. Pyranine was used by [Wolfbeis and Posch, 1986] to measure the concentration of ammonia. The most important properties of pyranine are summarized in Tab. 3.1.

Absorbing dye

Since pH values around pH $\simeq 6$ are needed for the method to justify the approximation $[I]_{tot} \gg [H_3O^+], [OH^-]$, a significant fraction of pyranine molecules will already be in the alkaline form. To suppress the background fluorescence of the water bulk,

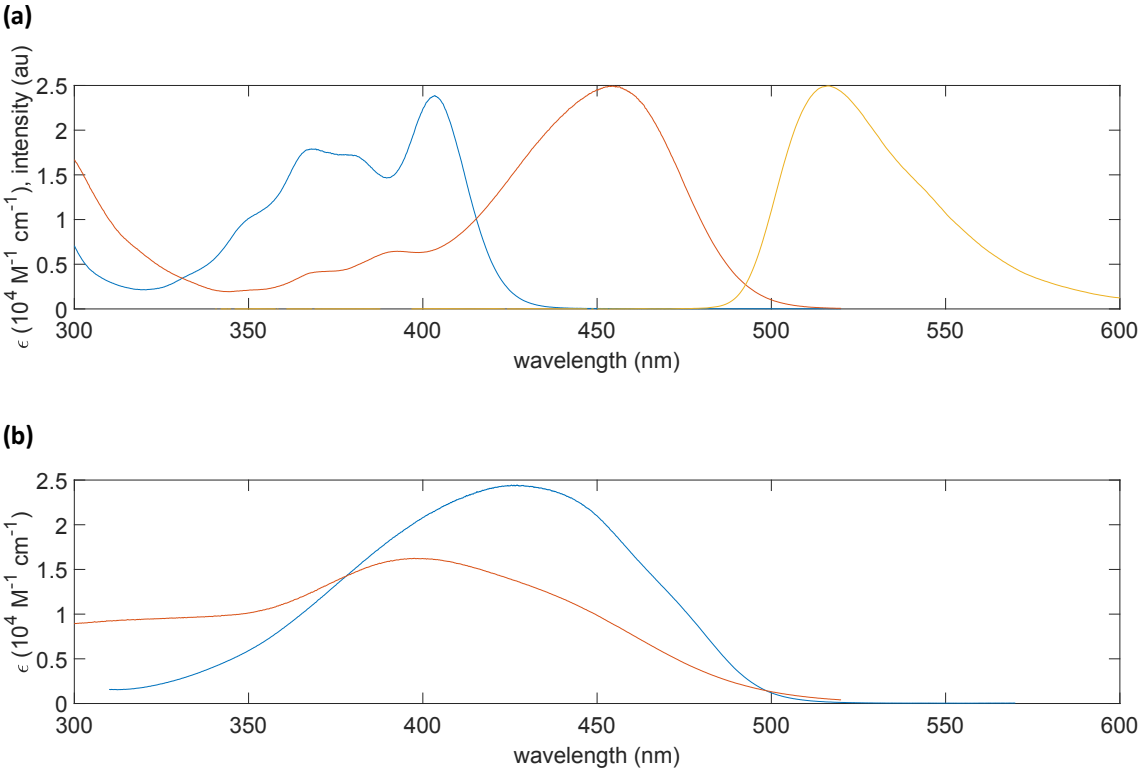

Fig. 3.2: (a) Molar absorption coefficient ϵ of the acidic (blue) and the alkaline (red) form of pyranine as a function of the wavelength, measured at a pH of 4 and 11, respectively (see Sec. 5.1.1). Moreover, the intensity of their fluorescence emission spectrum (yellow), taken from [Kräuter, 2015], is shown. (b) Molar absorption coefficient ϵ of the acidic (blue) and the alkaline (red) form of tartrazine, measured at a pH of 4 and 12, respectively (see Sec. 5.1.2).

which would diminish the contrast of the fluorescent signal resulting from the gas transfer, an absorbing dye called **tartrazine** (Food Yellow 4) with the chemical formula $C_{16}H_9N_4Na_3O_9S_2$ is added to the water. The dye absorbs the blue light, which excites the fluorescent indicator, such that is does not reach the deeper water layers in the bulk. Near the water surface, where most of the dynamics of the gas transfer take place, this effect is rather small. Tartrazine has a molar mass of $m_M = 534.4\,\mathrm{g/mol}$ and is a synthetic azo dye, which is used in the food industry as a colorant (yellow). It is well soluble in water and stays colorfast in acidic media as well as under high irradiation. Like pyranine, tartrazine can dissociate in aqueous solutions by donating a proton. But due to its higher dissociation constant $\mathrm{pK_a(T)} = 9.4 - 10$ [Perez-Urquiza and Beltran, 2001], it stays predominantly in its acidic form within the pH range relevant for this thesis. The acidic and the alkaline form of tartrazine are denoted by TH and $\mathrm{T^-}$, respectively. As for pyranine, the dissociation constant

of tartrazine was also determined from results of own measurements at a low ion concentration that yielded 9.91 ± 0.03 (see Sec. 5.1.2).

The molar absorption coefficient of the two tartrazine components is shown in Fig. 3.2 (b). The absorption characteristic of the acidic form TH peaks at $\lambda = 426\,\mathrm{nm}$ and covers the blue wavelength range around $\lambda = 450\,\mathrm{nm}$, where the absorption of I^- is the highest. Due to the small spectral overlap of the absorption coefficient of TH with the emission spectrum of pyranine, the fluorescence intensity is not significantly reduced. The most important properties of tartrazine are summarized in Tab. 3.1.

substance	formula	m_M(g/mol)	pK_a	$\lambda_{max,abs}$	$\lambda_{max,emi}$
pyranine	$C_{16}H_7Na_3O_{10}S_3$	524.4	$7.29 - 8.04(7.68)$	455	512
tartrazine	$C_{16}H_9N_4Na_3O_9S_2$	534.4	$9.4 - 10(9.91)$	426	–

Table 3.1: Summary of the properties of pyranine and tartrazine. The chemical formulae and the molar masses are from NIST (National Institute of Standards and Technology). The other properties can be found in [Wolfbeis et al., 1983] and in [Perez-Urquiza and Beltran, 2001] for pyranine and tartrazine, respectively. The pK_a values in brackets are results from own measurements at a low ion concentration (see Sec. 5.1).

3.2.2 Alkaline gas

The alkaline gas used for this thesis is ammonia, since it was already successfully used for the BLI method in [Kräuter, 2015]. Ammonia (NH_3) is a colorless, diamagnetic gas, which has a characteristically pungent smell. It dissolves in water and reacts as a weak base

$$NH_3 + H_3O^+ \rightleftharpoons NH_4^+ + H_2O \tag{3.7}$$

to ammonium (NH_4^+) with a dissociation constant of $pK_a(NH_3) = 9.25$ at 25 °C [Clegg and Brimblecombe, 1989].

The values found in literature for the dimensionless physical solubility of ammonia vary over a wide range from 812 [Shi et al., 1999] to 2256 [Hales and Drewes, 1979]. This thesis follows the recommendation $\alpha(NH_3) = 1463$ by [Sander, 2015]. Due to the reaction in Eq. 3.7, the pH-dependent effective solubility of ammonia

$$\alpha_{eff}(NH_3) = \frac{[NH_3]_w + [NH_4^+]_w}{[NH_3]_a} = \alpha(NH_3)(1 + 10^{-pH+pK_a(NH_3)}) \tag{3.8}$$

[Fogg and Sangster, 2003] has to be considered. Figure 3.3 shows $\alpha_{\text{eff}}(NH_3)$ calculated with this equation, assuming a physical solubility of $\alpha(NH_3) = 1463$. An overview of the properties of ammonia is given in Tab. 3.2.

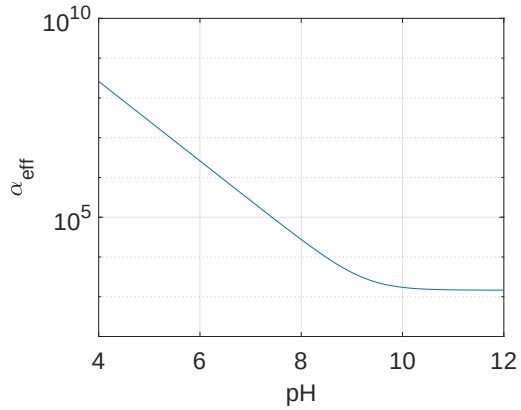

Fig. 3.3: Effective solubility of ammonia $\alpha_{\text{eff}}(NH_3)$ calculated with Eq. 3.8 as a function of the pH, assuming a physical solubility of $\alpha(NH_3) = 1463$.

substance	formula	m_M (g/mol)	pK_a	α	D_w (cm^2/s)	D_a (cm^2/s)
ammonia	NH_3	17.03	9.25	$812 - 2256(1463)$	$1.64 \cdot 10^{-5}$	0.23

Table 3.2: Overview of the properties of ammonia. The molar mass is taken from NIST (National Institute of Standards and Technology). The pK_a value can be found in [Clegg and Brimblecombe, 1989]. The lowest value for the solubility is from [Shi et al., 1999], the highest from [Hales and Drewes, 1979], while the value in brackets, which is assumed for this thesis, can be found in [Sander, 2015]. The values of the diffusion constants are from [Yaws, 1999].

With the employed chemical system, ammonia is mainly protonated by the acidic pyranine component to ammonium

$$IH + NH_3 \rightarrow I^- + NH_4^+ \tag{3.9}$$

(cf. Eq. 3.2). Since this protonation happens immediately, the water-side transport processes in the mass boundary layer can be assumed to be controlled by diffusion. The coupled diffusion constant (cf. Eq. 3.3) of I^- and NH_4^+ molecules can be written as

$$D_{I^-,NH_4^+} = \frac{2}{1/D_{I^-} + 1/D_{NH_4^+}} = 4.1 \cdot 10^{-6}\,\text{cm}^2/\text{s}, \tag{3.10}$$

with $D_{I^-} = 2.3{\cdot}10^{-6}\,\text{cm}^2/\text{s}$ [Xia et al., 1998] and $D_{NH_4^+} = 1.96{\cdot}10^{-5}\,\text{cm}^2/\text{s}$ [Yaws, 1999].

3.3 Chemical system

In this section, details on the used chemical system are discussed. In particular, the relation given in Eq. 3.5 will be derived explicitly by solving a system of equations. With the results of the calculation the proportionality factor is obtained.

An aqueous solution containing dissolved ammonia, pyranine and tartrazine is considered. This leads to the following system of equations

$$10^{-\mathrm{pK_w}} = [\mathrm{H_3O^+}] \cdot [\mathrm{OH^-}], \tag{3.11a}$$
$$[\mathrm{NH_3}]_{\mathrm{w,tot}} = [\mathrm{NH_3}]_{\mathrm{w}} + [\mathrm{NH_4^+}]_{\mathrm{w}}, \tag{3.11b}$$
$$10^{-\mathrm{pK_a(NH_3)}} = \frac{[\mathrm{H_3O^+}] \cdot [\mathrm{NH_3}]}{[\mathrm{NH_4^+}]}, \tag{3.11c}$$
$$[\mathrm{I}]_{\mathrm{tot}} = [\mathrm{IH}] + [\mathrm{I^-}], \tag{3.11d}$$
$$10^{-\mathrm{pK_a(I)}} = \frac{[\mathrm{H_3O^+}] \cdot [\mathrm{I^-}]}{[\mathrm{IH}]}, \tag{3.11e}$$
$$[\mathrm{T}]_{\mathrm{tot}} = [\mathrm{TH}] + [\mathrm{T^-}], \tag{3.11f}$$
$$10^{-\mathrm{pK_a(T)}} = \frac{[\mathrm{H_3O^+}] \cdot [\mathrm{T^-}]}{[\mathrm{TH}]}, \tag{3.11g}$$

which accounts for the autoprotolysis of water as well as the mass conservation and the reaction equilibrium of dissolved ammonia, pyranine and tartrazine. The necessary constants are

$$\begin{aligned} \mathrm{pK_w} &= 14, \\ \mathrm{pK_a(NH_3)} &= 9.25, \\ \mathrm{pK_a(I)} &= 7.68, \\ \mathrm{pK_a(T)} &= 9.91, \end{aligned}$$

where for the dissociation constants of the dyes results from own measurements are assumed (see Sec. 5.1). Additionally, the influence of CO_2 dissolved in the water should be considered, since ambient CO_2 inevitably enters the water phase. Moreover, the deionized water used in the experiments already contains ambient concentrations of CO_2. Apart from the physically dissolved $CO_2(aq)$, carbonic acid H_2CO_3 is the other charge-neutral form of carbon dioxide in water, which is only present in low concentration $[H_2CO_3]/[CO_2(aq)] \lesssim 0.3\,\%$ (see [Zeebe and Wolf-Gladrow, 2001]). Therefore, their concentrations are summarized by $[CO_2]_w = [CO_2(aq)] + [H_2CO_3]$. The water-side reactions of carbon dioxide can be then written as

$$CO_2 + 2\,H_2O \rightleftharpoons HCO_3^- + H_3O^+, \tag{3.12a}$$
$$HCO_3^- + H_2O \rightleftharpoons CO_3^{2-} + H_3O^+, \tag{3.12b}$$

leading to

$$[CO_2]_{w,tot} = [CO_2]_w + [HCO_3^-] + [CO_3^{2-}], \tag{3.13a}$$
$$10^{-pK_a^1(CO_2)} = \frac{[H_3O^+] \cdot [HCO_3^-]}{[CO_2]_w}, \tag{3.13b}$$
$$10^{-pK_a^2(CO_2)} = \frac{[H_3O^+] \cdot [CO_3^{2-}]}{[HCO_3^-]}. \tag{3.13c}$$

For the values of the dissociation constants, $pK_a^1(CO_2) = 6.4$ [Harned and Davis, 1943] and $pK_a^2(CO_2) = 10.3$ [Harned and Scholes, 1941] are assumed.

The pH value before and after the invasion experiment can be controlled by adding amounts of a HCl solution, where $[HCl] = [Cl^-]$ due to full dissociation. The charge conservation for the whole system reads

$$[NH_4^+] + [H_3O^+] = [OH^-] + [I^-] + [T^-] + [HCO_3^-] + 2 \cdot [CO_3^{2-}] + [Cl^-]. \tag{3.14}$$

With the input parameters $[NH_3]_{w,tot}$, $[I]_{tot}$, $[T]_{tot}$, $[CO_2]_{w,tot}$ and $[Cl^-]$, the system of equations can be solved for the concentrations $[H_3O^+]$, $[OH^-]$, $[NH_3]_w$, $[NH_4^+]$, $[IH]$, $[I^-]$, $[TH]$, $[T^-]$, $[CO_2]_w$, $[HCO_3^-]$ and $[CO_3^{2-}]$.

For the air-side concentration of CO_2, an indoor value of 600 ppmv is estimated which leads to $[CO_2]_{w,tot} = 2 \cdot 10^{-5}$ M in the water, assuming $\alpha(CO_2) = 0.8$ [Sander, 2015]. Furthermore, $[Cl^-] = 0$ is set at first. With this, the calculation is performed for three different concentrations of the dyes ($[I]_{tot} = [T]_{tot} = 5 \cdot 10^{-5}\,M, 10^{-4}\,M, 2 \cdot 10^{-4}\,M$) as a function of $[NH_3]_{w,tot}$. The choice $[T]_{tot} = [I]_{tot}$ was experimentally found to be a good compromise between the reduction of the background fluorescence signal and the penetration depth of the excitation light. The initial pH value pH_{start} is found with the calculation for $[NH_3]_{w,tot} = 0$, which corresponds to the situation before the invasion experiment.

Figure 3.4 (a) shows the results of the calculations for $[I^-]$, where the initial pH values are found to be around $pH_{start} \simeq 5.5$. The curves in Fig. 3.4 (a) confirm the linear relationship between $[I^-]$ and $[NH_3]_{w,tot}$. They also show that with the assumed concentrations of pyranine, an initial pH value of $pH_{start} \simeq 5.5$ is sufficient to justify $[I]_{tot} \gg [H_3O^+], [OH^-]$. Thus, the addition of HCl is not needed after the dyes have been added to the water at first. The flattening occurring if $[NH_3]_{w,tot} \gg$

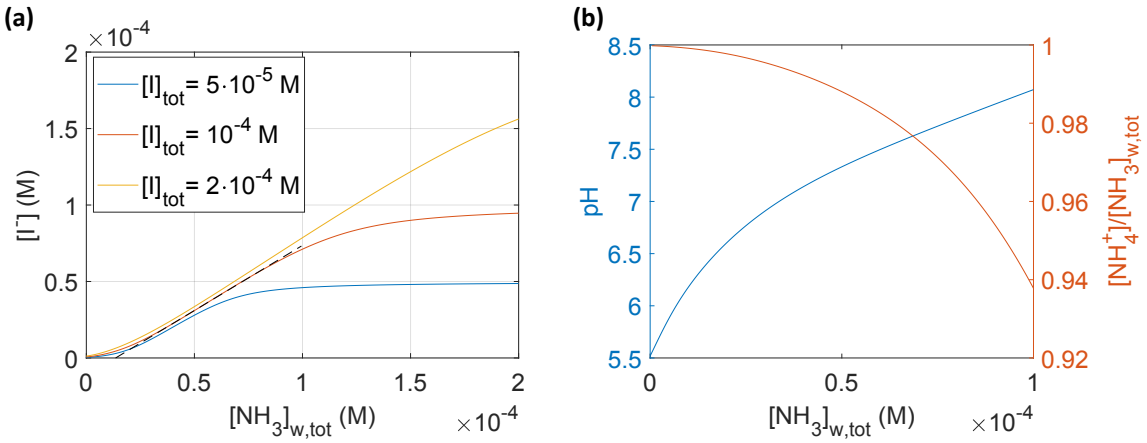

Fig. 3.4: (a) Results of the calculations showing the concentration of the alkaline pyranine component $[I^-]$ versus the total water-side ammonia concentration $[NH_3]_{w,tot}$ for different total pyranine concentraions $[I]_{tot}$. The dashed line indicates a linear fit applied to the curve calculated with $[I]_{tot} = 10^{-4}\,M$ chosen for the experiments. (b) Calculated results of the pH and the ratio $[NH_4^+]/[NH_3]_{w,tot}$ versus $[NH_3]_{w,tot}$ for $[I]_{tot} = 10^{-4}\,M$. The other input parameters for the calculations are mentioned in the text.

$[I]_{tot}$ demonstrates the case of saturation when nearly all pyranine molecules are in the alkaline form ($[I^-] \approx [I]_{tot}$). This means that the total pyranine concentration defines a threshold of the amount of (local) ammonia uptake without leaving the linear regime. Obviously, a high $[I]_{tot}$ is favorable. But a high pyranine concentration also leads to a significant absorption of the excitation light by pyranine itself, such that less light reaches deeper layers. Considering this, $[I]_{tot} = [T]_{tot} = 10^{-4}\,M$ and $pH_{start} \simeq 5.5$ were found to be the optimum parameters and will be assumed for further discussion. A linear fit is applied to the curve that was calculated with these parameters (see Fig. 3.4), yielding a proportionality factor of

$$a_{NH3,I^-} = 0.85 \pm 0.03, \tag{3.15}$$

with an estimated uncertainty. This value serves as a reference. Evidently, the proportionality factor for the acidic component is given by $a_{NH3,IH} = -a_{NH3,I^-}$. Using this proportionality, the (local) change of the water-side ammonia concentration during an invasion experiment is given by

$$\Delta[NH_3]_{w,tot} = [NH_3]_{w,tot} - [NH_3]_{w,tot,start} = \frac{1}{a_{NH3,I^-}}\Delta[I^-] = \frac{1}{a_{NH3,I^-}}([I^-] - [I^-]_{start}), \tag{3.16}$$

with the initial concentrations $[NH_3]_{w,tot,start}$ and $[I^-]_{start}$ at the beginning of the experiment. Figure 3.4 (b) shows for the chosen set of parameters that the approximation $[NH_3]_{w,tot} \approx [NH_4^+]$ is valid with a maximum error of about 5 % for $pH \lesssim 8$.

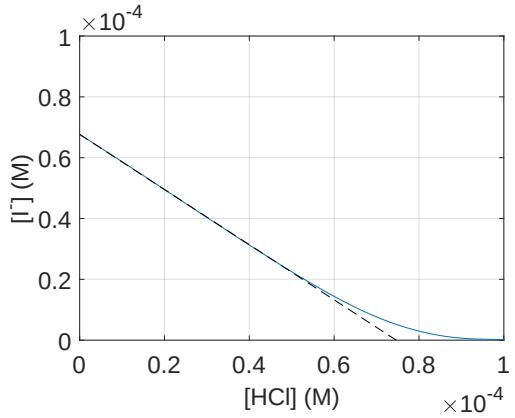

Fig. 3.5: Calculated concentration of the alkaline pyranine component I^- as a function of the concentration of added HCl for the set of parameters chosen for the experiments. Moreover, a total ammonia concentration of $[NH_3]_{w,tot} = 10^{-4}\,M$ is assumed to model the situation after an invasion experiment.

After the invasion, the concentrations of the substances in the water equilibrate. If the pH value does not exceeded ~ 8, the dissolved ammonia molecules stay mostly in their protonated form and do not participate in acid-base reaction. The concentration of the alkaline pyranine component has changed by $\Delta[I^-]$. By adding an amount of HCl solution to the water that corresponds to a concentration of $[HCl] \approx \Delta[I^-]$, the initial state of the chemical system is restored, as HCl provides H^+ ions that protonate the alkaline pyranine component. This suggests a linear relationship between the concentrations of the two substances. This is confirmed by performing the above calculation as a function of added [HCl]. For this, the total concentrations of the dyes and CO_2 are chosen as above. Furthermore it is assumed that ammonia is dissolved in the water in a concentration of $[NH_3]_{w,tot} = 1 \cdot 10^{-4}\,M$ to model the situation after the invasion. The resulting curve is shown in Fig. 3.5. The linear fit yields a proportionality factor of

$$a_{HCl,I^-} = -(0.91 \pm 0.03). \tag{3.17}$$

This relation makes it possible to prepare the chemical system after an invasion experiment in a defined way. Thus, several subsequent experiments can be conducted with one solution.

3.4 Mass balance

With mass balance methods, the temporal evolution of the air- and water-side concentrations of a gas during a gas exchange experiment can be related to each other. In the box model (for more details see e.g. [Mesarchaki et al., 2014]), the air space and the water body are modeled as two closed well-mixed compartments as sketched in Fig. 3.6. Gas can be exchanged between the air volume V_a and the water volume V_w through the water surface A_{ws}, where the air- and water-side bulk concentrations are denoted by c_a and c_w, respectively. Moreover, a gas input quantified by $\dot{V}_i c_i$ with

the input rate $\dot{V}_\mathrm{i}$ and the input concentration c_i as well as a leaking volume flow rate $\dot{V}_\mathrm{leak}$ are assumed. The latter accounts for the fact that in real experiments the air space is not perfectly gas-tight. Assuming constant volumes, temperature and pressure conditions, the mass balance for the air-side point of view can be written as

$$V_\mathrm{a}\dot{c}_\mathrm{a} = -A_\mathrm{ws} \cdot k_\mathrm{tot,a} \cdot \left(c_\mathrm{a} - \frac{c_\mathrm{w}}{\alpha}\right) + \dot{V}_\mathrm{i}c_\mathrm{i} - \dot{V}_\mathrm{leak}c_\mathrm{a}, \tag{3.18a}$$

$$V_\mathrm{w}\dot{c}_\mathrm{w} = A_\mathrm{ws} \cdot k_\mathrm{tot,a} \cdot \left(c_\mathrm{a} - \frac{c_\mathrm{w}}{\alpha}\right), \tag{3.18b}$$

where $k_\mathrm{tot,a}$ denotes total transfer velocity for the air-side perspective, averaged over the whole water surface.

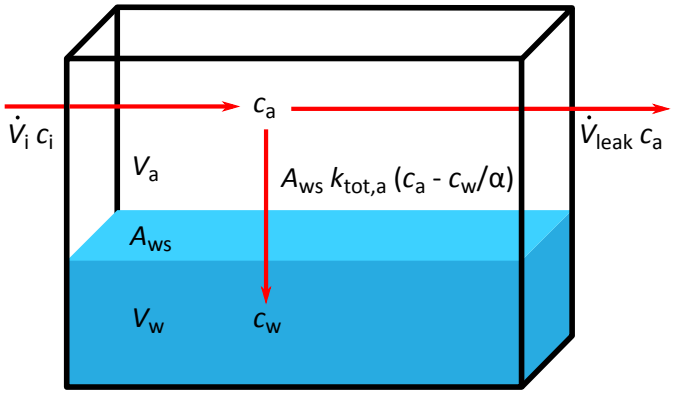

Fig. 3.6: Illustration of the box model for an invasion experiment with the air- and water-side concentrations c_a and c_w and the volumes of the air and the water space V_a and V_w. The two compartments are in contact through the water surface A_ws. The arrows indicate the temporal change of c_a, which is given by the gas tranfer into the water as well as the input and the leaking volume flow rate (modified after [Friedl, 2013]).

With the approximation $c_\mathrm{a} \gg \frac{c_\mathrm{w}}{\alpha}$ for highly soluble gases like ammonia, the differential equations decouple, leading to a simplified air-side mass balance

$$0 = \dot{c}_\mathrm{a} + \left(\frac{A_\mathrm{ws} \cdot k_\mathrm{tot,a}}{V_\mathrm{a}} + \frac{\dot{V}_\mathrm{leak}}{V_\mathrm{a}}\right) c_\mathrm{a} - \frac{\dot{V}_\mathrm{i}}{V_\mathrm{a}} c_\mathrm{i}. \tag{3.19}$$

The solution of this differential equation reads

$$c_\mathrm{a}(t) = \left(c_0 - \frac{\dot{V}_\mathrm{i}c_\mathrm{i}}{A_\mathrm{ws}k_\mathrm{tot,a} + \dot{V}_\mathrm{leak}}\right) \exp(-\lambda_\mathrm{a}t) + \frac{\dot{V}_\mathrm{i}c_\mathrm{i}}{A_\mathrm{ws}k_\mathrm{tot,a} + \dot{V}_\mathrm{leak}}, \tag{3.20}$$

assuming an initial air-side concentration c_0. The decay rate is defined as $\lambda_\mathrm{a} = \frac{A_\mathrm{ws} k_\mathrm{tot,a}}{V_\mathrm{a}} + \frac{\dot{V}_\mathrm{leak}}{V_\mathrm{a}}$. Fitting the function Eq. 3.19 to the measured time-dependent air-side concentration, gives λ_a which can be used to determine the transfer velocity according to

$$k_\mathrm{tot,a} = h_\mathrm{a} \left(\lambda_\mathrm{a} - \lambda_\mathrm{leak}\right), \tag{3.21}$$

with the effective height of the air space $h_\mathrm{a} = V_\mathrm{a}/A_\mathrm{ws}$. The leakage rate $\lambda_\mathrm{leak} = \frac{\dot{V}_\mathrm{leak}}{V_\mathrm{a}}$ of the used wind-wave tunnel can be measured in a separate experiment (see Sec. 5.3) by monitoring the air-side concentration of an insoluble gas, since its decay is only caused by leaks.

If the input flow rate is switched off, Eq. 3.19 reduces to

$$0 = \dot{c}_\mathrm{a} + \left(\frac{A_\mathrm{ws} \cdot k_\mathrm{tot,a}}{V_\mathrm{a}} + \frac{\dot{V}_\mathrm{leak}}{V_\mathrm{a}}\right) c_\mathrm{a}, \tag{3.22a}$$

$$\Rightarrow c_\mathrm{a}(t) = c_0 \exp(-\lambda_\mathrm{a} t). \tag{3.22b}$$

4. Setup

In this chapter details of the measurement setup for the invasion experiments with ammonia are addressed. The used linear wind-wave tunnel and the current instrumentation including the spectroscopy setups are presented first. With the spectroscopy, the air-side concentration of ammonia and the water-side concentrations of the dyes are measured. Afterwards the imaging setups are discussed which comprise lighting and cameras for the BLI (boundary layer imaging) and the LIF (laser-induced fluorescence) method to acquire images of the fluorescence signal of pyranine.

4.1 Linear wind-wave tunnel

The invasion experiments were conducted at the Heidelberg linear wind-wave tunnel at the Institute for Environmental Physics in Heidelberg. Details on this tunnel can be found in [Herzog, 2010], where the tunnel is called LIZARD (linear strong acid resistant device). The setup was further upgraded in the scope of this thesis. A schematic sketch of the tunnel with the current instrumentation is shown in Fig. 4.1. The glass windows at the water segment allow for optical measurements from the side, the top and the bottom. Moreover, the materials used at the inside of the tunnel have an excellent chemical resistance against acids and bases, such that ammonia can be used as a trace gas. The properties of the tunnel and the current instrumentation are presented in the following. The imaging setups will be discussed separately in Sec. 4.2.

4.1.1 General properties

The wind-wave tunnel consists of a water segment which is in contact with an enclosed air space. It has an air volume of $(3.0 \pm 0.3)\,\mathrm{m}^3$ and a water volume of $(123 \pm 6)\,\mathrm{l}$ including the water in the bypasses. The inside surface area is about $20\,\mathrm{m}^2$.

An axial fan in the air recirculation part of the tunnel serves as a wind engine. Its rotation frequency can be adjusted by an electronic frequency converter (*Sinamics G110* by *Siemens*) in a range from 0 Hz to 50 Hz. The frequency of the wind engine will be synonymously referred to as the wind frequency in this thesis. The so called honeycomb is a grid structure with a mesh size of 3 cm, which reduces unwanted disturbances of the mean air flow. The jet inlet installed after the honeycomb further

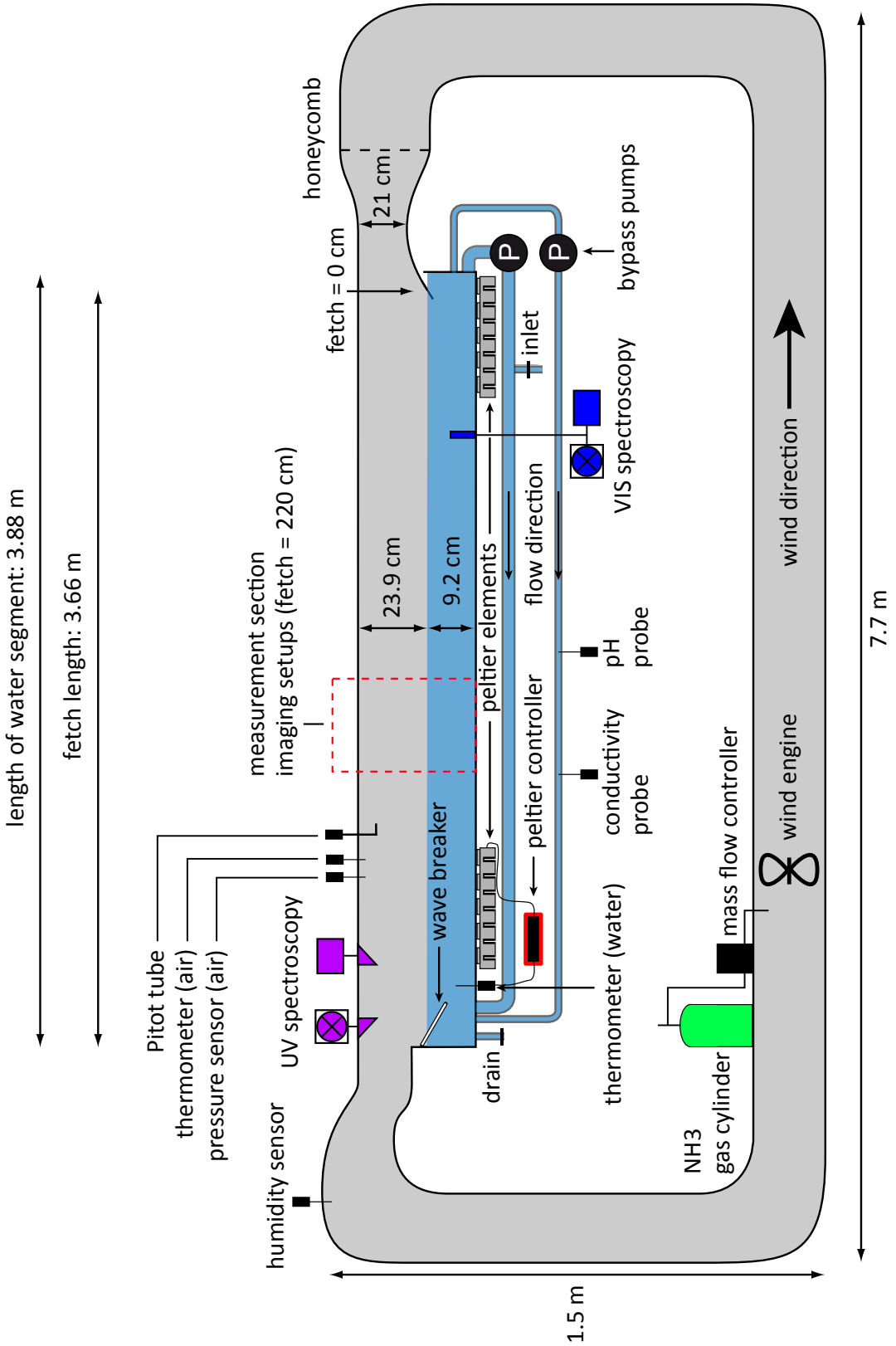

Fig. 4.1: Schematic illustration of the Heidelberg linear wind-wave tunnel from the side with the instrumentation used in this thesis (modified after [Friedl, 2013]).

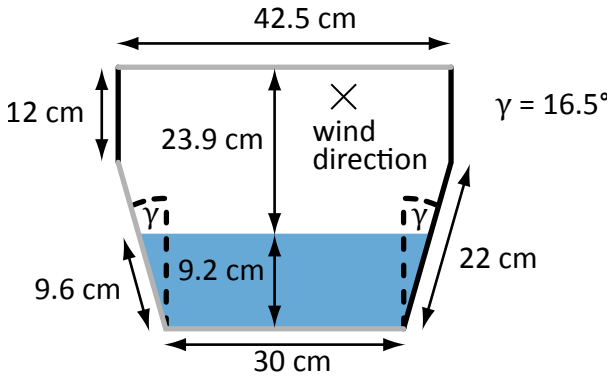

Fig. 4.2: Sketch showing the cross section of the water segment of the wind-wave tunnel as viewed in the wind direction. Walls with glass windows are depicted in gray, walls without in black (modified after [Friedl, 2013]).

reduces inhomogeneities by contracting the streamlines of the air flow.

Fig. 4.2 shows a sketch of the cross section of the water segment, which has a length of 3.88 m. The maximum fetch in the tunnel is 3.66 m. In the scope of this thesis a reproducible standard water level of $z_{\mathrm{ws},0} = 9.2\,\mathrm{cm}$, indicated by a mark at the tunnel, was used for the measurements. With this, the water segment without the bypass loops contains 116.8 l. The surface area is about $1.38\,\mathrm{m}^2$. If the water segment is filled, only wind frequencies up to $\sim 25\,\mathrm{Hz}$ are usable to avoid an overflow after the wave breaker. The sidewalls are tilted by an angle of $\gamma = 16.5\,^\circ$. Windows on the top, the bottom and the side, which have a thickness of 6.5 mm and are made out of borosilicate glass (*Borofloat 33* by *Schott*), allow for optical accessibility for fetches between 35 cm and 255 cm. The measurement section for this thesis is located at a fetch of 220 cm. The tilted window on the side makes it possible to observe the water surface from below even at wavy conditions. A wave breaker made out of PTFE half tubes is placed at the downstream end of the water segment to suppress reflections of the waves.

The linear shape of the water segment leads to a logarithmic wind profile above the water surface. For the measurements conducted in this thesis, the wind frequency was set to 15 Hz resulting in a medium plateau wind speed of about 4 m/s. According to the measurement results of [Friedl, 2013], the air-side friction velocity at the used fetch and wind frequency is given by $u_{*,\mathrm{a}} = 22\,\mathrm{cm/s}$.

Two water bypass loops, a circulation loop and a so called analysis loop, driven by pumps are used. The flow direction is indicated by arrows in Fig. 4.1. Both loops are continuously flushed during an invasion experiment. The circulation loop (see the uppermost loop in Fig. 4.1) contains a water volume of approximately 6 l and is used to mix the water bulk. In this way, chemicals added to the water become equally

distributed quickly. This is especially important for the experiments, since the water bulk is assumed to be well mixed, as described in Sec. 2.2.1. Apart from that, a continuous circulation of the water is important to equilibrate the water temperature when the Peltier temperature control (see Sec. 4.1.2) is active. The water flow is driven by an integrated centrifugal pump (*MPN 101* by Schweiker) with a maximum flow rate of $80\,\mathrm{L\,min^{-1}}$. An electronic frequency converter of the same type as used for the wind engine enables one to set its rotation frequency. In the experiments deionized water with initially pH $\simeq 5.5$ and a conductivity $\kappa \lesssim 0.1\,\mu\mathrm{S/cm}$ was used. The smaller analysis loop has a volume of approximately 490 ml and is used to measure the pH and the conductivity of the water. A magnetically coupled rotary pump (*RS-Components*) with a maximum flow rate of $14\,\mathrm{L\,min^{-1}}$ flushes the loop with water from the basin.

4.1.2 Instrumentation

The following section gives an overview of the current instrumentation at the wind-wave tunnel that is used besides the imaging setups.

Peripheral instruments

With the peripheral instruments, the pH and the conductivity of the water are measured. Moreover, instruments are used that monitor the measurement conditions in the wind-wave tunnel including the air- and the water-side temperatures, the air humidity, the air pressure and the wind speed. The devices are connected via USB to a PC and read out in parallel with a *Heurisko* worksheet.

pH probe The pH value is monitored by a pH probe (*GE 104* with *GMH 3530* by *Greisinger*). Details on the potentiometric measurement principle can be found e.g. in [Karastogianni et al., 2016]. The used pH electrode is suitable for measurements in unstirred or slightly stirred solutions only. A pH combination electrode is used which contains the measurement and the reference electrode and is appropriate for pH measurements in water with low conductivity. It is installed in the analysis loop. In unstirred solution, the measurement uncertainty of the pH probe is typically ± 0.05. Test measurements showed that, when the bypass pump is active, the pH probe measures values that are systematically lower by about 0.3 compared to the case when the pump is inactive. This can be explained by the fact that the flow in the loop disturbs the outflow of reference electrolyte and thus the voltage drop at the porous diaphragm which ensures electrical contact between the reference electrode and the solution to be mea-

sured. Since the calibration is done externally with unstirred buffer solutions, the values measured when the pump is active are corrected by the offset.

conductivity probe A conductivity probe (*LF 200 RW* with *GMH 5430* by *Greisinger*) is used to measure the conductivity of the water. The electrode is suitable for (ultra) pure water and installed in the analysis loop. The typical uncertainty of the measurements is 0.1 µS/cm. The conductivity value is used as a measure for the ion concentration in the water.

thermometers The air- and the water-side temperatures are measured with precision thermometers (*PT100* sensor with *GMH 3710* by *Greisinger*). The sensors are installed at the downstream end of the water segment. The thermometers have a tolerance of ±0.03 °C at 0 °C.

humidity sensor The relative humidity of the air in the tunnel is measured by a humidity sensor (*HC2-S* by *Rotronic*) installed in the air space behind the wave breaker.

pressure sensor A pressure sensor (*GMSD 1.3 BA* with *GMH 3110* by Greisinger) is installed on the air side near the thermometer to measure the static pressure inside the wind-wave tunnel with a resolution of 1 mbar.

Pitot tube To recognize possible variations of the wind field in the wind-wave tunnel, the wind speed is measured using an L-shaped Pitot tube with a differential pressure transducer (*DIFF-CAP* by *Special Instruments*). The transducer is connected to an A-D converter (*RedLab* by *Meilhaus Electronic*). More details on the functioning of the Pitot tube can be found in [Kundu et al., 2012]. The Pitot tube is installed 11 cm above the resting water surface at a fetch of 255 cm. With the differential pressure p_{diff} of the Pitot tube and the air density ρ_{a}, the wind speed u is determined according to

$$u = \sqrt{\frac{2 \cdot p_{\mathrm{diff}}}{\rho_{\mathrm{a}}}}. \tag{4.1}$$

To calculate the air density

$$\rho_{\mathrm{a}} = \frac{p_{\mathrm{a}}}{R_{\mathrm{ha}} \cdot T_{\mathrm{a}}}, \tag{4.2}$$

measurement data of the air-side temperature T_{a}, pressure p_{a} and relative humidity H_{a} are needed. The gas constant of humid air is given by

$$R_{\mathrm{ha}} = \frac{R_{\mathrm{a}}}{1 - H_{\mathrm{a}} \cdot p_{\mathrm{v}}(T_{\mathrm{a}})/p_{\mathrm{a}} \cdot (1 - R_{\mathrm{a}}/R_{\mathrm{v}})}, \tag{4.3}$$

where $R_{\mathrm{a}} = 287.1\,\mathrm{J/(kg \cdot K)}$ and $R_{\mathrm{v}} = 461.5\,\mathrm{J/(kg \cdot K)}$ denote the gas constants of dry air and water vapor, respectively [Wallace and Hobbs, 1977]. The

saturation vapor pressure of water as a function of the air temperature $p_v(T_a)$ is approximated according to the empirical Magnus formula [Sonntag, 1990]

$$p_v(T_a) = 6.112\,\text{hPa} \cdot \exp\left(\frac{17.62 \cdot T_a}{243.12\,°\text{C} + T_a}\right), \quad -45\,°\text{C} \leq T_a \leq 60\,°\text{C}. \tag{4.4}$$

The wind speed measured at that height corresponds to the plateau wind speed of the wind profile in the tunnel that was systematically investigated by [Friedl, 2013].

Peltier temperature control

When the tunnel filled with water is closed, the air space becomes quickly saturated with water vapor. To avoid condensation at the inside of the tunnel walls and the windows, the water needs to be cooled. Condensation would lead to misting of the windows and water films at the tunnel walls, where gaseous ammonia can dissolve. This would distort the mass balance.

Cooling is achieved with two Peltier temperature control units which are installed below the bottom of the water segment as shown in Fig. 4.1. Each unit is mounted between an aluminum plate embedded in the bottom of the water segment and a cooling element. The aluminum plate provides thermal contact to the water. The cooling element ($380 \times 280 \times 50\,\text{mm}^3$) consists of cooling ribs and a tangential fan, which improves the heat exchange with the ambient air.

Each Peltier unit consists of 24 Peltier elements (*QC-127-2.0-15.0M* by *Cooltronic*). The two units are supplied by a Peltier controller (*TC2812* by *Cooltronic*) with an integrated PID (proportional–integral–derivative) controller. By means of the Peltier temperature control, a constant temperature of the water in the tunnel is maintained with a precision of $\pm 0.1\,°\text{C}$.

Input of ammonia

For the gas input, a gas cylinder with ammonia is connected via a mass flow controller (model *35828S* by *Analyt-MTC*) to the air space of the tunnel in front of the wind engine. During an experiment the wind engine is already active before gas is let into the tunnel. When the gas input is activated, the fan helps with mixing the ammonia. With the mass flow controller, flow rates up to 200 ml/min can be set. According to the manufacturer the uncertainty ΔF_{set} of the set value F_{set} in ml/min is given by

$$\Delta F_{set} = \pm(0.8\,\% \cdot F_{set} + 0.2\,\% \cdot 200\,\text{ml/min}). \tag{4.5}$$

Input of dry air with low CO_2 concentration and exhaust

Since for the measurements the initial pH value is set near the neutral point, the chemical system is sensitive to CO_2 that enters the water from the air volume. To minimize this effect, the CO_2 concentration in the air space of the wind-wave tunnel is lowered. This is done by flushing the air space between the measurements with dry air which has a relative humidity of less than 1 % and a low CO_2 concentration of roughly 40 ppmv. At the same time an exhaust tube is connected to the air space and the wind engine is active with a frequency of 10 Hz − 15 Hz for mixing. The input of dry air also reduces the humidity so that condensation at the inner sides of the tunnel walls is suppressed.

Spectroscopy

The spectroscopy setups were newly installed at the wind-wave tunnel. With the air-side setup, the bulk concentration of gaseous ammonia is inferred by measuring its absorption spectrum in the ultraviolet (UV) wavelength range. Similarly, the water-side setup makes it possible to determine the concentration of the dyes in the water bulk by exploiting their absorption characteristics in the visible (VIS) range. Each setup consists of a light source and a spectrometer. Both spectrometers are controlled and read out in turns with a *Matlab* script. For each setup, a dark spectrum, accounting for the dark current of the respective spectrometer, is subtracted from the recorded spectra. The integration times of the spectrometers are adjusted in order to obtain an optimal signal to noise ratio. For each spectrum that is saved, several spectra are recorded and averaged to reduce noise further. Their number is set such that a good compromise between noise reduction and time resolution is found. With this, one measurement cycle including the data acquisition of both spectrometers is performed within a time period of about 1 s. With the integrated real-time evaluation of the script, concentration values from the measured spectra are determined directly.

Air-side UV spectroscopy As shown in Fig. 4.1, the UV spectroscopy setup is installed in the air space above the wave breaker. Fig. 4.3 (a) shows a detailed illustration of the setup. The optical path from the UV light source to the UV spectrometer (*Maya Pro 2000* by *Ocean Optics*) is indicated by the violet arrow. Fig. 4.3 (b) shows the spectrum of the light source. The absorption path with a length of (93.0 ± 0.5) cm is defined by two UV-transparent reflecting prisms which are fixed to stainless steel cylinders mounted in holes in the top of the tunnel. Each cylinder has a central through bore and is pressed against the wall by a threaded ring from the outside. The UV light source is attached

to one of the cylinders via a lens barrel where the lenses focus and collimate the light beam. The light source has cooling ribs and is in addition actively cooled by a fan. At the receiving end, the light is focused by a lens on the tip of an optical fibre that is connected to the UV spectrometer. The used fiber (*QP 600-025-SR-BX* by *Ocean Optics*) is particularly suitable for UV light.

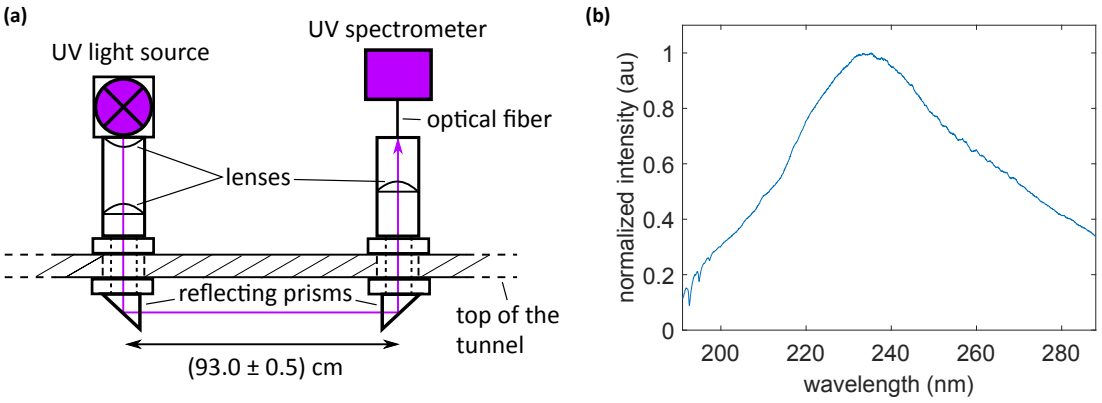

Fig. 4.3: (a) Schematic illustration of the UV spectroscopy setup with the absorption length of (93.0 ± 0.5) cm between two reflecting prisms. These are fixed to stainless steel cylinders that are mounted at the top of the tunnel. Lenses are used to focus and collimate the light coming from the UV light source. At the receiving end, a lens focuses the light on the tip of an optical fiber, which is connected to the UV spectrometer. (b) Spectrum of the UV light source.

Water-side VIS spectroscopy The core of the VIS spectroscopy setup is a transmission probe (*T300-RT-UV-VIS* by *Ocean Optics*), which is schematically illustrated in Fig. 4.4 (a). It consists of two optical fibers that are joined at a Y junction and lead to a measurement probe made out of stainless steel. The probe is submerged in the solution of which the absorption is to be measured. One fiber is connected to the VIS spectrometer (*USB 4000* by *Ocean Optics*), which has a sufficient resolution for the absorption bands of the used dyes. The other fiber is connected to the VIS light source, which is an LED lamp. Its spectrum is shown in Fig 4.4 (b). The lamp consists of two LED arrays which are mounted on the opposite sides of an aluminum cylinder. Each array consists of seven compact, high-power LEDs (type *LUXEON Z Color Line* and *LUXEON UV U Line* by *Lumileds*) in the wavelength range $\lambda = 380\,\text{nm} - 500\,\text{nm}$. The wavelength range matches the spectral location of the absorption features of pyranine and tartrazine (cf. Fig. 3.2). The LED light is directed into a hollow spherical cavity called *Ulbricht sphere* inside the aluminum cylinder. The inside of this cavity is covered with a diffuse white reflective coating such that the

LED light of the point-like sources is turned into diffuse, homogeneous light. This is the output of the LED lamp. As indicated by blue arrows in Fig. 4.4, the light of the lamp is guided to the measurement probe. At the end of the probe a measurement tip with a 2 mm gap and a mirror is mounted. The gap allows for free flow of the solution and corresponds to half of the absorption length, as the light coming from the light source is reflected by the mirror to the fiber that is connected to the spectrometer. The probe is installed in the water bulk at the upstream end of the wind-wave tunnel (see Fig. 4.1).

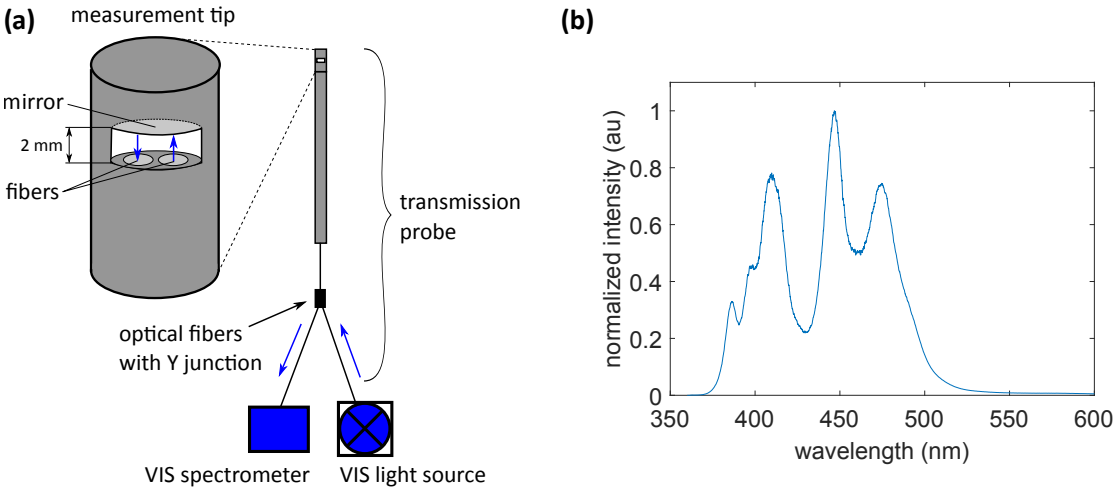

Fig. 4.4: (a) Schematic illustration of the VIS spectroscopy setup with the transmission probe that is connected to a spectrometer and the VIS light source, which is an LED lamp. The zoom in shows details of the measurement tip. (b) Spectrum of the VIS light source.

4.2 Imaging setups

The sketches in Fig. 4.5 (a) and (b) show the used imaging setups at the Heidelberg linear wind-wave tunnel from two different perspectives. The setup is located at a fetch of 220 cm (cf. Fig. 4.1) corresponding to the downstream end of the optically accessible part of the water segment where the waves are the highest. A rail system, that surrounds the wind-wave tunnel and is not shown in Fig. 4.5 for reasons of clarity, allows for a flexible displacement of the whole setup in wind direction. In the measurement section, the illumination and the cameras for the BLI and the LIF method are installed to image the fluorescence intensity of pyranine during the invasion experiment with ammonia. In order to provide an overview of the whole setup, the geometric arrangement of the single components is discussed first. After that, details on the components of the BLI and the LIF setup are given. Finally, the

camera settings and the triggering of the imaging setups are addressed.

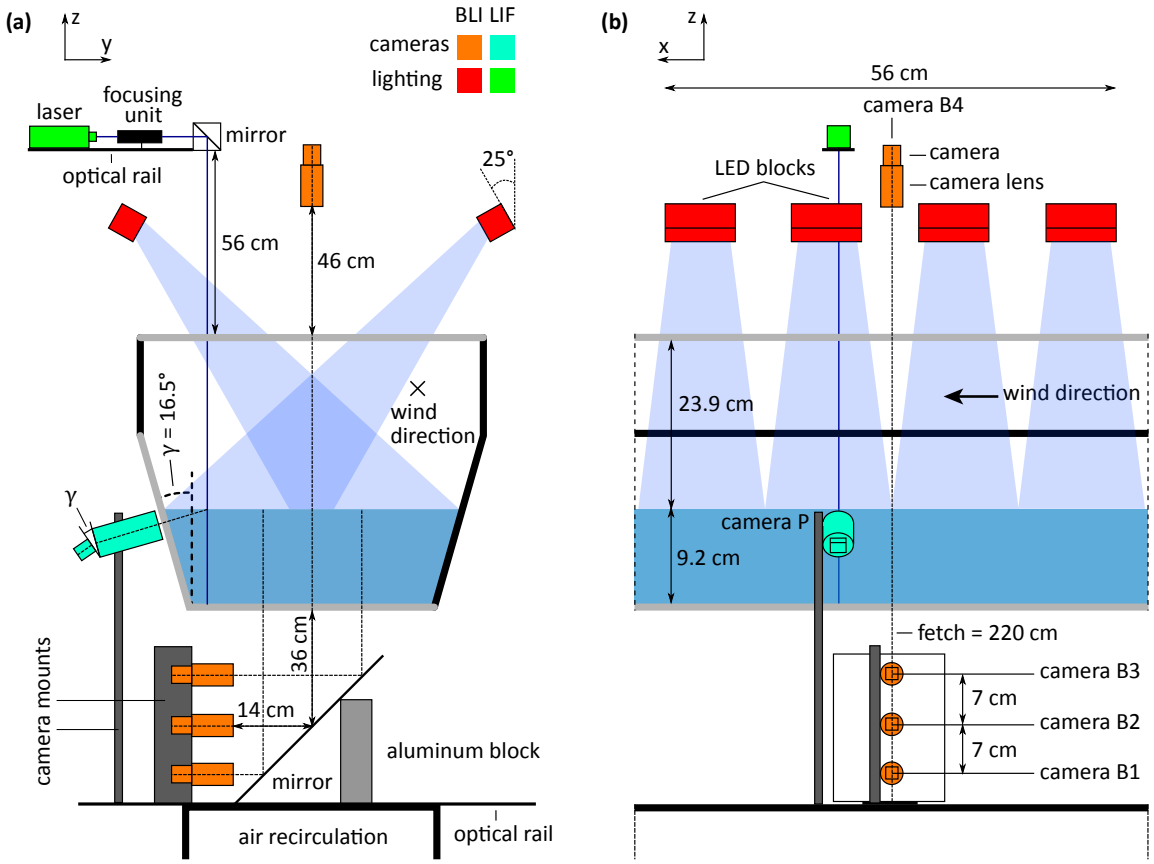

Fig. 4.5: Sketch of the imaging setups used at the Heidelberg linear wind-wave tunnel, where (a) shows the view in wind direction and (b) the view perpendicular to the wind direction. Glass windows and non-transparent walls are indicated by gray and black lines, respectively. The BLI setup includes eight LED blocks and cameras looking from below (B1, B2, B3) and from above (B4) the water segment. The LIF setup consists of a tilted camera (P) looking from the side at a vertical laser beam. The coordinate system and a color legend are shown at the top.

4.2.1 Geometric arrangement

Several cameras looking from different sides of the water segment are installed: Four BLI cameras, of which three are installed below (B1, B2 and B3) and one above (B4) the wind-wave tunnel, and a profile camera at the side (P). Each camera is depicted with its corresponding camera lens as indicated explicitly in Fig. 4.5 (b) for the top BLI camera B4. The optical axis of a camera is indicated by a dashed line.

For the BLI setup, eight blue LED light sources (LED blocks), of which four are mounted on each side of the wind-wave tunnel at an angle of 25° with respect to the vertical axis, provide the illumination of the water surface. The angle is adjusted in such a way that the lighting at the center of the water surface is as homogeneous as possible. The bottom BLI cameras are mounted on a plate one above the other with a respective distance of 7 cm and look at the water surface via a high-quality mirror by *Edmund Optics* with an area of $20.5 \times 25.5\,\mathrm{cm}^2$. The mirror is mounted with an angle of 45 ° to the horizontal axis and can be freely displaced along an optical rail. The rail is placed on the lower air recirculation part of the wind-wave tunnel. The arrangement of the bottom cameras allows for flexible adjustment of their field of views and optimal utilization of the limited space below the water segment.

For the LIF setup, a blue laser light source, a focusing unit and a mirror, that directs the laser beam to the water surface, are installed on an optical rail above the wind tunnel. The profile camera, that looks at the beam, is tilted by the angle $\gamma = 16.5\,°$ such that the optical axis of its camera lens is perpendicular to the tilted side window. As shown in Fig. 4.5 (a), the sensor of the profile is mounted at the angle γ with respect to the camera lens. The reason for the special orientation of the lens and the sensor will be explained in 4.2.3.

Figure 4.6 illustrates the fluorescence signals that are acquired with the BLI and the LIF setup. As mentioned in Sec. 3.1, only the alkaline form of pyranine I^- is supposed to be excited which is ensured by choosing appropriate light sources that will be characterized in the next sections. During the invasion experiment with ammonia, the concentration $[I^-]$ and correspondingly the visible fluorescence intensity increase.

The LED light $I_{0,\mathrm{LED}}(\lambda)$ of the BLI setup excites I^- in the illuminated water patch, where its intensity decreases with depth due to absorption by pyranine and tartrazine. With the BLI cameras, horizontal images are recorded. Each camera sees a certain fraction of the fluorescence intensity $\hat{I}_\mathrm{F}(L)$ integrated along the water column with a length $L = 9.2\,\mathrm{cm}$ (cf. Sec. 2.81). The fluorescence is emitted isotropically by the I^- molecules. Moreover, a fraction of the transmitted light $I_{\mathrm{T,LED}}(\lambda, L)$ reaches the bottom cameras, while a fraction of the incident LED light $I_{\mathrm{R,LED}}(\lambda)$ may be reflected to the top camera at wavy conditions. With the BLI setup, the mass boundary layer of ammonia entering the water and in particular, its accumulation in the form of streaks (cf. Sec. 2.2.3) is made visible by the fluorescence.

Light with the spectrum $I_{0,\mathrm{laser}}(\lambda)$ emitted by the laser excites the fluorescence of I^- along the vertical beam, creating a depth-dependent fluorescence profile $\tilde{I}_\mathrm{F}(z)$ (cf. Sec. 2.81). The profile is viewed by the profile camera. With this setup, the mass boundary layer is observed from the side and transport processes of the dissolved gas are resolved vertically.

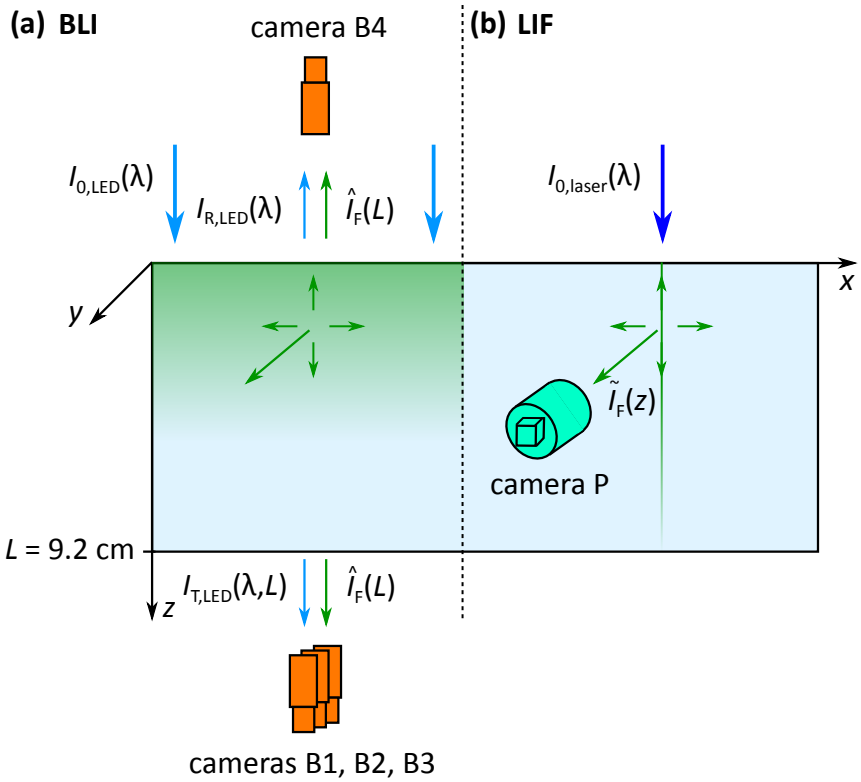

Fig. 4.6: Scheme illustrating which fluorescence signals are measured with the BLI (a) and the LIF (b) setup. The isotropy of the fluorescence of pyranine is indicated by the green arrows pointing in different directions. Details are given in the text.

4.2.2 BLI setup

This section addresses details on the lighting and the cameras used for the BLI setup.

LED light sources

To achieve high fluorescence intensities of pyranine in an alkaline solution, a light source with an emission spectrum matching the absorption spectrum of I^- is needed. The BLI light sources are LED blocks that were previously used for the BLI method in [Kräuter, 2015]. The LEDs (type *Osram OSLON SSL (blue)*) have a typical emission wavelength of $\lambda = 470\,\mathrm{nm}$. In each LED block ($11 \times 5.5 \times 6\,\mathrm{cm}^3$), which is made out of aluminum and provides passive cooling, four parallel rows with 9 LEDs each are installed. Two rows form an array where the LEDs are connected in series. The spectrum of such an array is shown in Fig. 4.7 (a) with the absorption coefficients of the two pyranine components. In order to avoid excitation of the acidic component IH, which significantly absorbs light below 440 nm, bandpass filters with a central

wavelength of 470 nm and a bandwidth of 35 nm (BP 470 nm × 35 nm by *Delta*) are integrated in the LED blocks. The transmission characteristic of this filter restricts the emission of the LEDs to $\lambda = 450\,\text{nm} - 490\,\text{nm}$ (see Fig. 4.7 (a)).

The LED arrays are controlled by a circuit with four channels, each supplying four arrays. Each channel provides a voltage of about 64 V and a current of 2.8 A such that each array can be operated at 700 mA. The controlling unit of the circuit is a programmable *Arduino* board (*Teensy 3.5*) that is connected via USB to a PC.

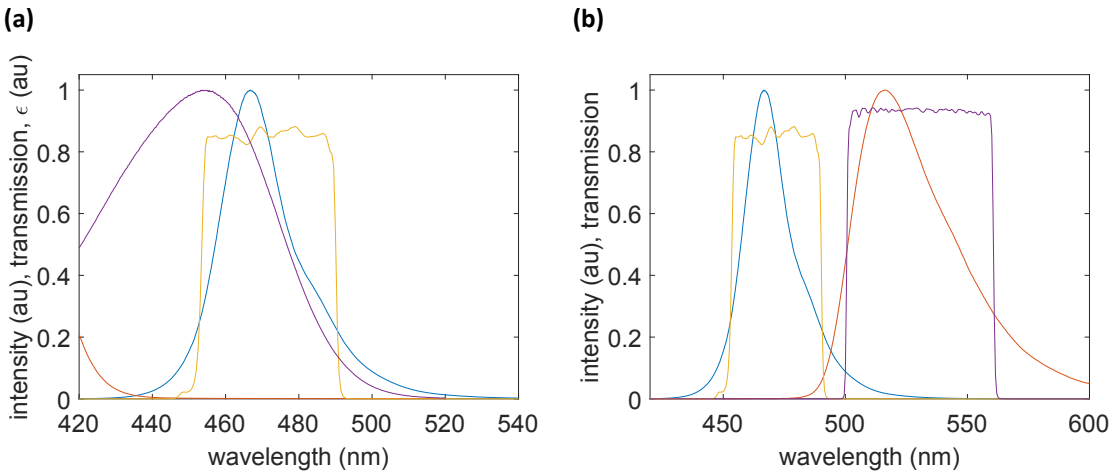

Fig. 4.7: (a) Spectrum of a blue LED array used for the BLI setup (blue), measured with a spectrometer, molar absorption coefficients ϵ of the two pyranine components IH (red) and I^- (purple) as in Fig. 3.2 (a) and transmission of one of the blue bandpass filters integrated in the LED blocks (yellow). (b) Spectrum of a blue LED array (blue) and transmission of a blue bandpass filter (yellow) as in (a). Furthermore, emission spectrum of pyranine (red) as in Fig. 3.2 (a) and transmission of a green bandpass filter used for the BLI cameras (purple). The transmission of the filters in (a) and (b) was measured with a spectrophotometer (see A.1).

Cameras

To image the fluorescence signal, compact, low-noise, monochrome area scan cameras (*acA1920-155um* by *Basler*) are used. Their CMOS sensors have 1920 × 1200 pixels with a pixel size of $5.86 \times 5.86\,\mu\text{m}^2$ and, according to the manufacturer, a typical quantum efficiency of 70%. The used camera lenses (*23FM25SP* by *Tamron*) have a minimal focal length of 25 mm and an aperture range of $1.4 - 22$. For the cameras of the BLI setup, green bandpass filters (BP 530 × 55 nm by *Edmund Optics*) are used. These block the residual light of the LEDs reaching the bottom cameras and suppress

reflections at the wavy water surface seen by the top camera (cf. Fig. 4.6). The green filters still allow most of the fluorescence light of pyranine to pass through. A good spectral separation between the unwanted excitation light and the fluorescence signal is achieved as illustrated in Fig. 4.7 (b).

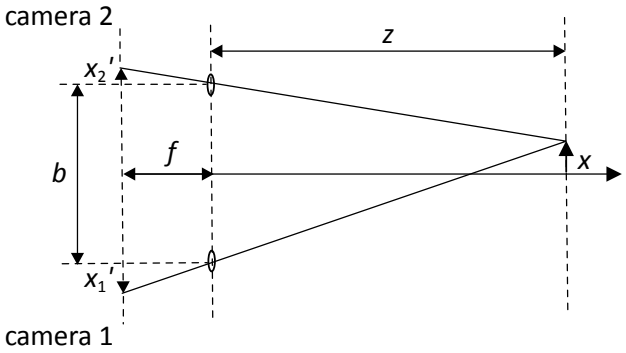

Fig. 4.8: Sketch of a general stereo-view geometry with two cameras placed a distance b apart. Their lenses have the same focal length f. The imaged object is at a distance $z \gg f$. The image positions on the image plane are denoted by x_1' and x_2' (modified after [Jähne, 2012]).

The idea of using several BLI cameras is that the fluorescent structures in the water-side mass boundary can be viewed from different perspectives which makes it possible to obtain depth information and compare the visibility of the structures seen from below and above. These aspects of the images recorded for this thesis are addressed by showing and discussing exemplary data. In particular, the present study aims to show that depth information can be obtained from the images recorded by the bottom cameras that form stereo pairs. A stereo-view geometry is illustrated in Fig. 4.8. Two cameras with parallel optical axes are placed a distance b apart, which is called the stereo basis. Both camera lenses have the same focal length f. The imaged object is at a distance $z \gg f$. The distance between the image positions x_1' and x_2' on the image plane, which is called the parallax p', is given by

$$p' = x_2' - x_1' = \frac{f \cdot b}{z} \tag{4.6}$$

[Jähne, 2012]. For the measurement setup, the parallax of a stereo pair observing an object directly at the resting water surface can be used as a reference. If objects are closer or further away by δz, the parallax will change by

$$\delta p' = -\frac{f \cdot b}{z^2} \delta z. \tag{4.7}$$

In total, three stereo pairs (B1, B2), (B2, B3) and (B1, B3) can be compared. The stereoscopic bases are $b_{1,2} = b_{2,3} = 7\,\text{cm}$ and $b_{1,3} = 14\,\text{cm}$, respectively. The image

size of the bottom cameras is adjusted such that a maximum overlap of their field of views is achieved.

4.2.3 LIF setup

In this section, details on the laser and the camera used for the LIF setup are given.

Laser

A diode laser (*Novapro 450-75* by *RGB Lasersysteme*) which was already used and characterized by [Friedl, 2013] is employed. The laser emits at a wavelength of $\lambda = (445 \pm 5)\,\mathrm{nm}$ and is therefore suitable to excite the alkaline form of pyranine I^- (see Fig. 4.7 (a)). The output power of the laser with a maximum value of about 79 mW is regulated by a controller with an input control voltage between 0 V and 5 V. The control voltage can be modulated with a frequency of up to 200 kHz. An integrated temperature control unit ensures a stable emission wavelength and beam shape. The compact design of the laser head ($60 \times 31 \times 31.5\,\mathrm{mm}^3$) and the controller ($85 \times 60 \times 28\,\mathrm{mm}^3$) facilitates the installation of the laser at places that are difficult to access.

Fig. 4.9 shows a cross section of the laser beam without any focusing elements, measured by [Friedl, 2013]. The laser is oriented in such a way that the direction along which the beam has a larger spatial extension (x-direction in Fig. 4.9) coincides with the wind direction (x-direction in Fig. 4.5 (b)).

Because of the high concentrations of the dyes, the vertical laser beam is significantly attenuated. Assuming $[I^-] = [I]_{tot} = 10^{-4}\,\mathrm{M}$ and $[TH] = [T]_{tot} = 10^{-4}\,\mathrm{M}$ and using the respective absorption coefficients in Fig. 3.2, the intensity of the beam is reduced to $1/e$ after the beam has passed about 1 mm in the water. As the fluorescence in the mass boundary layer is of interest, the beam can be only irradiated from above. This means that the position of the fluorescence profile changes when waves are present.

The beam emitted by the laser is focused by a focusing unit and directed by a mirror to the water surface. The focusing unit is positioned at a distance of 2 cm in front of the laser head and built after the principle of the Galilean telescope. It consists of a converging and a diverging lens that are placed in a lens barrel 6.5 cm apart and have focal lengths of 100 mm and 50 mm, respectively. Focusing the beam ensures a sufficiently high intensity, which allows for lower integration times.

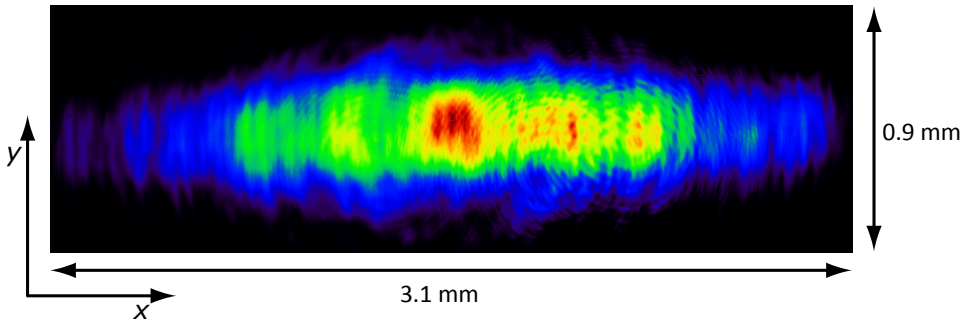

Fig. 4.9: Measured cross section of the laser beam used for the LIF setup [Friedl, 2013].

Profile camera

While the profile camera is of the same type as the cameras used for the BLI setup, the mounted lens is a telephoto macro lens (*AF Micro-Nikkor 200 mm 1:4D IF-ED* by *Nikon*). It has a focal length of 200 mm, an aperture range of $4 - 32$ and a maximum magnification factor of 1, which makes it possible to acquire images with a very high spatial resolution.

With the profile camera, that is mounted at the side of the wind-wave tunnel (see Fig. 4.5 (a)), the fluorescence profile created by the laser beam can be observed from below the water surface even at wavy conditions. This is made possible by the tilt of side window at an angle of $\gamma = 16.5\,^\circ$ with respect to the vertical. The plane of the camera lens needs to be parallel to the side window to avoid optical aberrations. To keep the vertical fluorescence profile in focus, also the image plane, i.e. the image sensor, needs to be tilted with respect to the lens plane. This optical arrangement is described by the Scheimpflug rule (see Fig. 4.10 (a)) from which the following condition for a sharp image is derived

$$\tan(\theta') = -m \tan(\theta) \tag{4.8}$$

[Jähne, 2012]. Here, m denotes the magnification factor and θ and θ' are the angles of the object and the image plane with respect to the lens plane, where $\theta = \gamma$ in the given measurement setup. The minus sign signals that the image plane is tilted in the opposite direction than the object plane. For $m = 1$ the absolute value of both angles is equal. In this setup, the distance and the focus of the lens are adjusted such that the limit $m = 1$ is reached. According to Eq. 4.8, it follows that the camera sensor needs to be mounted at an angle of $\theta' = \gamma$ with respect to the lens plane. This is realized with a tilted adapter.

Apart from these considerations, it has to be noted that the upper part of the fluorescence profile stays only visible if the optical axis of the camera does not intersect the water surface before it intersects the fluorescence profile. This means that the

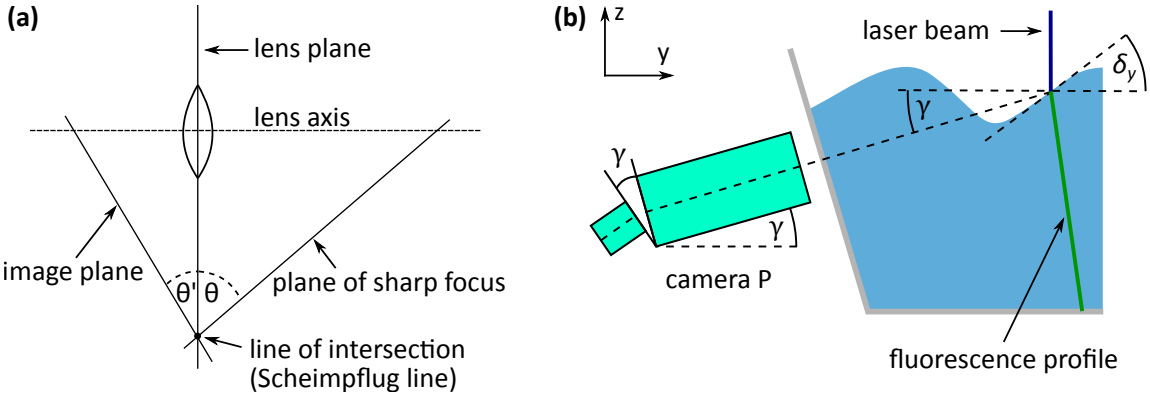

Fig. 4.10: (a) Sketch illustrating the Scheimpflug rule which states that if the image and the lens plane are not parallel, the plane of sharp focus is tilted, too. The three planes intersect in the Scheimpflug line. The angles θ and θ' are related by Eq. 4.8. (b) Sketch of the limiting case where the water surface is not visible to the profile camera (P). This case occurs if the inclination angle of the water surface in y-direction δ_y is greater than the angle γ by which the camera is tilted.

points on the water surface between the tilted side window and the point where the laser beam hits the water surface have to fulfill

$$\delta_y < \gamma, \tag{4.9}$$

where δ_y denotes the inclination angle in y-direction. This is exemplarily sketched in Fig. 4.10 (b) for the case where $\delta_y > \gamma$ at the intersection of the laser beam and the water surface. As only a moderate wind speed was used for the measurements, the level of turbulence and hence the inclination angle δ_y in the direction that is perpendicular to the wind direction were expected to be rather low which is why condition Eq. 4.9 was assumed to be fulfilled.

4.2.4 Camera settings and triggering

The speed at which data can be written to hard disks is the bottleneck for continuous recording of high resolution images at a high frame rate. Therefore, images are recorded in 8 bit format, even though the cameras have a dynamic range of 12 bit. To still make use of their full dynamic range, a lookup table (LUT) is used. It is based on the fact, that for high-quality cameras with low dark current noise, photon noise is the dominant noise contribution. Photon noise increases with the square root of the photon number (Poisson distribution) and hence with the gray value the camera measures. The lookup table corresponds to a non-linear, nearly lossless

transformation of gray values $g \in [0, 255]$ in the 8 bit range to values $g' \in [0, 4095]$ in the 12 bit range such that the noise at all new gray values is approximately equal (for more details see [Jähne, 2013]). During the image acquisition, the transformed images $G'(x, y)$ are saved. By applying the inverse transformation afterwards, the original images $G(x, y)$, where the gray values are proportional to the incident light, are reconstructed. The gray values in $G(x, y)$ are normalized to one. The resulting set of gray values between zero and one is denoted by g_{norm}.

camera	image size (px)	aperture	integration time (µs)	framerate (Hz)
B1	1540×470	2.0	500	400
B2	1900×470	2.0	500	400
B3	1124×470	2.0	500	400
B4	1900×470	2.0	400	400
P	1920×215	8.0	30	800

Table 4.1: Summary of the settings of the BLI (B1, B2, B3, B4) and the LIF (P) cameras. The image size is given in columns × lines of the image sensor.

To avoid interference between the BLI and the LIF setup, the lighting and the cameras are triggered by two separate pulse signals, provided by a function generator and temporally deferred with respect to each other. For this to work properly, the frequency of one signal needs to be an integer multiple of the other one. Besides, the time that is needed to read out the image sensor and write the acquired images to the hard drive has to be taken into account when choosing the acquisition frame rate and the image size. As the image sensor of the used cameras is read out line by line, the number of lines of the recorded images is decisive.

For the BLI setup, a frequency of 400 Hz and an image size with 470 lines are set. The image sections are chosen such that the overlap of the field of views is as big as possible. The LEDs are flashing with a pulse width of 500 µs. The aperture of the camera lenses is set to 2.0, which provides a sufficient depth of field and allows for low integration times of 400 µs for the top camera and 500 µs for the bottom cameras. A low integration time is favorable to avoid motion blur.

For the LIF setup, a frequency of 800 Hz with an image size of 1920×215 pixels was found to ensure that the movement of the water surface can be tracked and the fluorescence profile stays in the field of view at wavy conditions. The pulse width of the laser is set to 30 µs. An aperture setting of 8.0 is used for the camera lens. The integration time is set to the minimum value of 34 µs, but is effectively given by the time period of 30 µs during which the laser is on.

The integration times for both setups were adjusted at a high fluorescence intensity of the resting water bulk at pH $\simeq$ 9 such that a good signal to noise ratio without saturation could be achieved. Since no amplification was needed, the gain of the cameras is set to zero.

The delay between the two trigger signals is chosen such that two LIF pulses fit between two BLI pulses. Table 4.1 gives an overview of the camera settings. All cameras are read out with *Heurisko* worksheets.

5. Calibration

In this chapter, the calibration of the measurement setup is presented. First, measurement results of the dissociation constants of the used dyes are shown. The calibration of the spectroscopy setups is addressed, followed by the discussion of the leakage rate of the wind-wave tunnel and the correction of the flow rate of the mass flow controller used for the input of ammonia. Furthermore, the geometric calibration of the cameras and the preprocessing of the recorded images are presented. Finally, it is explained how the fluorescence intensity seen by the cameras is used to infer the concentration of the alkaline pyranine component by means of a simulation and a calibration measurement.

5.1 Dissociation constants of the dyes

As stated in [Wolfbeis et al., 1983], the dissociation constant of pyranine varies with the ion concentration. Besides, different values for the dissociation constant of tartrazine are found in literature [Perez-Urquiza and Beltran, 2001]. Since the values of these parameters are crucial for the developed method and it was not evident which values can be assumed, own measurements were performed at a low ion concentration to obtain reference values for the conducted experiments.

5.1.1 Pyranine

For the analysis of pyranine, the absorbance of a $[\mathrm{I}]_{\mathrm{tot}} = 10^{-4}\,\mathrm{M}$ pyranine solution in a cell with a length of $L = 1\,\mathrm{cm}$ was measured using a spectrophotometer (*UV-2700* by *Shimadzu*). The functioning principle of the device is explained in appendix A.1. Deionized water was used for the solution. After the addition of the dye, the conductivity was $\kappa \simeq 20\,\mu\mathrm{S/cm}$. HCl and NaOH were added to adjust the pH value in a range from pH $\simeq 2$ to pH $\simeq 12.5$. The data is shown in Fig. 5.1. The wavelengths $\lambda = 331\,\mathrm{nm}$ and $\lambda = 415\,\mathrm{nm}$, at which the absorbance is independent of the pH, are called isosbestic points. The pH-dependency of the absorbance reflects the concentration variation of IH and I^-, since the resulting absorbance A_{I} is additively composed of the absorbances A_{IH} and A_{I^-} of the two components

$$A_{\mathrm{I}}(\lambda) = \overbrace{\epsilon_{\mathrm{IH}}(\lambda)[\mathrm{IH}]L}^{A_{\mathrm{IH}}(\lambda)} + \overbrace{\epsilon_{\mathrm{I^-}}(\lambda)[\mathrm{I^-}]L}^{A_{\mathrm{I^-}}(\lambda)}. \tag{5.1}$$

For pH < 4 the acidic and for pH > 11 the alkaline form is dominant. From the most acidic spectrum, where $[\mathrm{IH}] \simeq [\mathrm{I}]_{\mathrm{tot}}$, and the most alkaline spectrum, where $[\mathrm{I^-}] \simeq [\mathrm{I}]_{\mathrm{tot}}$, the molar absorption coefficients $\epsilon_{\mathrm{IH}}(\lambda)$ and $\epsilon_{\mathrm{I^-}}(\lambda)$ are determined according to Eq. 2.72. The data is shown in Fig. 3.2 (a) and can be used as reference spectra to determine the concentrations of the two components in a solution.

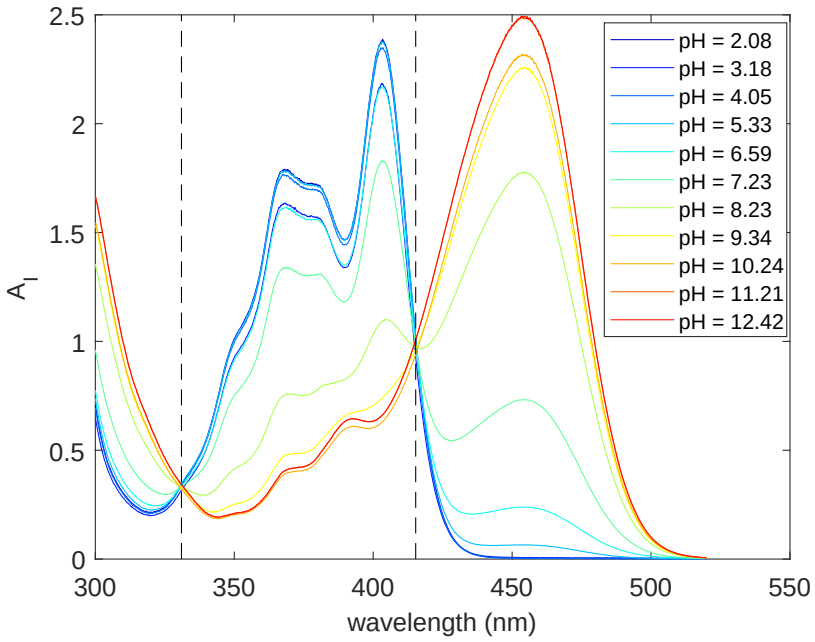

Fig. 5.1: Absorbance spectrum A_{I} of a 10^{-4} M pyranine solution in a cell with a length of 1 cm, measured with a spectrophotometer (see appendix A.1) for different pH values. The vertical dashed lines mark the isosbestic points of pyranine at $\lambda = 331$ nm and $\lambda = 415$ nm, where the absorbance is independent of the pH.

This was done for the data shown in Fig. 5.1, by fitting the reference spectra according to Eq. 5.1. The resulting concentration values are plotted versus the pH value in Fig. 5.2. With the identities

$$[\mathrm{I}]_{\mathrm{tot}} = [\mathrm{IH}] + [\mathrm{I^-}], \tag{5.2a}$$

$$10^{-\mathrm{pK_a(I)}} = \frac{10^{-\mathrm{pH}} \cdot [\mathrm{I^-}]}{[\mathrm{IH}]}, \tag{5.2b}$$

the concentration of both components can be written as a function of the pH with the parameters $[\mathrm{I}]_{\mathrm{tot}}$ and $\mathrm{pK_a(I)}$

$$[\mathrm{IH}] = \frac{[\mathrm{I}]_{\mathrm{tot}}}{10^{-\mathrm{pK_a(I)}+\mathrm{pH}}+1}, \tag{5.3a}$$

$$[\mathrm{I^-}] = \frac{[\mathrm{I}]_{\mathrm{tot}}}{10^{-\mathrm{pH}+\mathrm{pK_a(I)}}+1}. \tag{5.3b}$$

Thus, each of these equations can be fitted to the respective data to determine the dissociation constant of pyranine. To improve the fit performance, $[\mathrm{I}]_{\mathrm{tot}}$ remains a free parameter. The fitted curves are depicted in Fig. 5.2. The results for $\mathrm{pK_a(I)}$ of both fits are averaged, yielding

$$\mathrm{pK_a(I)} = 7.68 \pm 0.03, \tag{5.4}$$

where the difference of the two results i taken as an upper error estimate.

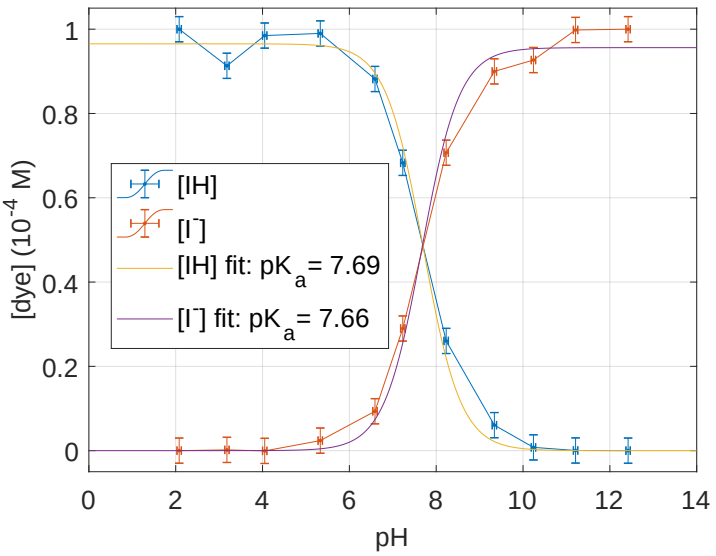

Fig. 5.2: Concentration of IH and $\mathrm{I^-}$, determined from the absorbance spectra in Fig. 5.1, as a function of the pH. The fitted curves yield the $\mathrm{pK_a}$ value of pyranine.

5.1.2 Tartrazine

Similar absorption measurements as for pyranine were performed with a $[\mathrm{T}]_{\mathrm{tot}} = 10^{-4}\,\mathrm{M}$ tartrazine solution. Equations 5.1, 5.2 and 5.3 apply analogously to tartrazine.

Using the spectrophotometer and a cell with a length of 1 cm, the molar absorption coefficients $\epsilon_{\mathrm{TH}}(\lambda)$ and $\epsilon_{\mathrm{T^-}}(\lambda)$ were determined with absorbance measurements at $\mathrm{pH} = 4$ and $\mathrm{pH} = 12$, respectively. The results are shown in Fig. 3.2 (b).

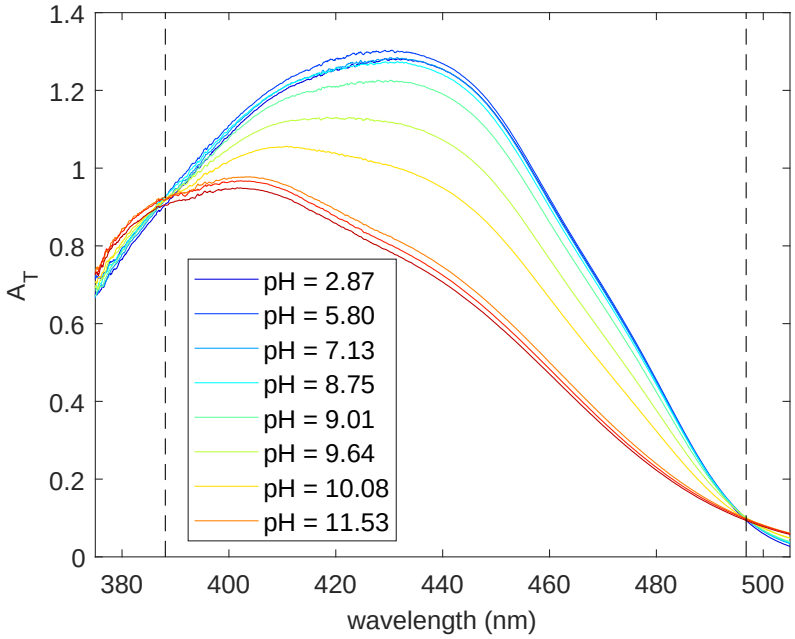

Fig. 5.3: Absorbance spectrum A_T of a 10^{-4} M tartrazine solution for various pH values. The spectra were measured with the transmission probe. The vertical dashed lines mark the isosbestic points of tartrazine at $\lambda = 388\,\text{nm}$ and $\lambda = 497\,\text{nm}$.

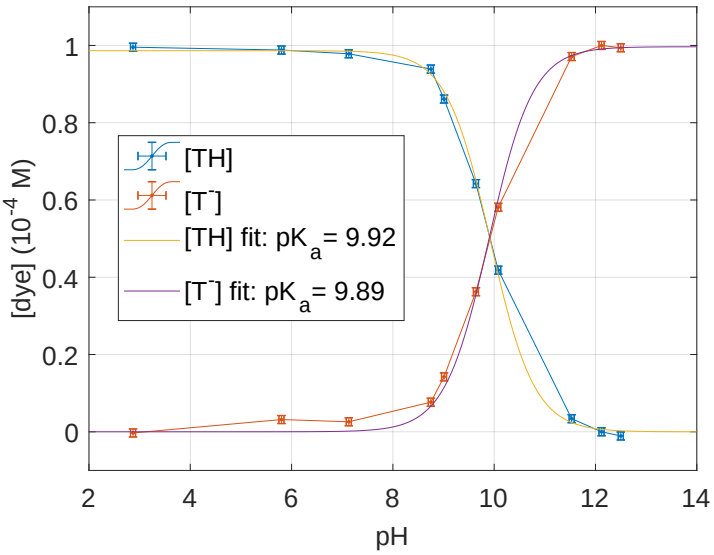

Fig. 5.4: Concentration of TH and T^-, determined from the absorbance spectra in Fig. 5.3, as a function of the pH. The shown fit curves yield the pK_a value of tartrazine.

In order to determine the dissociation constant $pK_a(T)$, the absorbance of the tartrazine solution was measured with the transmission probe (see Sec. 4.1.2) for different pH values (see Fig. 5.3). In analogy to the evaluation of the pyranine spectra, the concentration values and the dissociation constant are obtained

$$pK_a(T) = 9.91 \pm 0.03. \tag{5.5}$$

The concentration data versus the pH value and the adjusted curves are shown in Fig. 5.4.

5.2 Calibration of the spectroscopy setups

With the spectroscopy setups used in this study (see Sec. 4.1.2) the air-side bulk concentration of ammonia and the concentration of the dyes in the water bulk are measured. This is essential for the mass balance of the invasion experiments with ammonia. The absorbance spectra are determined according to Eq. 2.70b. Details on the determination of concentration values and the reference spectra are given in the following.

5.2.1 UV setup

Figure 5.5 (a) shows the molar absorption coefficient $\epsilon_{NH3}(\lambda)$ of ammonia in the wavelength range that corresponds to the one of the used UV light source. The spectrum is taken from [Cheng et al., 2006] and serves as a reference to determine absolute concentrations. Ammonia has distinct, narrow absorption characteristics.

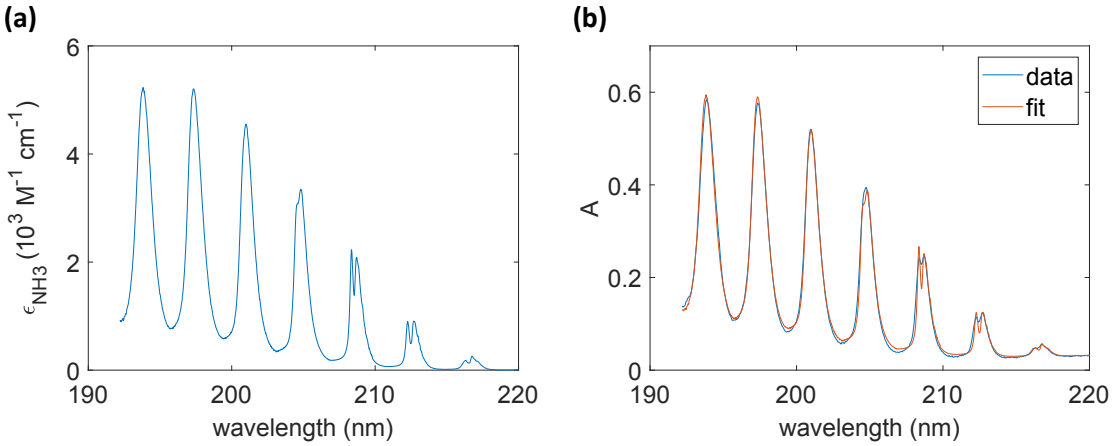

Fig. 5.5: (a) Molar absorption coefficient of gaseous ammonia ϵ_{NH3} in the wavelength range $\lambda = 192 - 224\,\text{nm}$ [Cheng et al., 2006]. (b) Example of a measured absorbance spectrum of ammonia. The shown fit according to Eq. 5.6 yields a concentration of $[NH_3]_a = 1.16 \cdot 10^{-6}\,\text{M}$.

To obtain the air-side concentration of ammonia $[NH_3]_a$, the function

$$A_{UV,fit}(\lambda) = \epsilon_{NH3}(\lambda) \cdot [NH_3]_a \cdot L + \sum_{n=0}^{2} p_n \lambda^n \tag{5.6}$$

is fitted to the measured absorbance spectra, where the absorption length of the used setup is $L = (93 \pm 0.5)\,\mathrm{cm}$. The polynomial term is added in order to account for changes of the lamp spectrum (cf. Eq. 2.75). Figure 5.5 (b) illustrates a measured spectrum with the best fit.

5.2.2 VIS setup

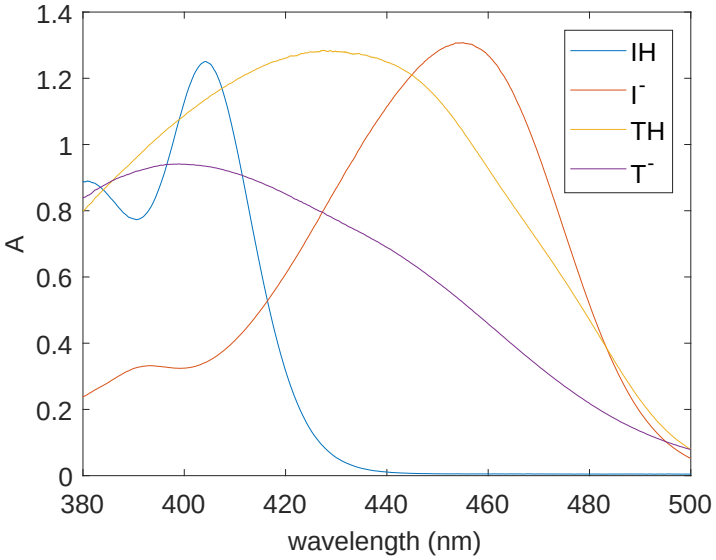

Fig. 5.6: Reference absorbance spectra of the acidic and the alkaline form of pyranine (IH, I^-) and tartrazine (TH, T^-). The spectra were measured with the transmission probe in solutions with $[I]_{tot} = 10^{-4}\,\mathrm{M}$ and $[T]_{tot} = 10^{-4}\,\mathrm{M}$, respectively.

For the water-side spectroscopy, a similar approach is used to determine the concentrations of the acidic and alkaline forms of pyranine and tartrazine. Reference absorbance spectra for the dye components, measured with the transmission probe, are needed. For tartrazine, the results shown in Sec. 5.1.2 are used. The spectra for pyranine are obtained in analogy. For consistency reasons, the reference spectra measured with the spectrophotometer (see Sec. 5.1.1) are not used.

Figure 5.6 shows the reference spectra measured with the transmission probe. Apart from IH, the dye components have rather broad absorption bands, which complicates their distinction by a fit. In order to obtain consistent fit results for the concentrations, the absorbance spectra are evaluated as follows.

The fit function

$$\begin{aligned} A_{TP,fit}(\lambda) = \{&A_{IH}(\lambda)[IH] + A_{I^-}(\lambda)[I^-] + \\ &A_{TH}(\lambda)[TH] + A_{T^-}(\lambda)[T^-]\} + p_0, \end{aligned} \tag{5.7}$$

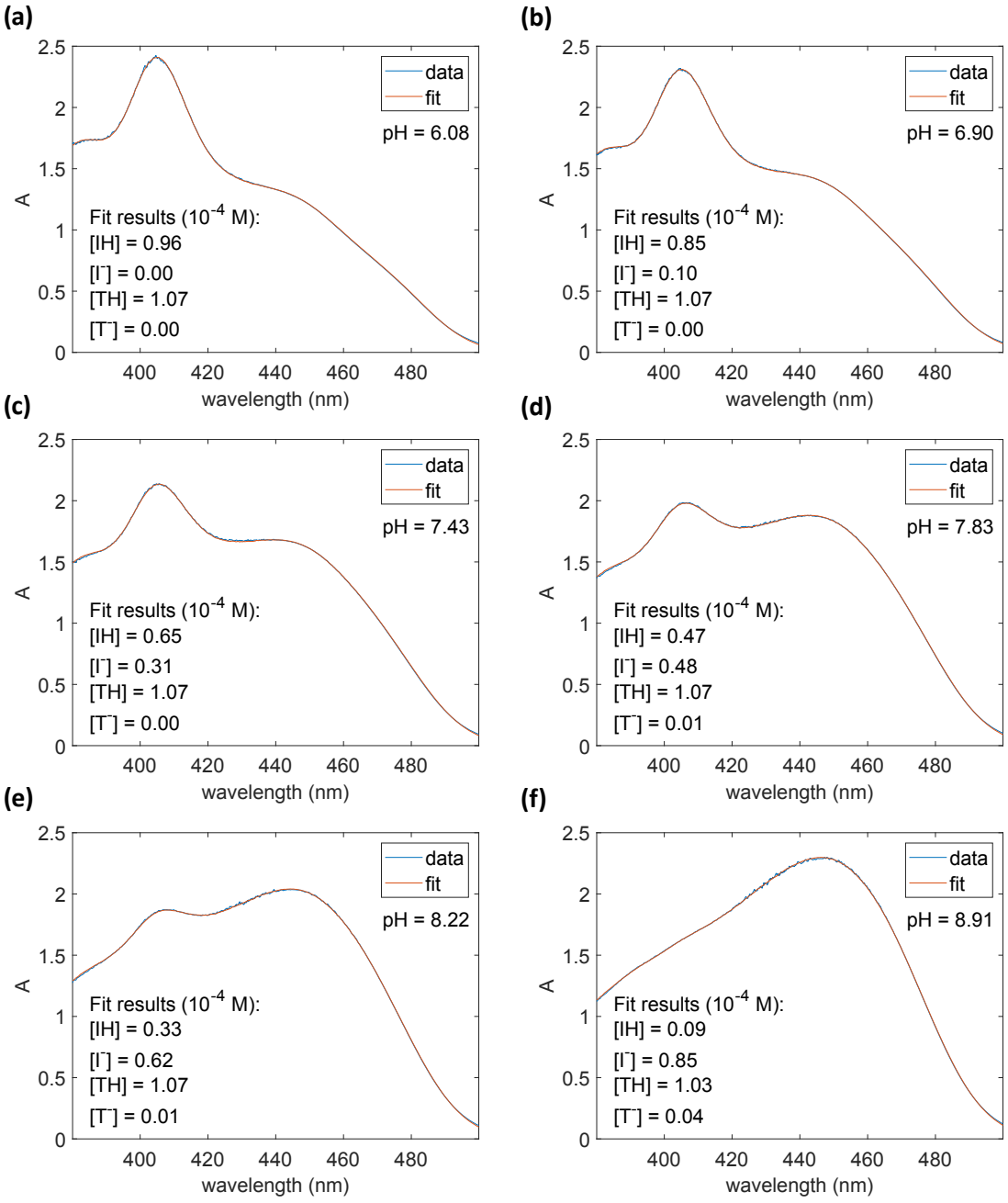

Fig. 5.7: Compilation of absorbance spectra of a solution with $[\mathrm{I}]_{\mathrm{tot}} = 0.97 \cdot 10^{-4}\,\mathrm{M}$ and $[\mathrm{T}]_{\mathrm{tot}} = 1.08 \cdot 10^{-4}\,\mathrm{M}$, measured with the transmission probe. The pH value increases from (a) to (f). The fit results are obtained according to the Eq. 5.7.

is adjusted to the data, where $A_{\mathrm{IH}}(\lambda)$, $A_{\mathrm{I}^-}(\lambda)$, $A_{\mathrm{TH}}(\lambda)$ and $A_{\mathrm{T}^-}(\lambda)$ are the reference spectra and p_0 denotes a free offset. The concentrations of the dyes are obtained in units of 10^{-4} M. For the fit according to Eq. 5.7, the following constraints are set:

$$0 \leq [\mathrm{IH}],\, [\mathrm{I}^-] \leq [\mathrm{I}]_{\mathrm{tot}}, \tag{5.8a}$$

$$0 \leq [\mathrm{TH}],\, [\mathrm{T}^-] \leq [\mathrm{T}]_{\mathrm{tot}}. \tag{5.8b}$$

Since $[\mathrm{IH}] = [\mathrm{I}]_{\mathrm{tot}}$ and $[\mathrm{TH}] = [\mathrm{T}]_{\mathrm{tot}}$ hold in the acidic regime, the total dye concentrations are determined by recording spectra at pH ≈ 4 to which only the spectra $A_{\mathrm{IH}}(\lambda)$ and $A_{\mathrm{TH}}(\lambda)$ are fitted. The stricter constraints $[\mathrm{IH}] + [\mathrm{I}^-] = [\mathrm{I}]_{\mathrm{tot}}$ and $[\mathrm{TH}]+[\mathrm{T}^-] = [\mathrm{T}]_{\mathrm{tot}}$ are found to lead to distorted fit results. If the fit yields $[\mathrm{IH}] > [\mathrm{I}^-]$ (i.e. the solution is rather acidic), the fit is repeated with $[\mathrm{T}^-] = 0$. This can be assumed because of the significantly higher dissociation constant of tartrazine. The systematic uncertainty of the concentration values obtained from the fit is estimated to be $1\,\% \cdot 10^{-4}$ M.

Figure 5.7 shows absorbance spectra of a solution with $[\mathrm{I}]_{\mathrm{tot}} = 0.97 \cdot 10^{-4}$ M and $[\mathrm{T}]_{\mathrm{tot}} = 1.08 \cdot 10^{-4}$ M for different pH values with fit results.

5.3 Leakage rate

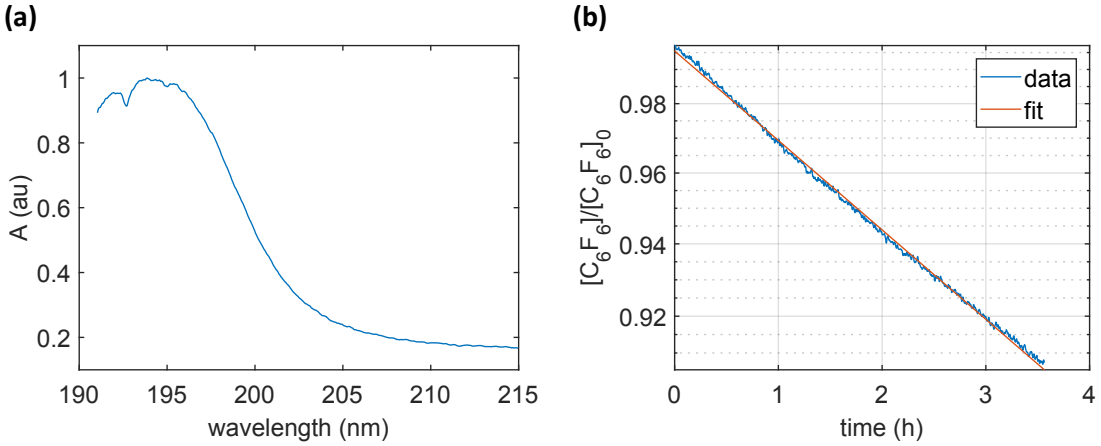

Fig. 5.8: (a) Normalized absorbance of C_6F_6 in the UV wavelength range, measured with the UV spectroscopy setup. (b) Concentration of C_6F_6 over time in units of its initial concentration with a logarithmic y-axis.

The leakage rate of the Heidelberg linear wind-wave tunnel was measured using the gas hexafluorobenzene (C_6F_6) with a low solubility of $\alpha(C_6F_6) = 1.36$ [Sander, 2015] and absorption features in the UV wavelength range [Motch et al., 2006]. Thus, the

UV spectroscopy setup could be used to measure its concentration over time. The tunnel was closed, drained and dried so that changes of the gas concentration could only be caused by leaks. As shown in Sec. 3.4, an exponential decay of the concentration according to

$$[C_6F_6](t) = [C_6F_6]_0 \cdot \exp(-\lambda_{\text{leak}} t) \tag{5.9}$$

is expected. The leakage rate of a tunnel typically increases with the wind speed. Therefore, the wind frequency was set to the maximum usable value of 25 Hz to obtain an upper limit for the leakage rate. About 250 ml of hexafluorobenzene were injected with a syringe through a small opening, which was immediately sealed afterwards. From then on absorbance spectra were acquired. Figure 5.8 (a) shows an example. After the air space had become well mixed, the maximum concentration $[C_6F_6]_0$ was reached. Since only relative changes of the concentration are needed to infer the leakage rate, the spectrum recorded at this point was defined as the reference A_0. With this, the concentration $[C_6F_6]$ in units of $[C_6F_6]_0$ is determined with the fit function

$$A_{\text{UV,fit}}(\lambda) = A_0 \cdot [C_6F_6] + \sum_{n=0}^{2} p_n \lambda^n, \tag{5.10}$$

similar to Eq. 5.6. Fitting Eq. 5.9 to the resulting concentration data (see Fig. 5.8 (b)), yields

$$\lambda_{\text{leak}} = (2.66 \pm 0.02) \cdot 10^{-2}\,\text{h}^{-1}. \tag{5.11}$$

Since the typical decay rate of the air-side ammonia concentration due to gas trasnfer into water is on the order of $3\,\text{h}^{-1}$ [Kräuter, 2015], the leakage rate can be neglected for the measurements conducted in this thesis.

5.4 Correction of the mass flow controller input

For a correct mass balance, a reliable input rate of ammonia is needed. By measuring the air-side ammonia concentration with the UV spectroscopy setup, it was found that for set flow rates $F_{\text{set}} \leq 10\,\text{ml/min}$, the real flow rate of the used mass flow controller is systematically higher than the set value. To obtain a corrected flow rate F_{corr} for this range, systematic measurements were performed.

For this, the wind-wave tunnel was closed, drained and dried. The frequency of the wind engine was set to 15 Hz to allow for a homogeneous mixing of the input ammonia. The air humidity was about $\sim 30\,\%$. Different flow rates in the range between 0.1 ml/min and 30 ml/min were set for one minute. From the maximum concentration $[NH_3]_a$ that was measured after each injection with the spectroscopy setup, a flow rate was calculated according to

$$F_{\text{UV}} = [NH_3]_a \cdot V_a \cdot V_M / t, \tag{5.12}$$

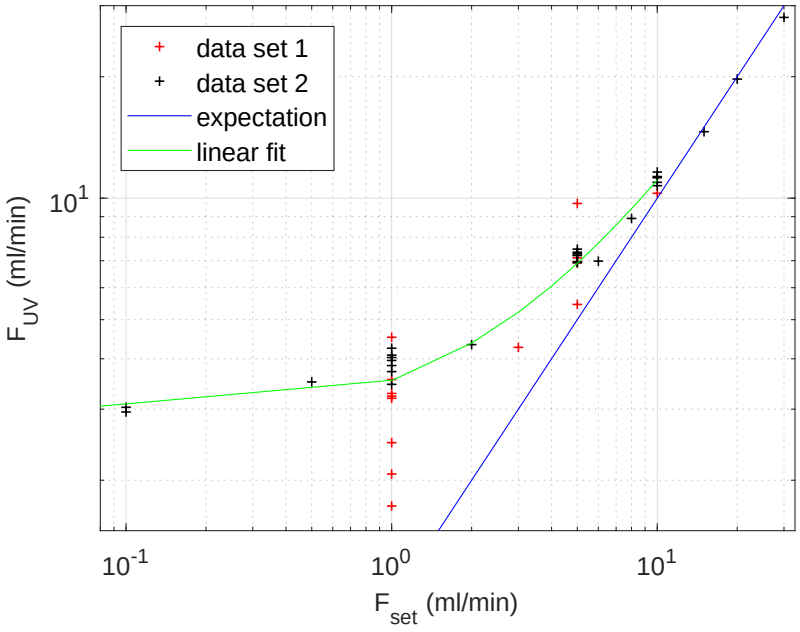

Fig. 5.9: Comparison of the ammonia flow rate F_{set} set at the mass flow controller and the rate F_{UV} calculated from data measured with the UV spectroscopy setup. Logarithmic scales are chosen and errorbars are omitted for illustrative purposes. The data were obtained in two independent measurement series. The blue line indicates the expected flow rate. A line is fitted to the data points with $F_{\text{set}} \leq 10\,\text{ml/min}$ to obtain parameters used to calculate a corrected flow rate.

with the air volume $V_{\text{a}} = (3.0 \pm 0.2)\,\text{m}^3$ of the tunnel, the molar volume $V_{\text{M}} \simeq 24\,\text{M}^{-1}$ at 25 °C and the input time $t = (60 \pm 2)\,\text{s}$.

In Fig. 5.9, the set and the measured flow rate are compared. The measured flow rate is in agreement with the set one for $F_{\text{set}} > 10\,\text{ml/min}$. Deviations which cannot be explained by the uncertainty given by the manufacturer (see Eq. 4.5) occur for $F_{\text{set}} \leq 10\,\text{ml/min}$. A linear function

$$F_{\text{corr}} = a \cdot F_{\text{set}} + b. \tag{5.13}$$

is applied to these data points as shown in Fig. 5.9. The resulting fit parameters $a = 0.78 \pm 0.06$ and $b = (2.7 \pm 0.2)\,\text{ml/min}$ are used to determine a corrected flow rate F_{corr} for this range.

5.5 Geometric calibration of the cameras

To quantify the magnification and the spatial resolution of the cameras, a target with a 2 mm × 2 mm grid of crosses was used. The cameras of the BLI setup (see Sec. 4.2.2) and the profile camera of the LIF setup (see Sec. 4.2.3) are addressed in turn in the following.

5.5.1 BLI cameras

The cross target was attached to a translation stage with which displacements in a range of 0 mm – 25 mm could be adjusted. The translation stage was mounted to a frame such that the zero setting of the translation stage corresponded to a water level of 8 cm. The wind-wave tunnel was filled with water up to the standard water level $z_{\mathrm{ws},0} = 9.2\,\mathrm{cm}$ at first. As the fluorescence in the mass boundary layer occurs close to the water surface, the bottom and the top BLI cameras were focused on the target placed at that height. Figure 5.10 shows as an example image recorded by the top camera B4.

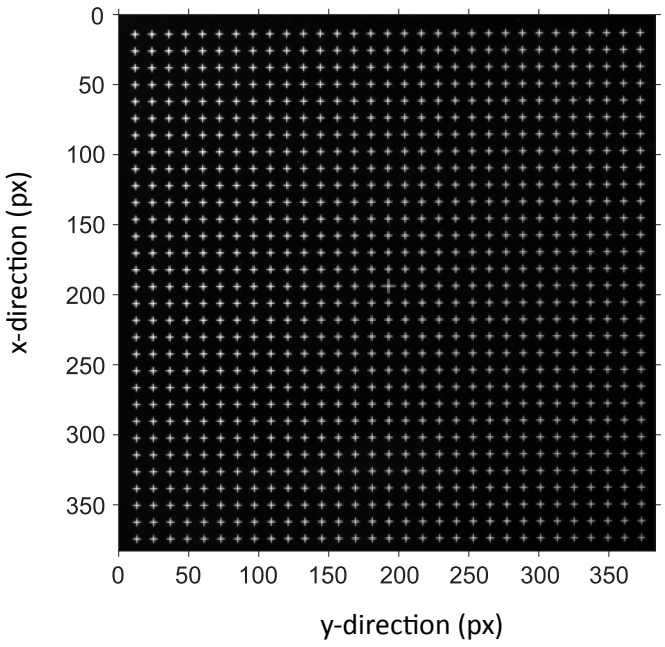

Fig. 5.10: Exemplary calibration image recorded by the top camera B4 at a target height of $z_{\mathrm{ws},0}$ corresponding to the standard water level at rest.

After that, a calibration measurement was performed to determine the depth resolution of the stereo pairs formed by the bottom cameras. The water level and the target height were equally adjusted between 8 cm and 10.5 cm in steps of 1 mm and images of the target were recorded. The water level was needed to be adjusted to account for refraction by the water, as in the experiments the bottom cameras also look

through the water column. The chosen range of water levels covers the amplitudes of the water waves $\eta_{\max} \simeq 1\,\mathrm{cm}$ that occur at the maximum usable wind frequency (25 Hz). For the sake of completeness, images were analogously recorded with the top camera for the different target heights and water levels. In order to match the top camera with the bottom cameras, images of glass beads placed on the water surface were acquired at each of the water levels used for the recordings of the cross target. The used glass beads had a diameter of about 1 mm. The determination of the magnification factors of all BLI cameras for the different target heights and the depth resolution of the stereo pairs formed by the bottom cameras is shown in the following.

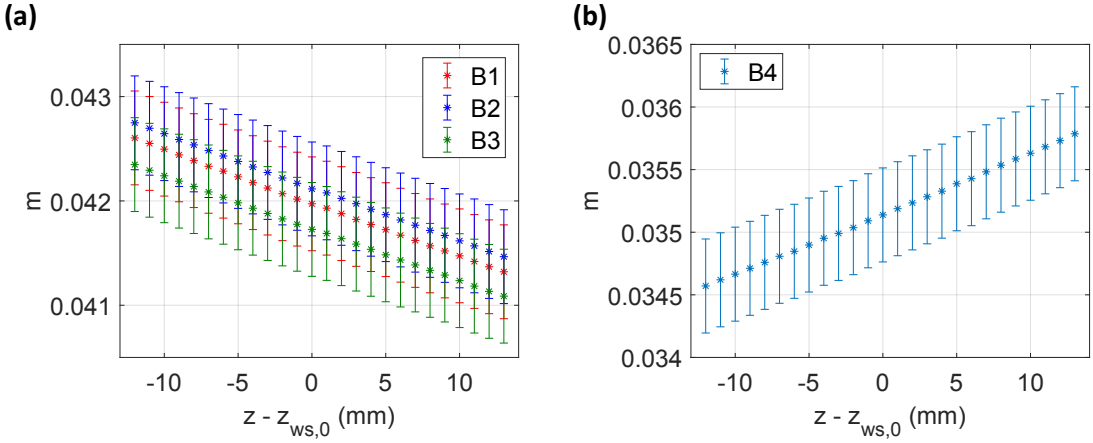

Fig. 5.11: Magnification factor m of the bottom cameras B1, B2, B3 in (a) and the top camera B4 in (b) as a function of the target height z, where $z = z_{\mathrm{ws},0}$ corresponds to the standard water level of 9.2 cm.

The positions of the grid crosses in the recorded images are identified with an image processing algorithm, which only needs the number of crosses per dimension. With the mean and the standard deviation of the distances between neighboring crosses in pixels, the magnification factor and its uncertainty are determined by using the pixel size of the camera sensor and the real world distance between the crosses. The standard deviation is used as an error estimate. The results are shown in Fig. 5.11. The magnification of the BLI cameras and the corresponding spatial resolution at the target height $z_{\mathrm{ws},0} = 9.2\,\mathrm{cm}$ are given in Tab. 5.1.

The condition that the focal lengths of the lenses of two stereo cameras has to be the same (see Sec. 4.2.2) is equivalent to the fact that both cameras have the same magnification factor. As the magnification factors of the bottom cameras are in agreement with each other in the scope of their uncertainties, the pairs (B1,B2), (B2,B3) and (B1,B3) can be used for stereo vision.

The depth resolution of the stereo pairs is obtained based on Eq. 4.7. The parallax

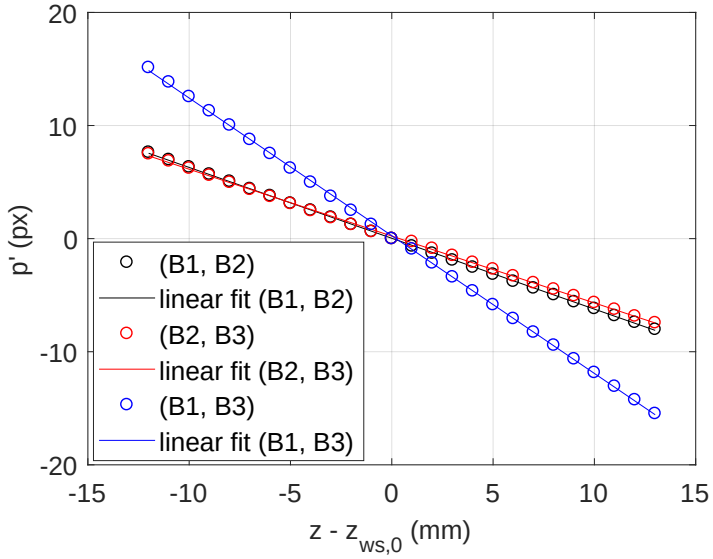

Fig. 5.12: Parallax p' of the stereo pairs (B1, B2), (B2, B3) and (B1, B3) as a function of the target height z, where $z_{\mathrm{ws},0}$ corresponds to the standard water level of 9.2 cm. The linear fits yield the depth resolution in px/mm.

p' of each pair is determined as the average horizontal distance between the cross positions viewed by the two cameras. As only the change of $p'(z)$ with changing depth z is of interest, the parallax at the level of the resting water surface $z_{\mathrm{ws},0}$ is used as a reference such that $p'(z_{\mathrm{ws},0}) = 0$. This corresponds to a matching of the cross positions obtained at this depth. Figure 5.12 shows the parallax of the stereo pairs with respect to the reference. The depth resolution $r = \frac{\partial p'}{\partial z}$ is then determined as the slope of a line fitted to the data $p'(z)$ as shown in the figure. The results for the three stereo pairs given as absolute values are

$$|r_{1,2}| = 0.63\,\mathrm{px/mm}, \tag{5.14a}$$
$$|r_{2,3}| = 0.59\,\mathrm{px/mm}, \tag{5.14b}$$
$$|r_{1,3}| = 1.22\,\mathrm{px/mm}. \tag{5.14c}$$

To correct the images for the electrical dark current of the cameras and the inhomogeneity of the used illumination, a dark and a flat field image were recorded. For the dark correction, 1000 images were recorded without lighting and averaged, yielding a dark image for each camera. For the flat field correction, 1000 images of the water illuminated by the LEDs were recorded, where the dyes were present in the concentrations $[\mathrm{I}]_{\mathrm{tot}} \simeq 10^{-4}\,\mathrm{M}$ and $[\mathrm{T}]_{\mathrm{tot}} \simeq 10^{-4}\,\mathrm{M}$ and the pH value was pH = 9. Thus, a high fluorescence intensity was imaged. The recorded images were averaged and normalized, yielding a flat field image for each camera.

The image sections of all recorded BLI images were reduced to the water patch illuminated at the center of the tunnel to exclude shadows at the edges. Their sizes are listed in Tab. 5.1. Figure 5.13 (a) shows the flat field recording of the bottom

camera B2 with the reduced image section. The field of views of the BLI cameras on the water surface at the standard water level $z_{\mathrm{ws},0} = 9.2\,\mathrm{cm}$ are shown in 5.13 (b). The common area of the observed water patch was about $13.0 \times 6.6\,\mathrm{cm}^2$.

To obtain a calibrated BLI image $G_{\mathrm{cal}}(x, y)$, a recorded raw image is preprocessed using the recorded dark and flat field images. First, the inverted LUT transformation is applied to the dark, flat field and raw images. After this transformation the gray scale values take values between zero and one (cf. Sec. 4.2.4). With the resulting dark $D(x, y)$, flat field $L(x, y)$ and raw image $G_{\mathrm{raw}}(x, y)$, the calibrated image is obtained from

$$G_{\mathrm{cal}}(x, y) = \frac{G_{\mathrm{raw}}(x, y) - D(x, y)}{L(x, y) - D(x, y)}. \tag{5.15}$$

The value of a pixel in this calibrated image is assumed as the depth-integrated fluorescence signal $\hat{I}_{\mathrm{F}}$ in units of the normalized gray scale values g_{norm}.

camera	size of image section (px)	$m\,(10^{-2})$	$s\,(\mu\mathrm{m/px})$
B1	1000×470	4.20 ± 0.05	140 ± 1
B2	1127×470	4.21 ± 0.05	139 ± 1
B3	936×470	4.17 ± 0.05	141 ± 1
B4	921×470	3.51 ± 0.04	167 ± 2

Table 5.1: Size of the used image section as well as the magnification factor m and the spatial resolution s at the standard water level $z_{\mathrm{ws},0} = 9.2\,\mathrm{cm}$ of the BLI cameras (B1, B2, B3, B4).

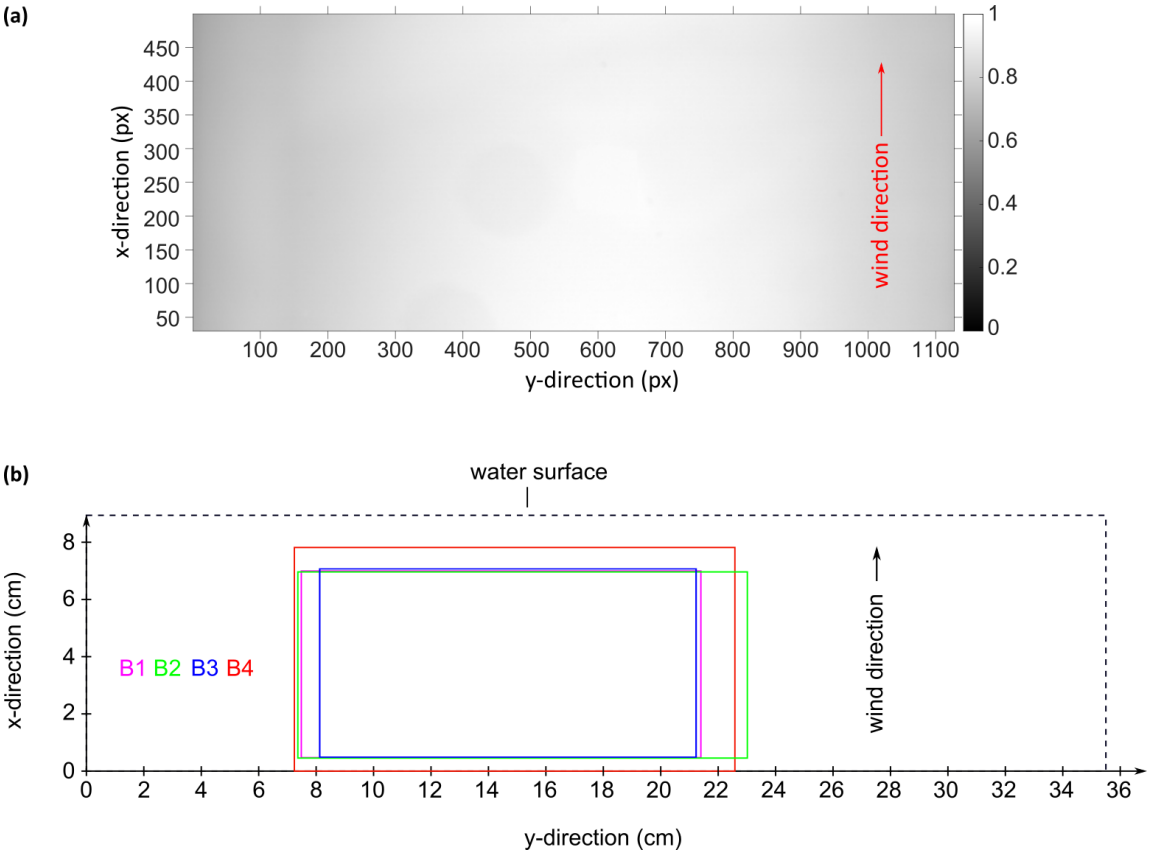

Fig. 5.13: (a) Normalized flat field image recorded by the bottom camera B2 showing the fluorescence signal of pyranine at pH = 9. The shown image section is reduced to the water patch illuminated at the center of the tunnel. The wind direction coincides with the x-direction. (b) Illustration of the field of views of the BLI cameras (B1, B2, B3, B4) on the water surface at the standard water level $z_{\mathrm{ws},0} = 9.2\,\mathrm{cm}$ viewed from above.

5.5.2 LIF camera

To focus the profile camera of the LIF setup, the tunnel was filled with water and the cross target was directly placed in the vertical fluorescence profile. To account for displacements of the water surface when waves are present, the water level was raised such that the water surface was outside of the field of view. Figure 5.14 (a) shows the recorded calibration image. The position and the focus of the camera lens were adjusted such that a magnification factor of

$$m_{\mathrm{P}} = 1.01 \pm 0.01 \tag{5.16}$$

was achieved and the best image sharpness was at the standard water level.

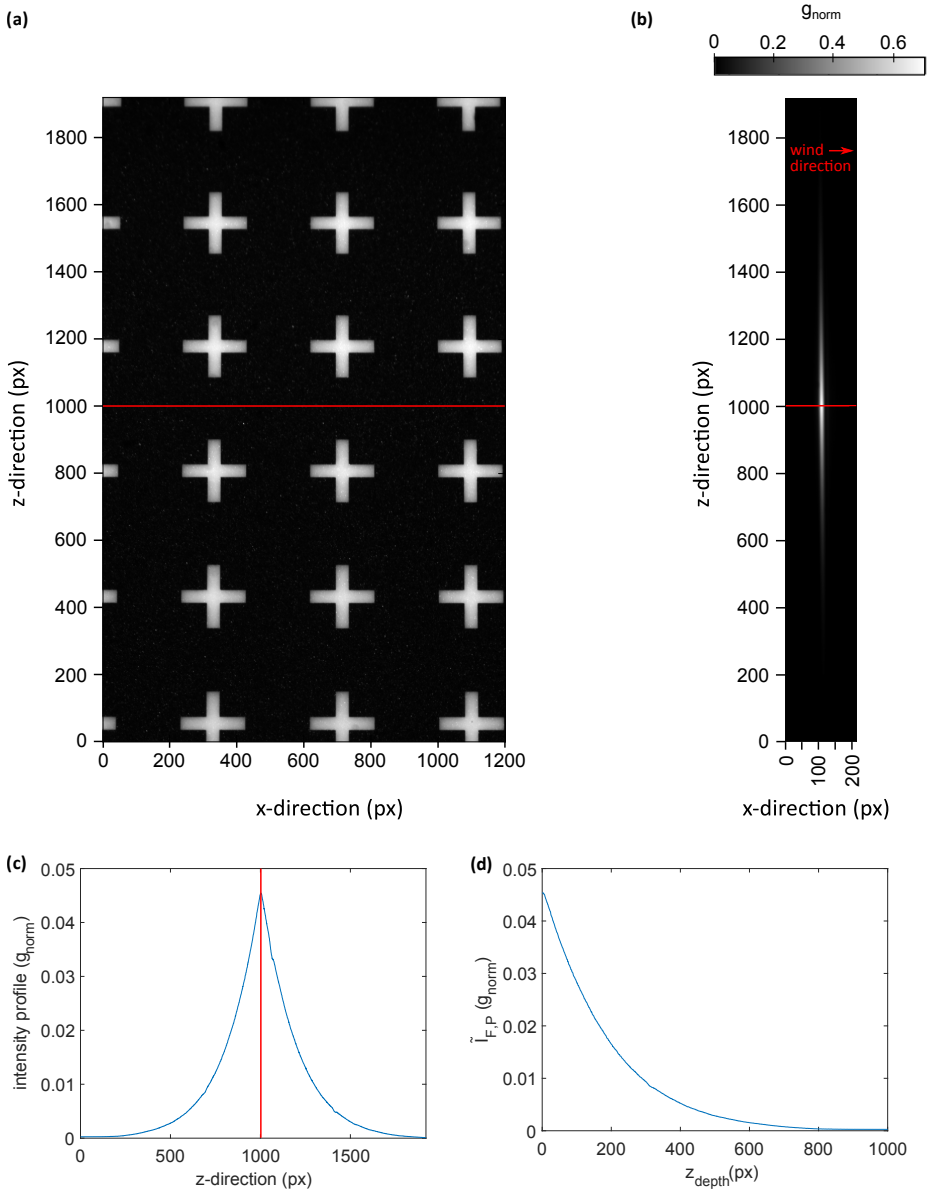

Fig. 5.14: (a) Calibration image of the profile camera, where the target was placed in the vertical fluorescence profile and the tunnel was filled with water. The red line indicates the standard water level $z_{\mathrm{ws},0} = 9.2\,\mathrm{cm}$ and the water depth increases from top to bottom. In this image, the water surface was outside of the field of view. (b) Example image of the fluorescence profile where the dyes were in the water ($[\mathrm{I}]_{\mathrm{tot}} \simeq [\mathrm{T}]_{\mathrm{tot}} \simeq 10^{-4}\,\mathrm{M}$) and the tunnel was filled up to the standard water level (red line). The wind direction is indicated by the red arrow. The gray values are given in units of the normalized scale g_{norm}. (c) Mean of the lines of the image in (b). The part of the resulting intensity profile from the largest depth to the water surface, that is marked by the red line, is the fluorescence profile $\tilde{I}_{\mathrm{F,P}}$ shown in (d). The new pixel coordinate z_{depth} increases with depth, where $z_{\mathrm{depth}} = 0$ at the current water surface position.

Thus, a high spatial resolution of $s_\mathrm{P} = (5.80 \pm 0.06)\,\mu\mathrm{m/px}$ was achieved. The magnification factor was determined from the calibration image in analogy to the BLI cameras.

Similar to the BLI cameras, a dark image was acquired for the profile camera. For preprocessing, the inverted LUT transformation is applied to the dark and the raw images. The dark image is then subtracted from the raw data.

Figure 5.14 (b) shows a preprocessed image of the fluorescence profile recorded with the profile camera. The intensity is given by the normalized gray scale values g_norm. The water surface that was at the standard water level $z_\mathrm{ws,0} = 9.2\,\mathrm{cm}$ is marked by the red line, where the maximum intensity is located. The part of the image below the red line shows the real water-side fluorescence profile, while the part above corresponds to its mirror image created by total reflection at the water surface. The water depth increases downwards from the red line. The reduction of the intensity with depth is a consequence of the absorption by the dyes that were in the water in the concentration also used for the experiments ($[\mathrm{I}]_\mathrm{tot} \simeq [\mathrm{T}]_\mathrm{tot} \simeq 10^{-4}\,\mathrm{M}$). The gray values in each line at a z-position in the image are averaged to obtain a mean intensity profile as shown in Fig. 5.20 (c). During the experiments at wavy conditions, this method to obtain a profile was found to yield more reliable results than the determination of the maximum value in each line. The profile from the largest depth to the water surface corresponds to the fluorescence profile $\tilde{I}_\mathrm{F,P}$ (see Fig. 5.20 (d)). The new pixel coordinate z_depth increases with depth, where $z_\mathrm{depth} = 0$ corresponds to the current position of the water surface.

5.6 Calibration of the fluorescence intensity

The following section addresses the calibration based on a numerical simulation that relates the concentration of the alkaline form of pyranine $[\mathrm{I}^-]$ to its fluorescence intensity measured with the cameras. First, the simulation is explained, where the notation of the fluorescence signals introduced in Sec. 2.4 is used. After that, the calibration measurement is related to the simulation results to obtain calibration parameters.

5.6.1 Simulation of the fluorescence intensity

A solution containing pyranine and tartrazine is considered. For the BLI setup, the fluorescence intensity $\hat{I}_\mathrm{F}(L)$ integrated along the water column L is needed. For the LIF setup, the fluorescence profile $\tilde{I}_\mathrm{F}(z)$ is required (cf. Fig. 4.6). To simplify notation, the concentrations and the (decadic) absorption coefficients of the acidic

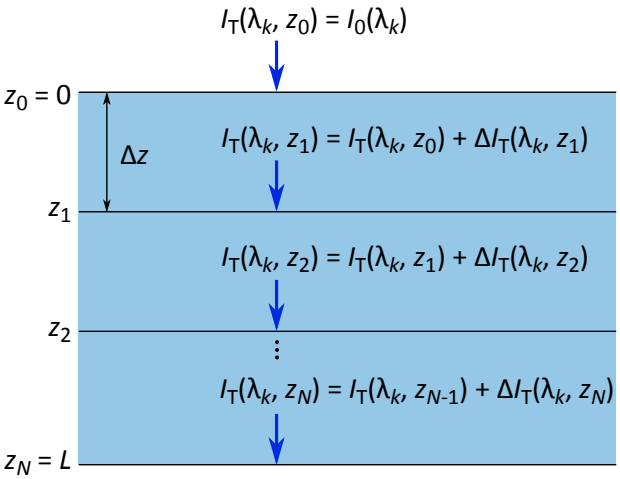

Fig. 5.15: Scheme illustrating the simulation used to recursively calculate the light intensity $I_\mathrm{T}(\lambda_k, z_n)$ that is transmitted by an absorbing solution. The total absorption length L is divided into a grid with grid spacing Δz. The initial intensity $I_0(\lambda_k)$ is reduced in each layer by absorption expressed by the term $\Delta I_\mathrm{T}(\lambda_k, z_n)$.

and alkaline form of pyranine ($i = 1, 2$) and tartrazine ($i = 3, 4$) are denoted by c_i and ϵ_i in the context of the simulation. With this, Eq. 2.73 reads

$$\mathrm{d}I_\mathrm{T}(\lambda) = -I_0(\lambda) \sum_{i=1}^{4} \ln(10)\epsilon_i(\lambda)c_i(z)\mathrm{d}z. \tag{5.17}$$

In Eq. 2.79, the fluorescence intensity could be related to the absorbed light and hence to the concentration of the fluorophore because only the fluorescent species was present. Since tartrazine also absorbs the excitation light, the fluorescence intensity $\hat{I}_\mathrm{F}(L)$ cannot be obtained analytically. Therefore a simulation is performed which discretely calculates the intensity of the transmitted light $I_\mathrm{T}(\lambda, z)$ and the fluorescence profile $\tilde{I}_\mathrm{F}(z)$. Integration of $\tilde{I}_\mathrm{F}(z)$ along the water column yields $\hat{I}_\mathrm{F}(L)$. Moreover, the profile of the total transmitted intensity $\tilde{I}_\mathrm{T}(z)$ is useful to estimate the penetration depth of light emitted by a (broadband) light source.

The simulation is explained in the following. The depth z and the wavelength λ are described by discrete variables z_n and λ_k. All integrals are performed as sums. As shown in Fig. 5.15, the total absorption length is divided into a grid with $N + 1$ equidistant grid points z_n and a grid spacing Δz, where the water surface and the end of the water column are defined by $z_0 = 0$ and $z_N = L$, respectively. Within a layer $z_n < z \leq z_{n+1}$ between two neighboring points, the concentrations $c_i(z_{n+1})$ are assumed to be constant. At z_0, where the concentrations are $c_i(z_0) = 0$, light with the spectrum $I_0(\lambda_k)$ is irradiated. The integral of this spectrum over all wavelengths

$$I_{0,\mathrm{norm}} = \sum_k I_0(\lambda_k)\Delta\lambda_k \tag{5.18}$$

serves as a reference intensity.

The input parameters of the simulation are L, Δz, $I_0(\lambda_k)$, the absorption coefficients $\epsilon_i(\lambda_k)$, the quantum yield of pyranine Φ_F and the concentration profiles $c_i(z_n)$.

With them, the spectrum of transmitted light $I_\mathrm{T}(\lambda_k, z_n)$ and the profiles of the total transmitted intensity $\tilde{I}_\mathrm{T}(z_n)$ and the fluorescence intensity $\tilde{I}_\mathrm{F}(z_n)$ can be calculated recursively, layer by layer. In accordance with Eq. 5.17, the reduction of transmitted light $\Delta I_\mathrm{T}(\lambda_k, z_{n+1})$ in each layer $z_n \leq z \leq z_{n+1}$ is given by

$$\Delta I_\mathrm{T}(\lambda_k, z_{n+1}) = -I_\mathrm{T}(\lambda_k, z_n) \sum_{i=1}^{4} \ln(10)\epsilon_i(\lambda_k)c_i(z_{n+1})\Delta z. \tag{5.19}$$

Using the start values $I_\mathrm{T}(\lambda_k, z_0) = I_0(\lambda_k)$, $\tilde{I}_\mathrm{T}(z_0) = I_{0,\mathrm{norm}}$, $\tilde{I}_\mathrm{F}(z_0) = 0$, the recursion for $n = 0, ..., N-1$ is written as

$$I_\mathrm{T}(\lambda_k, z_{n+1}) = I_\mathrm{T}(\lambda_k, z_n) + \Delta I_\mathrm{T}(\lambda_k, z_{n+1}), \tag{5.20a}$$

$$\tilde{I}_\mathrm{T}(z_{n+1}) = \sum_k I_\mathrm{T}(\lambda_k, z_{n+1})\Delta\lambda_k, \tag{5.20b}$$

$$\tilde{I}_\mathrm{F}(z_{n+1}) = \Phi_\mathrm{F} \sum_k \left(I_\mathrm{T}(\lambda_k, z_n) \sum_{i=1}^{2} \ln(10)\epsilon_i(\lambda_k)c_i(z_{n+1})\Delta z \right) \Delta\lambda_k. \tag{5.20c}$$

As expressed by the last equation, only light absorbed by pyranine is converted to fluorescence. The depth-integrated fluorescence intensity is obtained from

$$\hat{I}_\mathrm{F}(L) = \sum_{n=0}^{N} \tilde{I}_\mathrm{F}(z_n)\Delta z. \tag{5.21}$$

For the length of the water column L, the standard water height 9.2 cm is employed. Since the maximum surface displacements at the used wind speed are on the order of a few millimeters, this is a useful approximation. Because of the moderate wind speed, also the slope of the water surface and hence optical aberrations like lens effects due to waves are expected to be rather small. A sufficiently fine spacing of $\Delta z = 1\,\mu\mathrm{m} \ll L$ is chosen. For the BLI setup, the measured LED spectrum with the blue filter (see Fig. 4.7) is used for $I_0(\lambda)$, while for the laser of the LIF setup only its central emission wavelength (see Sec. 4.2.3) is assumed in a good approximation. For the absorption coefficients, the measured spectra of the dye components are used (see Fig. 3.2). The quantum yield is assumed to be $\Phi_\mathrm{F} = 1$ (see Sec. 3.2.1). The concentration profiles $c_i(z_n)$ remain as free input parameters. With a fixed geometric arrangement of the lighting and the cameras and a constant intensity of the light sources, the fluorescence signals measured by the BLI cameras ($\mathrm{BLI} = \{\mathrm{B1}, \mathrm{B2}, \mathrm{B3}, \mathrm{B4}\}$) and the profile camera (P) are proportional to the simulated intensities

$$\hat{I}_\mathrm{F,BLI} = \sigma_\mathrm{BLI}\hat{I}_\mathrm{F}, \tag{5.22a}$$

$$\tilde{I}_\mathrm{F,P}(z) = \sigma_\mathrm{P}\tilde{I}_\mathrm{F}(z). \tag{5.22b}$$

with individual proportionality factors σ_{B1}, σ_{B2}, σ_{B3}, σ_{B4}, σ_P. Since the absorption length L is fixed, the explicit dependency of $\hat{I}_F$ on L is omitted for convenience. The calibration measurement presented in the next section aims to find these proportionality factors.

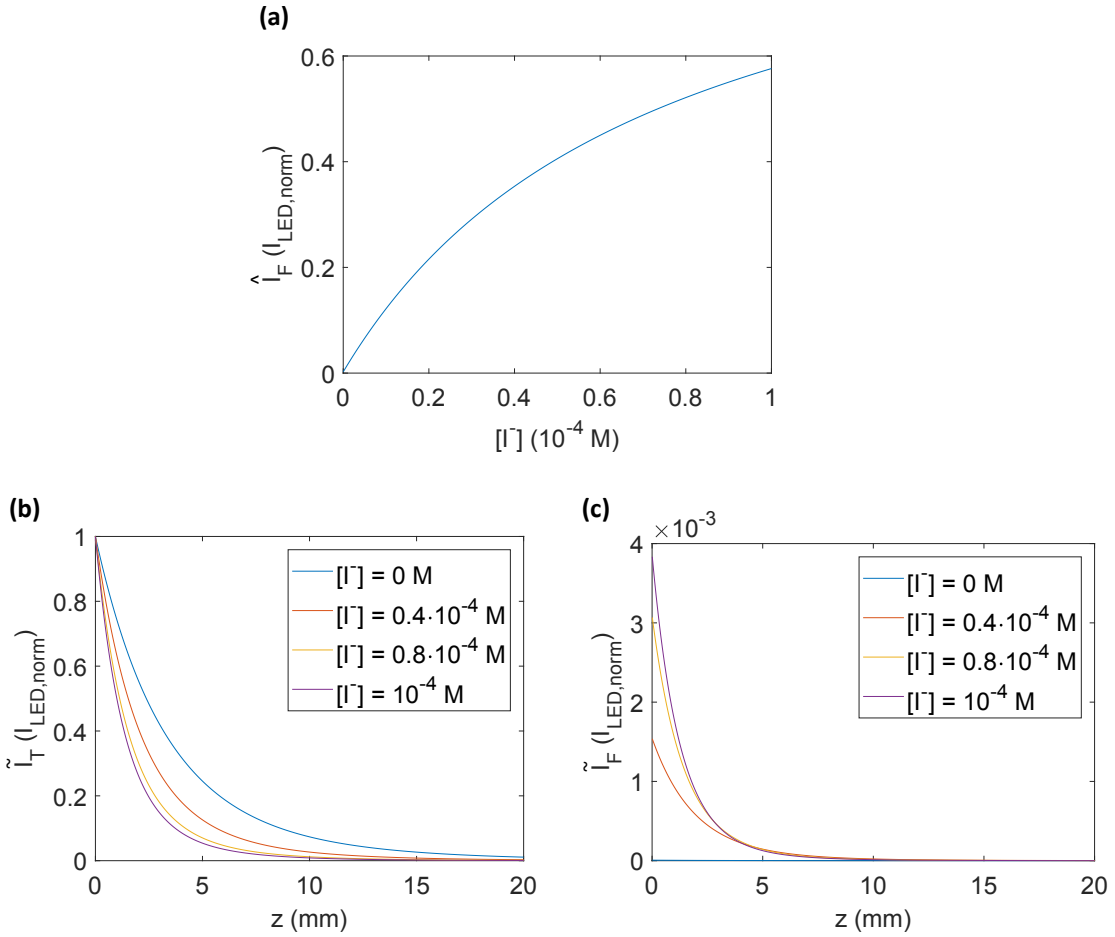

Fig. 5.16: Exemplary simulation results calculated for the LED spectrum of the BLI setup, assuming constant concentration profiles and total dye concentrations of $[I]_{tot} = [T]_{tot} = 10^{-4}$ M. The calculations are performed as a function of $[I^-]$, as described in the text. (a) Depth-integrated fluorescence intensity $\hat{I}_F$ as a function of $[I^-]$. (b) and (c) show the depth profiles of the total transmitted intensity $\tilde{I}_T$ and the fluorescence intensity $\tilde{I}_F$, respectively. The spectral integral of the light source $I_{LED,norm}$ serves as a unit of intensity.

Figure 5.16 shows exemplary simulation results calculated with the LED spectrum $I_{0,LED}(\lambda_k)$ of the BLI setup as a function of $[I^-]$. The spectral integral of $I_{0,LED}(\lambda_k)$

$$I_{LED,norm} = \sum_k I_{0,LED}(\lambda_k)\Delta\lambda_k. \tag{5.23}$$

serves as a unit of intensity. Furthermore, constant concentration profiles $c_1(z) = [\mathrm{IH}]$, $c_2(z) = [\mathrm{I^-}]$, $c_3(z) = [\mathrm{TH}]$, $c_4(z) = [\mathrm{T^-}]$ and total dye concentrations of $[\mathrm{I}]_{\mathrm{tot}} = [\mathrm{T}]_{\mathrm{tot}} = 10^{-4}\,\mathrm{M}$ are assumed. As this does not describe the situation during an invasion experiment with ammonia, the constant values are intended to be average values along the water column. For each calculation, $[\mathrm{I^-}]$ takes a value between zero and $[\mathrm{I}]_{\mathrm{tot}}$ using a sufficiently fine step size, while $[\mathrm{IH}] = [\mathrm{I}]_{\mathrm{tot}} - [\mathrm{I^-}]$, $[\mathrm{TH}] = [\mathrm{T}]_{\mathrm{tot}}$ and $[\mathrm{T^-}] = 0$ are set for the other dye components. With the simulation results for the depth profiles of the total transmitted intensity $\tilde{I}_{\mathrm{T}}$, the penetration depth of the LED light is determined for the case $[\mathrm{I^-}] = 10^{-4}\,\mathrm{M}$ as the depth at which the intensity is reduced to $1/e$ of its initial value. The simulation yields about 1.4 mm. The same calculation performed for the emission wavelength of the laser gives 0.9 mm.

5.6.2 Calibration of the measured fluorescence intensity

The calibration measurement series was performed at the wind-wave tunnel with the instrumentation as described in Sec. 4. The tunnel was filled with deionized water up to the standard water level. Pyranine ($m_{\mathrm{I}_{\mathrm{tot}}} \simeq 6.82\,\mathrm{g}$) and tartrazine ($m_{\mathrm{T}_{\mathrm{tot}}} \simeq 6.95\,\mathrm{g}$) were added to the water, corresponding to a concentration of the dyes of about $10^{-4}\,\mathrm{M}$. The tunnel was closed afterwards. The measurement series started in the alkaline regime at pH ~ 9, which was set by adding NaOH solution. The conductivity of the water was $\kappa \simeq 120\,\mu\mathrm{S/cm}$. For the experiment, the concentration ratio of the two pyranine components was adjusted by adding certain amounts of a 1 M HCl solution with a syringe. For this, a small injection opening was used that was closed after each addition. The concentrations of the dyes were continuously measured with the transmission probe. After each addition of HCl, the water was mixed by using the wind engine and the pumps in the bypasses. When the water had become well mixed, which was recognized by the fact that the measured concentrations approached constant values, the wind engine and the pumps were turned off. The pH value was recorded. With the BLI and the LIF setup 100 and 200 images of the fluorescence signal were recorded and averaged, respectively. The measurement series includes in total 20 of these measurements at different pH values between 6 and 9. The evaluation of the acquired data comprises an analysis of the concentration data acquired with the transmission probe as well as a comparison of the fluorescence intensities measured by the cameras with the simulation. As the BLI and the LIF cameras measured different signals, the two setups are treated separately.

Analysis of the concentration data

Figure 5.17 shows the measured concentration values of the dyes as a function of the HCl concentration calculated from the added volume. Tartrazine stayed mostly in its acidic form. As predicted by the calculation in Sec. 3.3, the concentration of the alkaline form of pyranine [I^-] decreases linearly with [HCl] around the equivalence point. The concentration of the acidic form [IH] increases correspondingly. A linear fit is applied to each data set. The absolute values of the resulting proportionality factors, which are expected to be the same, are averaged, yielding

$$a_{\mathrm{HCl,I^-}} = 0.85 \pm 0.05. \tag{5.24}$$

Their difference is taken as an upper error estimate. This result is in good agreement with the theoretical estimation in Eq. 3.17.

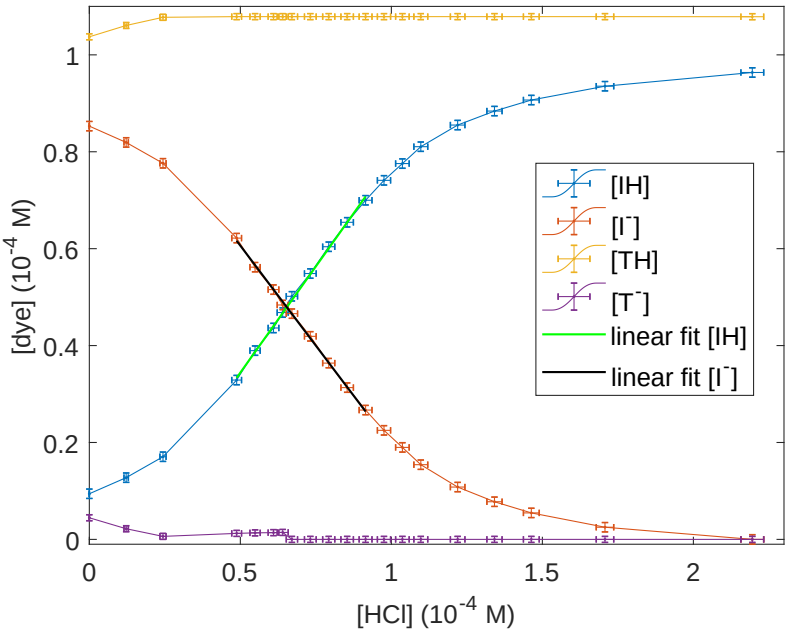

Fig. 5.17: Concentrations of the dye components versus the concentration of added HCl. The linear fits yield the proportionality factor $a_{\mathrm{HCl,I^-}}$.

BLI

The BLI images are preprocessed as described in Sec. 5.5. Figure 5.18 shows exemplary images recorded by the top BLI camera B4 for different concentrations of the alkaline pyranine component I^- measured with the transmission probe. The

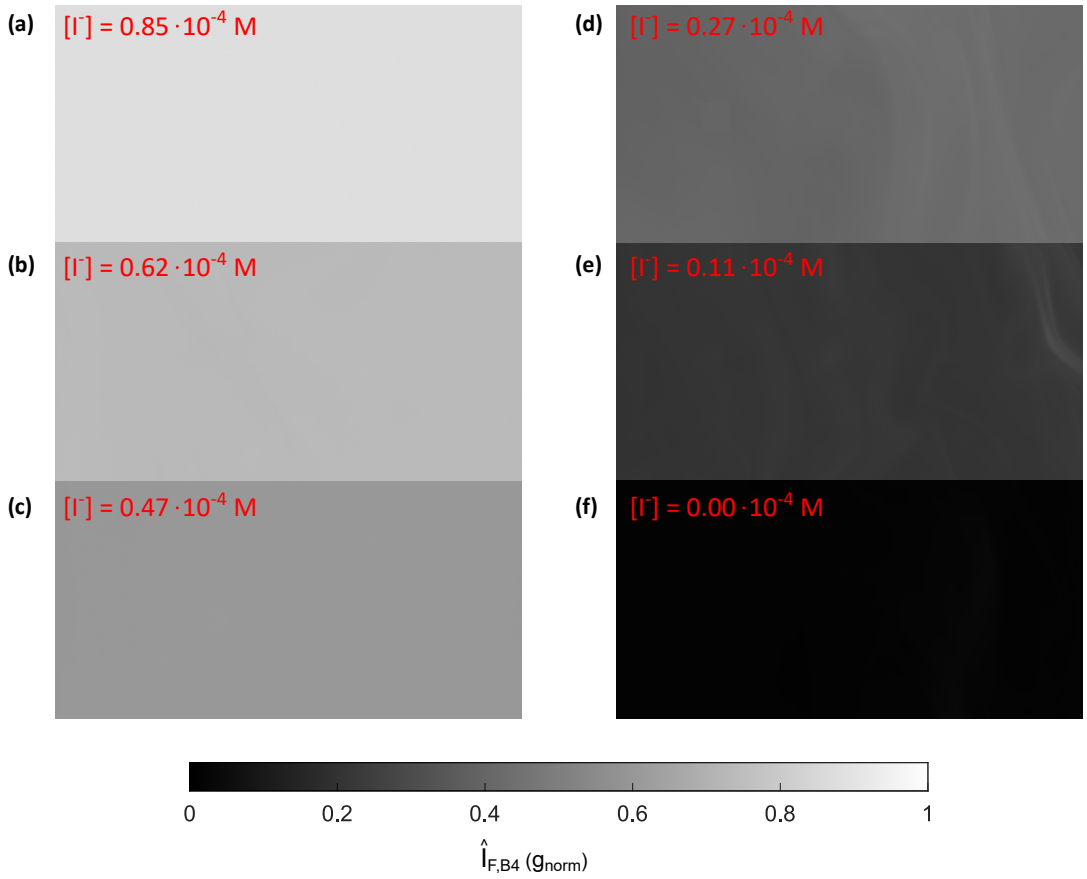

Fig. 5.18: Preprocessed example images of the fluorescent water recorded by the top BLI camera B4 ($921 \times 470\,\mathrm{px}$) during the calibration measurement series. The shown intensity corresponds to the depth-integrated fluorescence intensity $\hat{I}_{\mathrm{F,B4}}$. The concentration of the alkaline form of pyranine [I^-] measured with the transmission probe is shown in the top left corner of each image and decreases from (a)-(f).

gray values correspond to the depth-integrated fluorescence intensity $\hat{I}_{\mathrm{F,B4}}$. For each camera, the gray values of each image are averaged. Brighter regions as visible in Fig. 5.18 (d) and (e) were excluded from the average. They are related to a local increase of [I^-]. This means that the solution had become less acidic, which was most likely caused by the gas exchange of CO_2 from the water to the air space, as no other reacting gases were present in the wind-wave tunnel.

The averaged gray values are plotted in Fig. 5.19 versus the concentration [I^-]. Now, the simulation of the fluorescence signal (see Sec. 5.6.1) is employed. Since the water was well mixed for each measurement, a homogeneous concentration distribution and hence constant concentration depth profiles can be assumed. As a consequence, the values measured with the transmission probe can be used as input parameters for

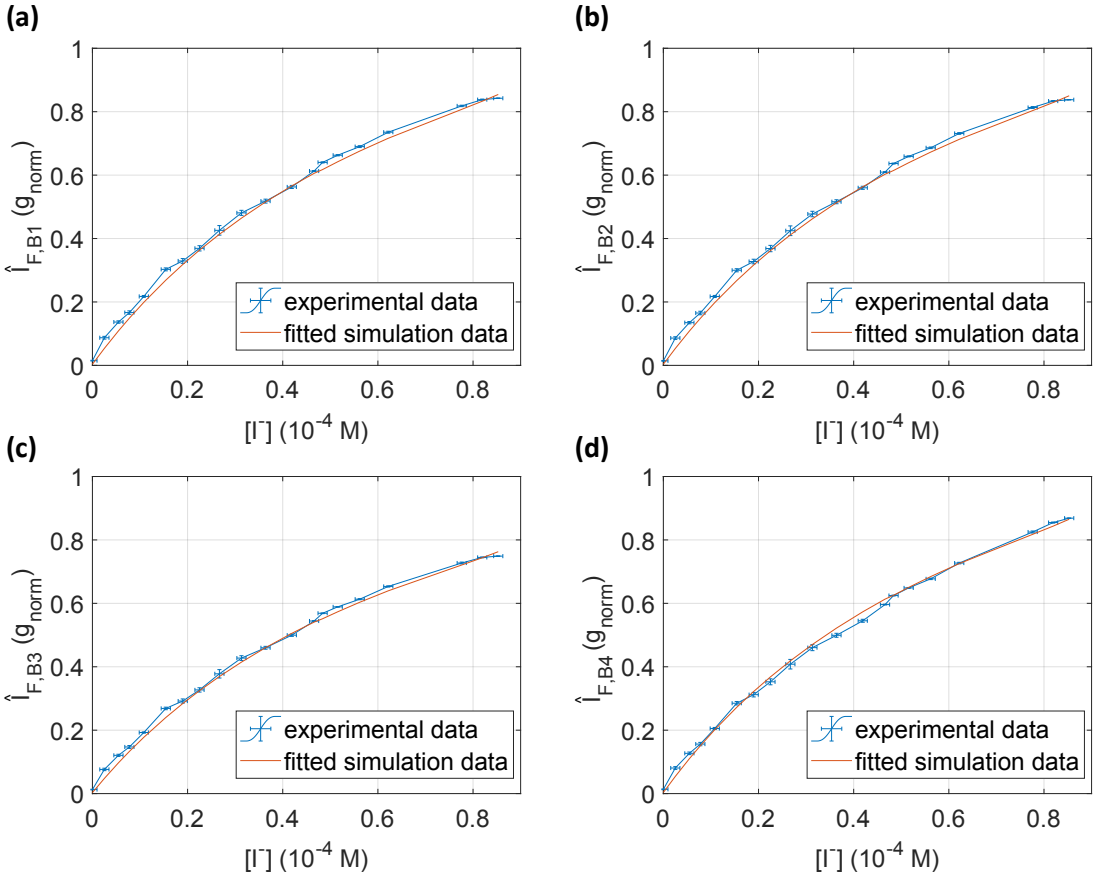

Fig. 5.19: Depth-integrated fluorescence intensity $\hat{I}_\mathrm{F}$ measured by the BLI cameras ((a): B1, (b): B2, (c): B3, (d): B4) as a function of the concentration $[\mathrm{I}^-]$ of the alkaline pyranine component. The concentration was measured with the transmission probe. Besides, simulation data fitted to the experimental data are shown.

the simulation by setting $c_1(z) = [\mathrm{IH}]$, $c_2(z) = [\mathrm{I}^-]$, $c_3(z) = [\mathrm{TH}]$, $c_4(z) = [\mathrm{T}^-]$. The simulation data are calculated for each of the 20 measurements and fitted according to Eq. 5.22a to the fluorescence intensity obtained with the cameras. The fitted curves are shown in Fig. 5.19. The proportionality factors with the respective uncertainties obtained from the fits are

$$\sigma_{\mathrm{B1}} = 1.63 \pm 0.01, \tag{5.25a}$$
$$\sigma_{\mathrm{B2}} = 1.62 \pm 0.01, \tag{5.25b}$$
$$\sigma_{\mathrm{B3}} = 1.46 \pm 0.01, \tag{5.25c}$$
$$\sigma_{\mathrm{B4}} = 1.65 \pm 0.01. \tag{5.25d}$$

With this calibration, the concentration of the alkaline pyranine component $[\mathrm{I}^-]$ can be determined from the depth-integrated fluorescence intensity measured by the BLI cameras for given concentration profiles of the dyes.

LIF

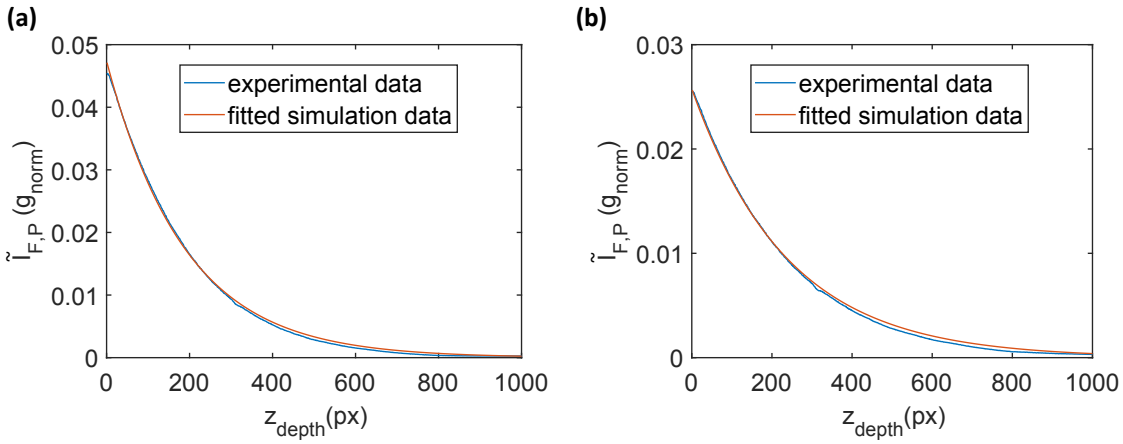

Fig. 5.20: Exemplary fluorescence profiles $\tilde{I}_{\mathrm{F,P}}$ in units of the normalized gray scale g_{norm}, extracted from the LIF images that were recorded during the calibration measurement series ((a): no. 1, (b): no. 8). Simulation results are fitted to the experimental data.

From the recorded LIF images, the fluorescence profiles are extracted as described in Sec. 5.5.2. To find the proportionality factor σ_{P} of the profile camera, $\tilde{I}_{\mathrm{F}}$ obtained from the simulation with the measured concentrations is fitted to the data according to Eq. 5.22b. In order to perform the fit, the real world depths used in the simulation are matched to the pixel depths z_{depth} using the magnification factor in Eq. 5.16. Figure 5.20 shows two fluorescence profiles with the fits. The fit is performed for each of the 20 measurements. The resulting proportionality factors are averaged, yielding

$$\sigma_{\mathrm{P}} = 101 \pm 4, \tag{5.26}$$

where the standard deviation of the factors is assumed as an error estimate.

6. Experiments

In this chapter, the invasion experiments with ammonia conducted at the Heidelberg linear wind-wave tunnel are described. Two types of experiments were performed.

In one set of experiments, ammonia was injected over short time periods. The concentration change of the pyranine components that followed the gas invasion was measured and related to the amount of ammonia that had entered the water. For this type of measurements, the spectroscopy setups were employed. The experiments aim to verify the linear relationship between $[NH_3]_{w,tot}$ and $[I^-]$ (see Eq. 3.5).

A second set of measurements with constant air-side ammonia flux into the water was performed. These experiments involved the complete setup including the imaging setups. With the data of the spectroscopy setups and the recorded images, the air-side and the water-side concentration fluxes are inferred and compared with regard to the proportionality given in Eq. 3.6.

For both types of measurements, the following preparations were conducted. The tunnel was filled with deionized water up to the standard water level $z_{ws,0} = 9.2\,\mathrm{cm}$. Pyranine ($m_{I_{tot}} \simeq 6.82\,\mathrm{g}$) and tartrazine ($m_{T_{tot}} \simeq 6.95\,\mathrm{g}$) were added to the water. This resulted in total dye concentrations of

$$[I]_{tot} = (1.02 \pm 0.01) \cdot 10^{-4}\,\mathrm{M},$$
$$[T]_{tot} = (1.07 \pm 0.01) \cdot 10^{-4}\,\mathrm{M},$$

measured with the transmission probe. During the experiments the tunnel was closed. The water was continuously cooled with the Peltier temperature control and the wind engine frequency was set to 15 Hz. The circulation and the analysis loops were flushed. The measurement conditions were monitored by the peripheral instruments. The spectroscopy setups were used to continuously measure the air-side ammonia and the water-side dye concentrations.

6.1 Invasion experiments with short gas injection

For the experiments with short gas injections, three measurement series were performed. The measurement procedure is exemplarily explained for measurement series no. 1 in the following.

The series started in the acidic regime at pH = 5.84 and comprised eight injections of ammonia. The gas was injected for one minute with the mass flow controller. After

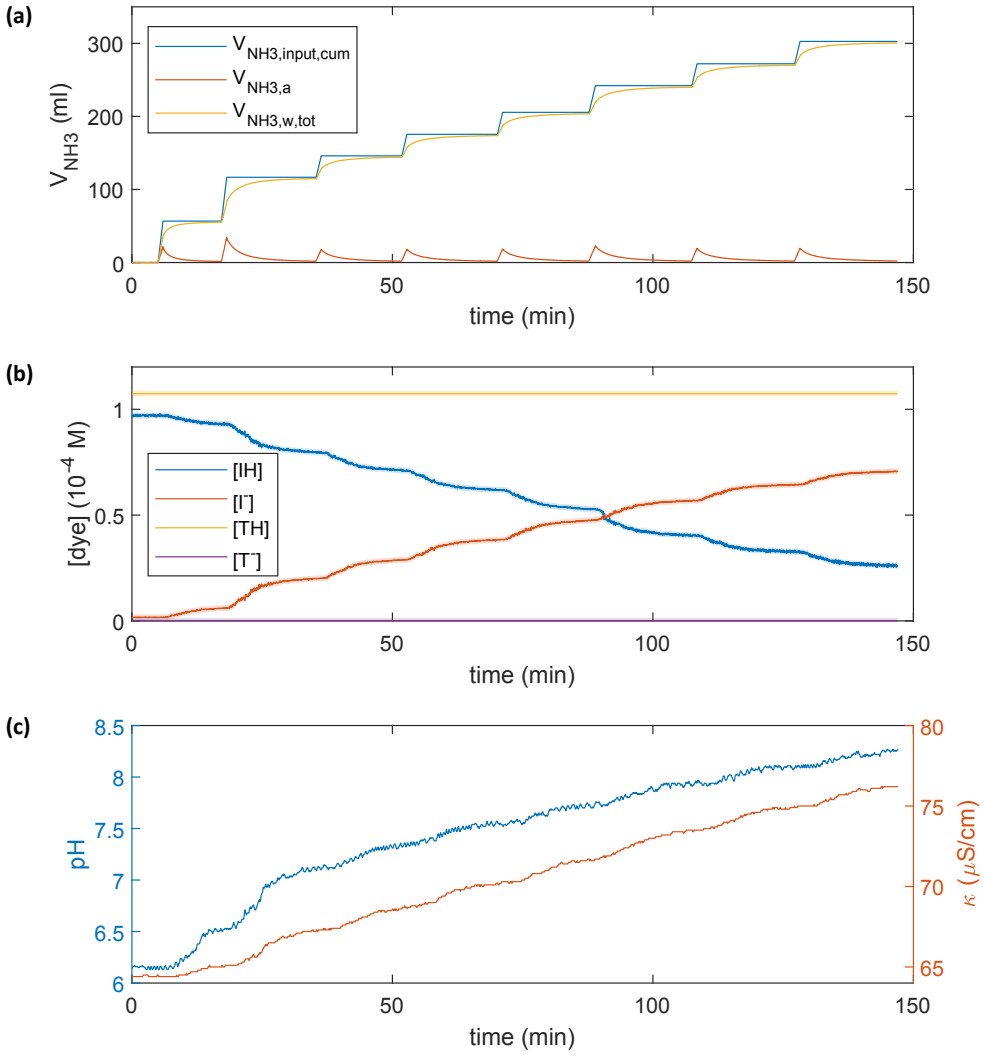

Fig. 6.1: Temporal overview of series no. 1 of the experiments with short ammonia injections (see Tab. 6.1). (a) Gas volume of ammonia V_{NH3}, where the different labels denote the total cumulative input ($V_{\mathrm{NH3,input,cum}}$) as well as the air-side ($V_{\mathrm{NH3,a}}$) and the water-side ($V_{\mathrm{NH3,w,tot}}$) volume. (b) Concentrations of the dye components IH, I^-, TH and T^-, where the shaded areas indicate the uncertainties. (c) pH and conductivity κ.

each gas input, a maximum air-side ammonia concentration was reached followed by a decay caused by gas exchange with the water. Between successive gas inputs, time was given for equilibration. It was waited until the air-side ammonia concentration had dropped to a value below the lower measurement limit of the UV spectroscopy setup of 10^{-8} M and the concentration of the pyranine components had not changed by more than 10^{-6} M within a time of 3 min. This period of time was chosen, as

the time delay between the ammonia input and the first concentration change of the pyranine components was found to be typically around 2 min. Figure 6.1 (a) shows the amount of ammonia, given as a gas volume V_{NH3}, as a function of time. Here, $V_{\mathrm{NH3,input,cum}}$ denotes the cumulative amount of ammonia that was injected in total during the experiment. Each step of the curve corresponds to a gas injection. The injected volume of ammonia was calculated with the corrected flow rate F_{corr} (see Sec. 5.4) and the input time. The air-side volume $V_{\mathrm{NH3,a}}$ was calculated from the air-side concentration measurement with the UV spectroscopy setup. Since the leakage rate could be neglected (see Sec. 5.3), the amount of ammonia entering the water $V_{\mathrm{NH3,w,tot}}$ was calculated as the difference between $V_{\mathrm{NH3,input,cum}}$ and $V_{\mathrm{NH3,a}}$. Figure 6.1 (b) shows the concentrations of the dye components measured with the transmission probe. As required, tartrazine stayed in its acidic form. This was also found for the other measurement series. The measured pH and conductivity values are illustrated in Fig. 6.1 (c).

series no.	1	2	3
$V_{\mathrm{NH3,input}}$ (ml)	60, 60, 30, 30, 30, 30, 30, 30	60, 60, 60, 60	60, 60, 60, 60, 60, 60
$[\mathrm{I}^-]_{\mathrm{start}}, [\mathrm{I}^-]_{\mathrm{end}}$ (10^{-4} M)	0.02, 0.71	0.05, 0.65	0.07, 0.64
$\mathrm{pH}_{\mathrm{start}}, \mathrm{pH}_{\mathrm{end}}$	5.84, 7.96	6.28, 7.86	6.37, 7.84
$\kappa_{\mathrm{start}}, \kappa_{\mathrm{end}}$ (µS/cm)	64.4, 76.2	76.2, 85.9	90.0, 102.1
$\langle T_{\mathrm{a}} \rangle_t$ (°C)	22.46	22.47	22.47
$\langle T_{\mathrm{w}} \rangle_t$ (°C)	20.31	20.34	20.34
$\langle p_{\mathrm{a}} \rangle_t$ (mbar)	1009	1009	1008
$\langle H_{\mathrm{a}} \rangle_t$ (%)	99.8	98.2	99.1
$\langle u \rangle_t$ (m/s)	3.83	3.82	3.82

Table 6.1: Summary of the measurement conditions for the experiments with short ammonia injections in chronological order. The listed quantities are the volume of ammonia $V_{\mathrm{NH3,input}}$ injected within one minute, the concentration of the alkaline pyranine component $[\mathrm{I}^-]$, the pH and the conductivity κ. Furthermore, the temporal mean values of the air temperature $\langle T_{\mathrm{a}} \rangle_t$, water temperature $\langle T_{\mathrm{w}} \rangle_t$, air pressure $\langle p_{\mathrm{a}} \rangle_t$, air humidity $\langle H_{\mathrm{a}} \rangle_t$ and the plateau wind speed $\langle u \rangle_t$ are shown. The labels "start" and "end" refer to the beginning and the end of a measurement series.

After completion of the measurement series, HCl was added to the water to restore the initial concentrations of the pyranine components. In this way, the chemical system was prepared for the next series. The amount of added HCl corresponded

to a concentration of roughly $[I^-]_{end} - [I^-]_{start}$, where $[I^-]_{start}$ and $[I^-]_{end}$ denote the values of $[I^-]$ at the beginning and the end of the series, respectively. The fact that the system could be controlled in such a defined way is based on the proportionality between the concentration of the pyranine components and HCl (see the discussion at the end of Sec. 3.3 and the experimental result in Sec. 5.6.2).

Table 6.1 summarizes the measurement conditions of the three series including the input volumes of ammonia. The values of the concentration of the alkaline pyranine component, the pH and the conductivity at beginning and the end of each series are listed. Since the air-side and water-side temperatures, the static air pressure, the air humidity and the plateau wind speed were relatively stable, only their average values, indicated by angle brackets, are given.

6.2 Invasion experiments with constant gas flux

With the experiments presented in the following, images of the fluorescence signal were acquired at constant ammonia flux $j_{a,NH3}$ from the air space into the water. Modeling the wind-wave tunnel with the box model (see Sec. 3.4), a constant ammonia flux into the water can be assumed if the air-side ammonia concentration $[NH_3]_a$ is constant during the gas input. This corresponds approximately to a steady state between the air and the water space, where the rate at which ammonia is injected into the tunnel is equal to the rate at which it dissolves in the water, since the leakage rate is negligible. If the flux into the water is constant, the water-side ammonia concentration increases approximately linearly. Based on the considerations presented in Sec. 3.1, it is expected that the concentration of the alkaline pyranine component and hence the fluorescence intensity imaged by the BLI cameras increase, too.

It turned out that with the employed chemical system a steady state could not be achieved by setting a certain constant input rate. The reason for this is that the initial pH value at ~ 5.5 is close to the neutral point such that the water has become already alkaline before a constant air-side ammonia concentration is reached. In the alkaline regime, the fluorescent streaks resulting from the instantaneous gas invasion cannot be distinguished then from the high background signal as the whole water bulk emits fluorescence. Moreover, it is difficult to reach a steady state because the effective solubility of ammonia changes exponentially with the pH (see Fig. 3.3). To overcome these problems, the following procedure was applied. Prior to the image acquisition a high flow rate ($F_{corr} \geq 50\,\mathrm{ml/min}$) is used. The value of $[NH_3]_a$ provided by the UV spectroscopy setup is observed. Having reached a certain value, the flow rate is reduced appropriately such that the concentration stays approximately at that value. As a result, a steady state with a concentration $[NH_3]_{a,ss}$ is reached faster than with

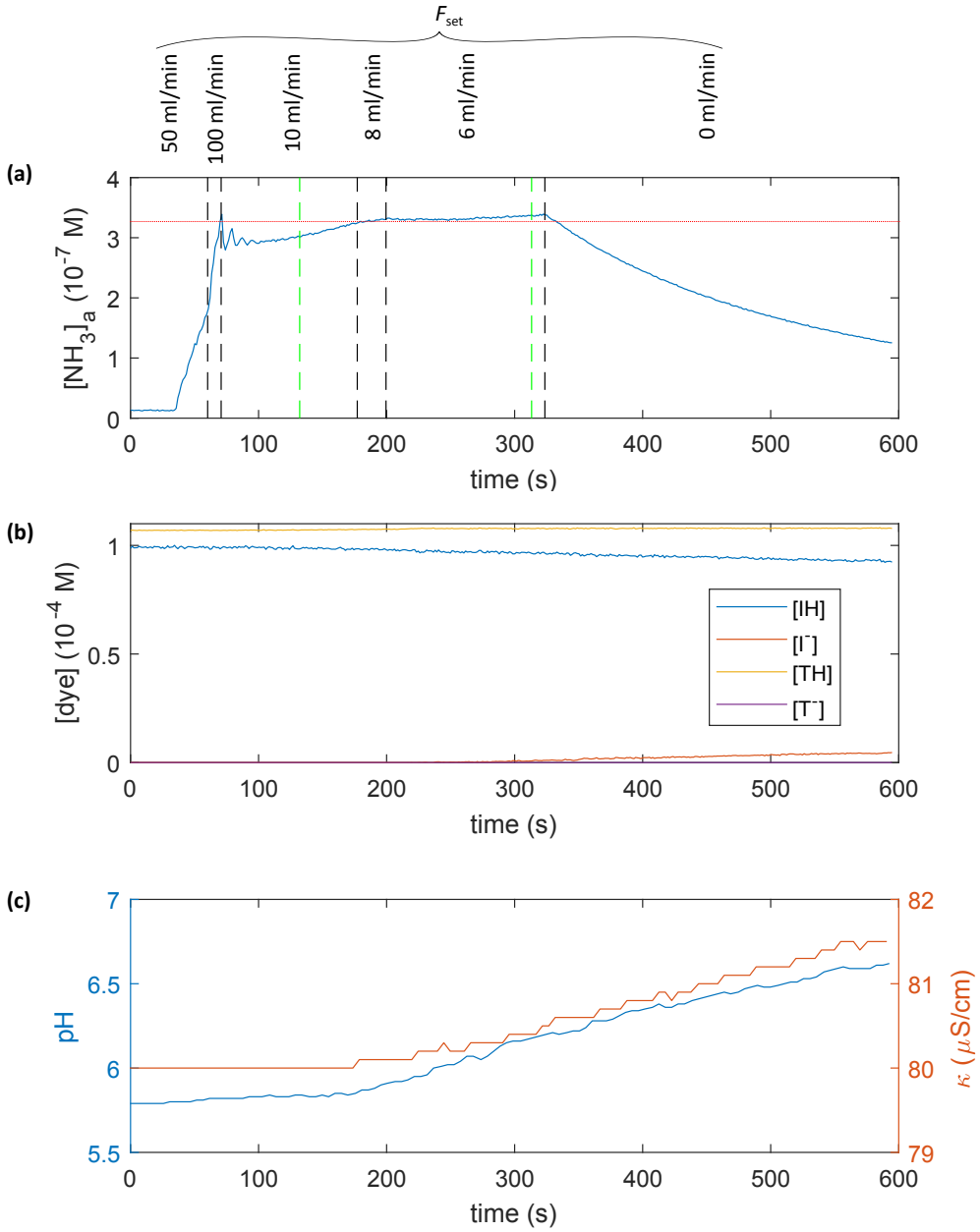

Fig. 6.2: Temporal overview of measurement no. 5 with constant ammonia flux into the water (see Tab. 6.2). (a) Air-side ammonia concentration $[NH_3]_a$ (blue) measured with the UV spectroscopy setup. The flow rates set at the mass flow controller are indicated at the top, where the black dashed lines mark the points of time when the flow rate was changed. The green dashed lines mark the beginning and the end of the measurement time during which images were recorded. The average concentration within this time period is assumed as the steady-state concentration $[NH_3]_{a,ss}$ (red). (b) Concentrations of the pyranine and the tartrazine components IH, I^-, TH and T^-. (c) pH and conductivity κ.

a lower ammonia input rate and the acquisition of images is started. The flow rates that are set to reach certain steady-state concentrations were found experimentally by testing. Since the effective solubility of ammonia decreases, if the pH increases, the flow rate is lowered further during the experiment to avoid an increase of the air-side ammonia concentration. After the image acquisition, the ammonia injection is switched off.

As a starting point for the measurements, the concentration of the alkaline pyranine component was set to $[I^-] \simeq 0.01 \cdot 10^{-4}\,\mathrm{M}$ corresponding to an initial pH value of ~ 5.5. This starting point was preferred over the initial pH value of ~ 6, as it provided a small buffer until the water turned alkaline. This gave more time to adjust the ammonia flow rate correctly. A recording time of 3 min was found to be suitable to avoid a high background fluorescence towards the end of a measurement. With each BLI camera, a sequence of 72000 images at 400 Hz and with the LIF camera a sequence of 144000 images at 800 Hz were acquired during a measurement. Before each measurement, reference images with a resting water surface were recorded.

Figure 6.2 (a) illustrates exemplarily for measurement no. 5 that with the described procedure a relatively constant value of the concentration $[NH_3]_a$ could be achieved. The average of the concentration values measured during the image acquisition was assumed as the steady-state concentration $[NH_3]_{a,ss}$. The corresponding temporal evolution of the concentrations of the pyranine components, the pH and the conductivity are shown in Fig. 6.2 (b) and (c), respectively. Tartrazine stayed in its acidic form.

In total nine measurements of this type at different steady-state concentrations $[NH_3]_{a,ss}$ were conducted. The set steady-state concentrations were chosen in a range to investigate if the saturation of the indicator (see Sec. 3.3) can be observed. There it was stated that the saturation of the indicator can be avoided if the (local) water-side ammonia concentration does not exceed the total indicator concentration $[I]_{tot} \simeq 10^{-4}\,\mathrm{M}$. Due to the fact that the experiment is designed to be an invasion, the highest water-side concentrations of ammonia are expected to be at the water surface. This leads to the limit $[NH_3]_{w,tot,s} = 10^{-4}\,\mathrm{M}$. To estimate the corresponding limit for the air-side bulk concentration $[NH_3]_{a,b}$, that is measured with the UV spectroscopy setup, a constant flux $j_{a,NH3} = j_{w,NH3}$ is assumed. Moreover it can be assumed that $[NH_3]_{a,s} = 0$ due to the high solubility and $[NH_3]_{w,tot,b} = 0$ in the water bulk. This leads to

$$j_{a,NH3} = j_{w,NH3} \Rightarrow [NH_3]_{a,b} = \frac{R_a}{R_w}[NH_3]_{w,tot,s}. \tag{6.1}$$

The equations 2.43a and 2.43b can be used for the air- and the water-side transfer resistances R_a and R_w because of the low air- and high water-side Schmidt number

of ammonia with $\mathrm{Sc_a} \simeq 0.7$ and $\mathrm{Sc_w} \simeq 600$. Assuming the limit of a wavy water surface, 1/2 is used for the Schmidt number exponent on the water side. It follows that

$$[\mathrm{NH_3}]_{\mathrm{a,b}} = \frac{15.2\mathrm{Sc_a^{0.61}}}{12.1\mathrm{Sc_w^{1/2}}}\sqrt{\frac{\rho_\mathrm{a}}{\rho_\mathrm{w}}}[\mathrm{NH_3}]_{\mathrm{w,tot,s}}. \tag{6.2}$$

Inserting the numerical values, the approximation for the air-side concentration limit reads

$$[\mathrm{NH_3}]_{\mathrm{a,b}} \approx 1.4 \cdot 10^{-3} \cdot [\mathrm{NH_3}]_{\mathrm{w,tot,s}} = 1.4 \cdot 10^{-7}\,\mathrm{M}, \tag{6.3}$$

at which a transition of the indicator from the unsaturated to the saturated case is expected. Table 6.2 summarizes the measurement conditions during the image recordings. The set of measurements is sorted by the ammonia flux $j_{\mathrm{a,NH3}}$ into the water. In Sec. 8.2, it will be explained how the flux was determined. Fresh water was prepared once in between the measurements to avoid higher ion concentrations and a potential change of the dissociation constant of pyranine.

no.	$j_{a,NH3}$ (10^{-5} $\frac{mol}{m^2 s}$)	$[NH_3]_{a,ss}$ (10^{-7} M)	F_{corr} (ml/min)	$[I^-]_{start}, [I^-]_{end}$ (10^{-4} M)	pH_{start}, pH_{end}	$\kappa_{start}, \kappa_{end}$ (µS/cm)	$\langle T_a \rangle_t$ (°C)	$\langle T_w \rangle_t$ (°C)	$\langle p_a \rangle_t$ (mbar)	$\langle H_a \rangle_t$ (%)	$\langle u \rangle_t$ (m/s)
1	0.136	0.70	3.5, 3.4, 3.1, 2.9, 2.8	0.01, 0.01	6.12, 6.20	76.2, 76.3	22.55	20.63	1002.4	99.8	3.80
2	0.140	0.51	3.5, 3.1, 2.9, 2.8	0.00, 0.00	5.85, 5.93	77.9, 78.0	20.76	20.67	1002.2	99.5	3.80
3	0.206	0.78	6.6, 5.1, 4.3, 3.5	0.01, 0.02	6.12, 6.28	75.1, 75.2	22.42	20.66	1001.9	97.0	3.80
4	0.293	1.85	8.9, 6.6, 5.8, 5.1	0.00, 0.01	6.03, 6.18	85.3, 85.6	22.09	19.63	993.7	94.4	3.82
5	0.377	3.27	10.5, 8.9, 7.4	0.00, 0.01	5.84, 6.17	80.0, 80.4	22.19	19.90	987.1	99.3	3.83
6	0.508	4.49	13.0, 12.0, 10.5, 8.9	0.00, 0.04	6.08, 6.44	89.7, 90.4	22.89	20.77	1002.6	99.1	3.80
7	0.572	6.16	18, 15, 10.5	0.00, 0.01	5.51, 6.09	74.4, 74.7	22.11	19.78	987.4	98.6	3.83
8	0.657	5.78	15, 13	0.07, 0.19	6.63, 6.90	66.4, 67.2	21.98	19.55	988.1	97.4	3.84
9	1.673	11.20	50.0, 40.0, 30.0	0.00, 0.18	5.80, 6.83	79.2, 80.6	22.82	20.71	1002.6	98.6	3.80

Table 6.2: Summary of the measurement conditions. The set of measurements is sorted by the air-side ammonia flux $j_{a,NH3}$ into the water. The other listed quantities are the steady-state concentration of ammonia $[NH_3]_{a,ss}$, the corrected ammonia flow rate F_{corr} (see Sec. 5.4), the concentration of the alkaline pyranine component $[I^-]$, the pH and the conductivity κ. Furthermore, the mean values of the air temperature $\langle T_a \rangle_t$, water temperature $\langle T_w \rangle_t$, air pressure $\langle p_a \rangle_t$, air humidity $\langle H_a \rangle_t$ and the plateau wind speed $\langle u \rangle_t$ during an image recording are shown. The labels "start" and "end" refer to the beginning and the end of an image recording. During each measurement, different ammonia flow rates were set to keep the air-side ammonia concentration constant.

7. Image processing

This chapter addresses the evaluation of the BLI and the LIF images recorded during the invasion experiments with ammonia (see Sec. 6.2). All images are preprocessed as described in Sec. 5.5. The next evaluation steps which include a statistical analysis and the extraction of physical parameters are explained in the following with example images from measurement no. 5 (see Tab. 6.2).

7.1 BLI images

It will be shown how mean concentrations of the alkaline pyranine component are obtained. Moreover, statistical measures of the determined concentration values are discussed, as they are useful to recognize systematic changes and trends in the large set of recorded data.

7.1.1 Determination of mean concentrations

Figure 7.1 (a) shows a typical BLI image recorded by the top BLI camera (B4). The fluorescent streaks resulting from the gas transfer are aligned in wind direction and exhibit a variety of complex turbulent structures. The width of the visible structures typically ranges from 1 mm to 1 cm. The brightest structures are close to the water surface and indicate that high amounts of ammonia entered the water at the moment of recording. Less brighter streaks correspond typically to fluorescence signals emitted from larger depths.

To determine the concentration of the alkaline pyranine component, the simulation described in Sec. 5.6.1 is employed. Despite the fact that the concentration depth profiles are not known during the invasion experiment, the simulation can be still used to determine mean concentrations along the water column which will be indicated by an overbar in the following.

Constant profiles $c_1(z) = \overline{[\mathrm{IH}]}$, $c_2(z) = \overline{[\mathrm{I^-}]}$, $c_3(z) = \overline{[\mathrm{TH}]}$, $c_4(z) = \overline{[\mathrm{T^-}]}$, which are intended to represent the mean values, are assumed. The calculation is performed in analogy to the exemplary calculation shown in Sec. 5.6.1, where for the total concentrations of the dyes, the values measured with the transmission probe are used. The fluorescence intensities are calculated for different values of $\overline{[\mathrm{I^-}]}$ in a range from zero to $[\mathrm{I}]_{\mathrm{tot}}$, while $\overline{[\mathrm{IH}]} = [\mathrm{I}]_{\mathrm{tot}} - \overline{[\mathrm{I^-}]}$, $\overline{[\mathrm{TH}]} = [\mathrm{T}]_{\mathrm{tot}}$, $\overline{[\mathrm{T^-}]} = 0$ are set. In a good

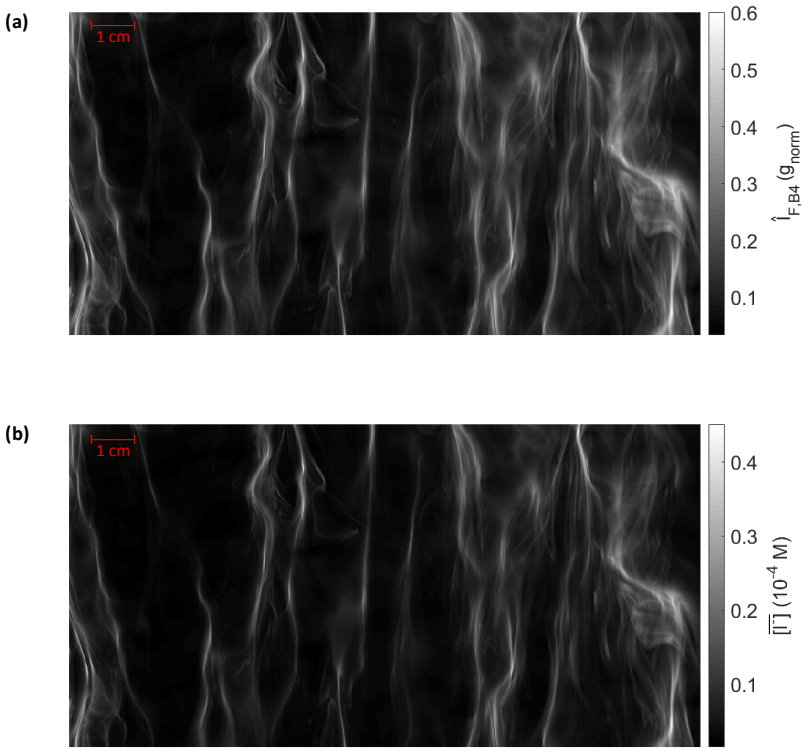

Fig. 7.1: (a) BLI image recorded by the top camera B4 during an invasion experiment with ammonia, showing fluorescent streaks as a consequence of the gas transfer. The visible intensity corresponds to the depth-integrated fluorescence $\hat{I}_{\mathrm{F,B4}}$ in units of the normalized gray scale g_{norm}. The scale in the top left corner indicates 1 cm in real world coordinates. (b) Mean concentrations of the alkaline pyranine component $\overline{[\mathrm{I}^-]}$ determined for each pixel of the image in (a).

approximation, tartrazine is assumed to stay in its acidic form. The calculations yield a curve for the depth-integrated fluorescence intensity $\hat{I}_{\mathrm{F}}$ as shown in Fig. 7.2.

A gray value $\hat{I}_0$, measured for instance by camera B4, is converted to a simulation value $\hat{I}_{0,\mathrm{sim}} = \hat{I}_0/\sigma_{\mathrm{T}}$ using the results of the calibration measurement (see Eq. 5.25). The corresponding concentration value $\overline{[\mathrm{I}^-]}_0$ is then found by interpolation of the calculated curve, as illustrated in Fig. 7.2. The same method is employed in analogy for the other BLI cameras with the respective proportionality factors.

The gray values of an image can be converted to mean concentration values at once for all pixels of a BLI image. The resulting concentration image determined from Fig. 7.1 (a) is shown in (b).

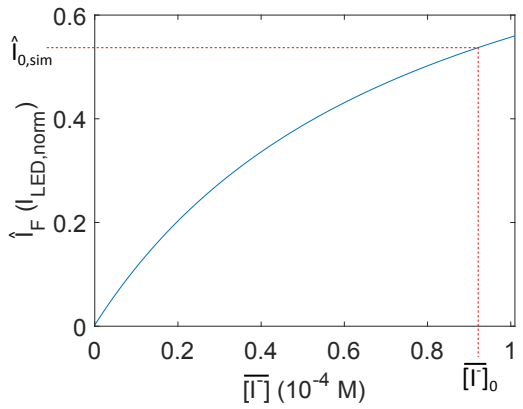

Fig. 7.2: Illustration how the mean concentration of the alkaline pyranine component I^- is determined from a gray value measured with a BLI camera. The shown curve corresponds to the fluorescence intensity calculated as a function of $\overline{[I^-]}$ with the simulations. The value $\hat{I}_{0,sim}$ is obtained from the measured gray value, as described in the text, and the corresponding mean concentration $\overline{[I^-]}_0$ is found by interpolation.

7.1.2 Image statistics

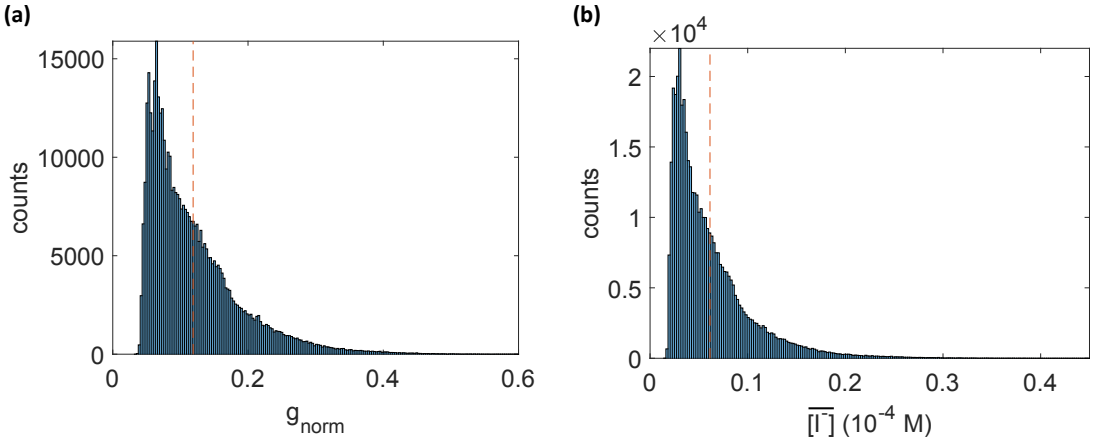

Fig. 7.3: Histograms of the gray values g_{norm} (a) and mean concentrations $\overline{[I^-]}$ (b) of the images in Fig. 7.1. The mean values of the distributions are marked by red lines.

Figure 7.3 shows the histograms of the gray values and the mean concentrations of the images in Fig. 7.1. The average (avg) and the skewness (sk) of the distributions are calculated. Since the bright streaks cover only a small area compared to the dark background, the distributions are always right-tailed. As the gray values themselves bear no physical information, the statistical analysis is continued with the distribution of the concentration values.

In a first approach the average avg($\overline{[I^-]}$) can be used to perform a segmentation of an image by defining it as a threshold to distinguish between streaks and background

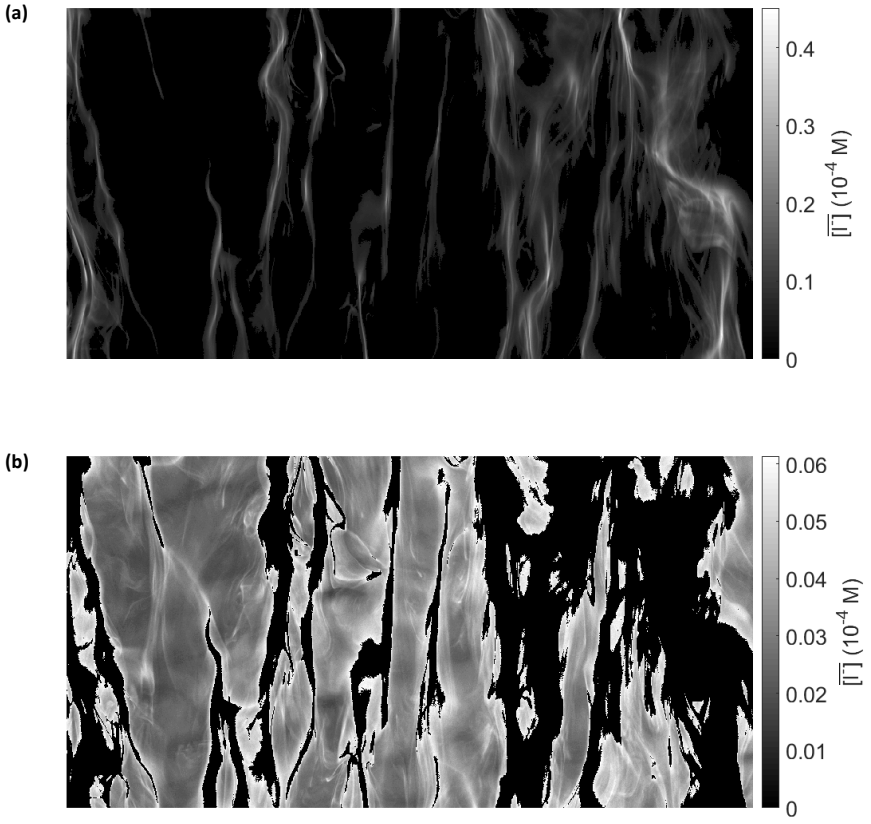

Fig. 7.4: Segmentation of the concentration image in Fig. 7.1 (b). (a) Extracted streak signal $\overline{[\mathrm{I}^-]}_{\mathrm{str}}$, where pixels belonging to the background signal $\overline{[\mathrm{I}^-]}_{\mathrm{bg}}$ are set to zero. (b) Remaining background signal $\overline{[\mathrm{I}^-]}_{\mathrm{bg}}$, where the streak signal $\overline{[\mathrm{I}^-]}_{\mathrm{str}}$ is set to zero.

signal. Pixels with $\overline{[\mathrm{I}^-]} \leq \mathrm{avg}(\overline{[\mathrm{I}^-]})$ are assigned to the background and pixels with $\overline{[\mathrm{I}^-]} > \mathrm{avg}(\overline{[\mathrm{I}^-]})$ to the streak signal. The set of concentration values of streak and background pixels are denoted by $\overline{[\mathrm{I}^-]}_{\mathrm{str}}$ and $\overline{[\mathrm{I}^-]}_{\mathrm{bg}}$, respectively. Figure 7.4 shows the result of this segmentation. It is evident that the brightest streaks are captured, but also in areas assigned to the background lots of fine structures are visible. The segmentation is still useful to obtain the concentration values for the dominant streaks.

With the segmentation, the coverage of the observed water patch by streaks can be quantified by the percentage of streak pixels

$$\xi_{\mathrm{str}} = \frac{N(\overline{[\mathrm{I}^-]}_{\mathrm{str}})}{N(\overline{[\mathrm{I}^-]}_{\mathrm{str}}) + N(\overline{[\mathrm{I}^-]}_{\mathrm{bg}})}, \tag{7.1}$$

with the number of streak $N(\overline{[\mathrm{I}^-]}_{\mathrm{str}})$ and background pixels $N(\overline{[\mathrm{I}^-]}_{\mathrm{bg}})$ in an image.

7.2 LIF images

The evaluation of the LIF images includes a geometric and an intensity analysis. As the laser beam is irradiated from above the water surface, the position of the fluorescence profile changes when waves are present. By detecting the position of the profile, the position and the slope of the water surface can be determined. From the evaluation of the intensity, a concentration depth profile is obtained. With this, the concentration gradient at the water surface and the boundary layer thickness are estimated.

7.2.1 Geometric analysis

Figure 7.5 (a) shows a typical LIF image recorded by the profile camera during the invasion experiment. As a reminder, the water surface is located at the position of the maximum gray value $g_{\max}$. The visible intensity corresponds to an intensity profile along the depth z, where the depth increases to the left. The intensity profile left of the water surface is the true fluorescence profile, while the profile to the right of the water surface is its mirror image. The slope of the fluorescence profile is related to the slope of the water surface, as explained below. The profile images are smoothed with a two-dimensional Gaussian filter which improves the results of the following evaluation steps.

To obtain more reliable results for the water surface position, the positions of gray values $g_{\text{norm}} > 0.95 \cdot g_{\text{norm,max}}$ are found and averaged to give $(z_{\text{ws}}, x_{\text{ws}})$. The uncertainty of this method is estimated to be 1 px for both coordinates. The position of the intensity profile $x_{\text{P}}(z)$ in the z-x plane is found by determining the position of the maximum in each column z. The result is shown in Fig. 7.5 (b). The use of a Gaussian fit to find the position of a maximum was found to be not suitable due to the increase of computational time which could not be compensated by the slight improvement of the result.

By applying a linear fit to $x_{\text{P}}(z)$ up to the water surface $(z_{\text{ws}}, x_{\text{ws}})$, the position $x_{\text{P,fit}}(z)$ and the slope a_{P} of the fluorescence profile are determined (see Fig. 7.5 (b)).

The same geometric analysis is applied to the reference images recorded before each measurement, yielding the height of the water surface $z_{\text{ws,0}}$ and the slope of the fluorescence profile $a_{\text{P,0}}$ at rest. The water surface displacement is then given as $\eta = z_{\text{ws}} - z_{\text{ws,0}}$. With the error estimate of 1 px for the determined water surface positions and the spatial resolution of the profile camera (see Sec. 5.5.2), the uncertainty of η is about 8 µm.

Fig. 7.6 illustrates how the inclination angle of the water surface in wind direction

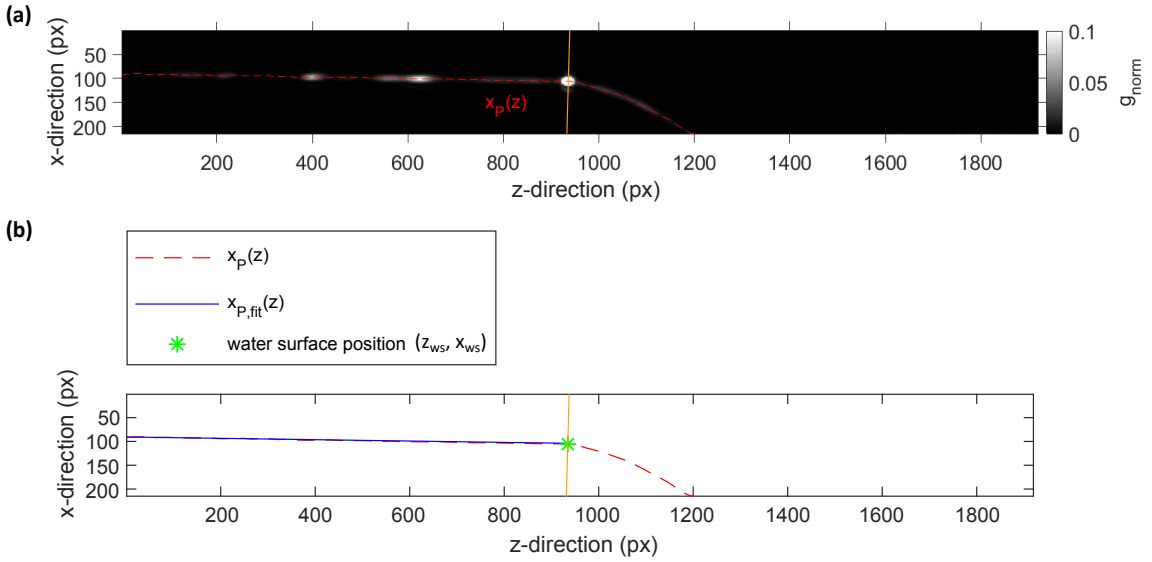

Fig. 7.5: (a) LIF image recorded by the profile camera during an invasion experiment with ammonia. The water surface is indicated by the orange line. The displayed range of gray values is chosen such that also darker regions of the intensity profile are visible. The position of the profile is marked by the red curve $x_\mathrm{P}(z)$. Only the part left of the water surface corresponds to the fluorescence profile. (b) The position of the fluorescence profile is determined with a linear fit $x_\mathrm{P,fit}(z)$, applied to $x_\mathrm{P}(z)$ up to the water surface $(z_\mathrm{ws}, x_\mathrm{ws})$.

δ_x is determined, which yields the slope $\frac{\partial \eta}{\partial x} = \tan(\delta_x)$. The scheme in (a) represents the situation when the water is at rest. The angle δ_0 between the z-direction of the camera and the line perpendicular to the water surface and the angle $\vartheta_\mathrm{a,0}$ between the latter and the laser beam on the air side are unequal zero, because of the not perfect alignment of the beam and the camera. The air- and water-side angles $\vartheta_\mathrm{a,0}$ and $\vartheta_\mathrm{w,0}$ are related by Snell's law

$$\frac{n_\mathrm{a}}{n_\mathrm{w}} = \frac{\sin(\vartheta_\mathrm{w,0})}{\sin(\vartheta_\mathrm{a,0})} \tag{7.2}$$

with the refractive indices of air $n_\mathrm{a} = 1$ and water $n_\mathrm{w} = 1.33$. The corresponding situation, when the water surface is inclined by $\delta_x = \delta - \delta_0$, is shown in Fig. 7.6 (b). From the slopes $a_\mathrm{P,0}$ and a_P of the fluorescence profiles found for the resting and the inclined water surface, the angles

$$\beta_\mathrm{w,0} = \arctan(a_\mathrm{P,0}), \tag{7.3a}$$

$$\beta_\mathrm{w} = \arctan(a_\mathrm{P}) \tag{7.3b}$$

are determined, where $\beta_\mathrm{w,0} = \delta_0 + \vartheta_\mathrm{w,0}$ and $\beta_\mathrm{w} = \delta + \vartheta_\mathrm{w}$. The corresponding angles on the air side are denoted by $\beta_\mathrm{a,0} = \delta_0 + \vartheta_\mathrm{a,0}$ and $\beta_\mathrm{a} = \delta + \vartheta_\mathrm{a}$. As the laser beam

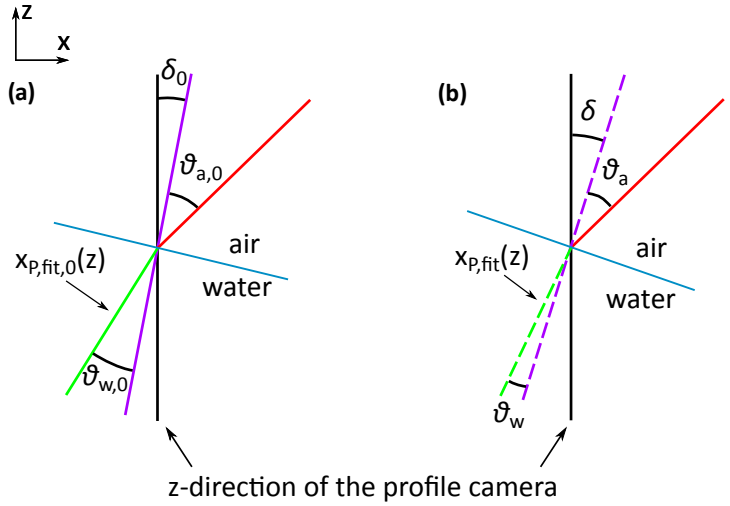

Fig. 7.6: Sketches of the laser beam (red) hitting the water surface when the water is at rest (a) and when the slope of the water surface is changed due to waves (b). The black vertical lines indicate the z-direction in the LIF images of the profile camera. The purple lines are perpendicular to the water surface. The green lines mark the positions of the fluorescence profile $x_{\mathrm{P,fit,0}}$ and $x_{\mathrm{P,fit}}$ for the two cases, which can be used to infer the slope of the water surface as described in the text.

and the camera position are fixed, they are equal and it follows

$$\delta_x = \delta - \delta_0 = \vartheta_{\mathrm{a,0}} - \vartheta_{\mathrm{a}}. \tag{7.4}$$

By using Snell's law in Eq. 7.2, this can be rewritten as

$$\delta_x = \arcsin\left(\frac{n_{\mathrm{w}}}{n_{\mathrm{a}}}\sin(\beta_{\mathrm{0,w}} - \delta_0)\right) - \arcsin\left(\frac{n_{\mathrm{w}}}{n_{\mathrm{a}}}\sin(\beta_{\mathrm{w}} - \delta)\right). \tag{7.5}$$

To obtain an analytical result, small angles implying $\sin(x) \approx x$, $\arcsin(x) \approx x$ are assumed, leading to

$$\delta_x = \frac{\beta_{\mathrm{w}} - \beta_{\mathrm{w,0}}}{1 - n_{\mathrm{a}}/n_{\mathrm{w}}} = 4(\beta_{\mathrm{w}} - \beta_{\mathrm{w,0}}). \tag{7.6}$$

The angles $\beta_{\mathrm{0,w}} - \delta_0$ and $\beta_{\mathrm{w}} - \delta$ are expected to be small, as only a moderate wind speed was used for the measurements. If they do not exceed 20 °, the error of δ_x should stay below 3 %. The uncertainty of the slope of the fluorescence profile a_{P} can be neglected here.

7.2.2 Intensity analysis

A high gray value in the image in Fig. 7.5 (a) corresponds to a high concentration of the alkaline pyranine component $[\mathrm{I}^-]$ related to a high amount of ammonia entering

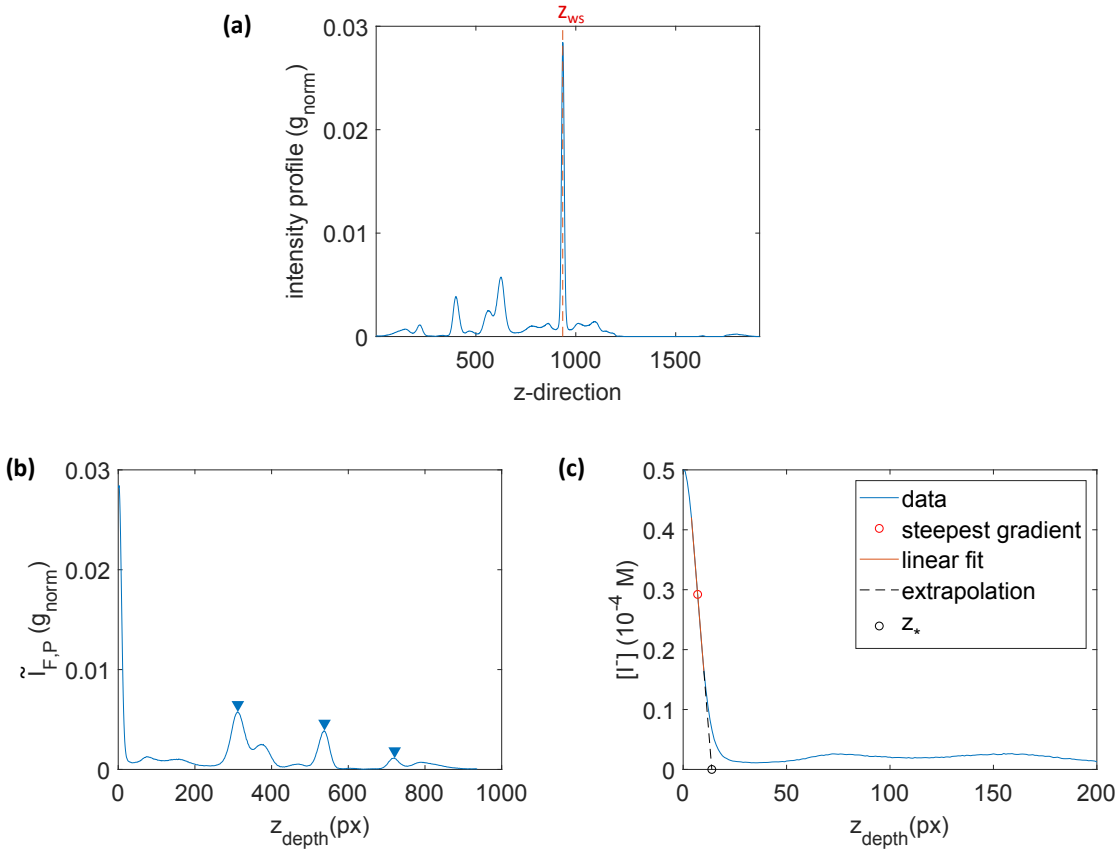

Fig. 7.7: (a) Intensity profile determined as the column-wise mean of the image in Fig. 7.5 (a). The height of the water surface z_{ws} is indicated by the red line. (b) Fluorescence profile of (a), where peaks corresponding to detachments are marked. (c) Concentration profile of (b) up to 200 px. The linear fit applied to data points around the steepest gradient yields the boundary layer thickness z_* by extrapolation.

the water at the moment of recording. As described in Sec. 5.5.2, the intensity profile is determined as the column-wise mean of an image (see Fig. 7.7 (a)). The relevant fluorescence profile $\tilde{I}_{\mathrm{F,P}}(z_{\mathrm{depth}})$ (see Fig. 7.7 (b)) includes only the values up to the water surface height z_{ws} determined from the geometric analysis. This extracted fluorescence profile reveals the mass boundary layer, visible as the steep intensity decrease close to the water surface, as well as peaks at larger depths. These represent detachments from the boundary layer in the form of packages of fluorescent indicator molecules traveling to the water bulk. The peaks are identified with an algorithm (*findpeaks* function by *Matlab*) to determine their locations and their number.

To infer a concentration profile $[\mathrm{I}^-](z_{\mathrm{depth}})$ from the fluorescence profile $\tilde{I}_{\mathrm{F,P}}(z_{\mathrm{depth}})$, the proportionality factor from the calibration measurement (see Eq. 5.26) and the simulation (see Sec. 5.6.1) are used. The calculations are performed as for the BLI

setup (see Sec. 7.1.1), the only difference being that the emission wavelength of the laser is used instead of the spectrum of the LEDs. The simulated fluorescence profiles are shown in Fig. 7.8 for a few depths z_{depth} as a function of $[\mathrm{I}^-]$. A value $\tilde{I}_0(z_{\mathrm{depth}})$ of a measured fluorescence profile is converted to $\tilde{I}_{0,\mathrm{sim}}(z_{\mathrm{depth}}) = \tilde{I}_0(z_{\mathrm{depth}})/\sigma_{\mathrm{P}}$. With the resulting value, the corresponding concentration $[\mathrm{I}^-]_0(z_{\mathrm{depth}})$ is found by interpolation of the calculated curve corresponding to the depth z_{depth}.

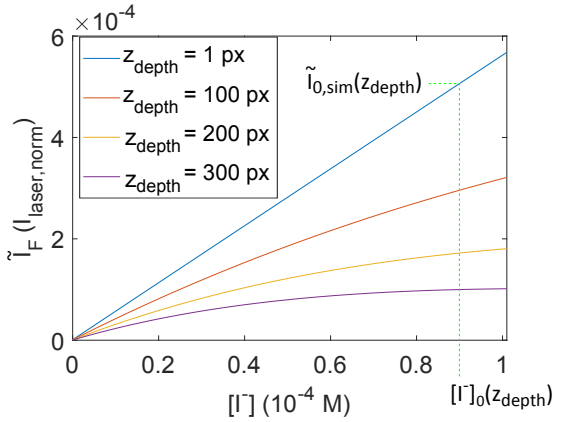

Fig. 7.8: Simulation data of the fluorescence profile $\tilde{I}_{\mathrm{F}}$ as a function of $[\mathrm{I}^-]$ for several discrete depths z_{depth}. The value $\tilde{I}_{0,\mathrm{sim}}(z_{\mathrm{depth}})$ is obtained from the measured fluorescence profile and used to infer the concentration value $[\mathrm{I}^-]_0(z_{\mathrm{depth}})$ by interpolation of the calculated curve corresponding to the depth z_{depth}.

Due to the flattening of the calculated curves with increasing depth, a small uncertainty of the input value $\tilde{I}_{0,\mathrm{sim}}(z_{\mathrm{depth}})$ leads to a large error of the determined concentration value. Therefore, concentrations are only determined for depths $z_{\mathrm{depth}} \leq 200\,\mathrm{px}$, where this effect was found to be not dominant. Figure 7.7 (c) shows the concentration profile determined from the fluorescence profile in Fig. 7.7 (b).

As described in Sec. 2.2.2, the water-side mass boundary layer thickness z_* can be found by extrapolating the tangent of the concentration profile at the water surface down to the bulk concentration. Since the flattening of the measured fluorescence profile at the water surface due to the point spread function of the optics [Jähne, 2012] is carried over to the concentration profile, determining the tangent directly, is not reasonable. Still, an approximation can be found by applying a linear fit to the concentration profile around the point with the steepest gradient. For this, data points are chosen symmetrically around the global minimum of the first derivative calculated numerically. The slope of the fitted line is an estimate for the gradient $\frac{\partial c}{\partial z}\big|_{z=0}$ occurring in Fick's first law (Eq. 2.32). Extrapolating the line to zero, yields z_* (see Fig. 7.7 (c)).

8. Experimental results and discussion

In this chapter, the results of the invasion experiments with ammonia conducted at the Heidelberg linear wind-wave tunnel are presented. The experiments with short ammonia injections and with constant ammonia flux into the water are addressed in turn.

8.1 Results of the experiments with short gas injection

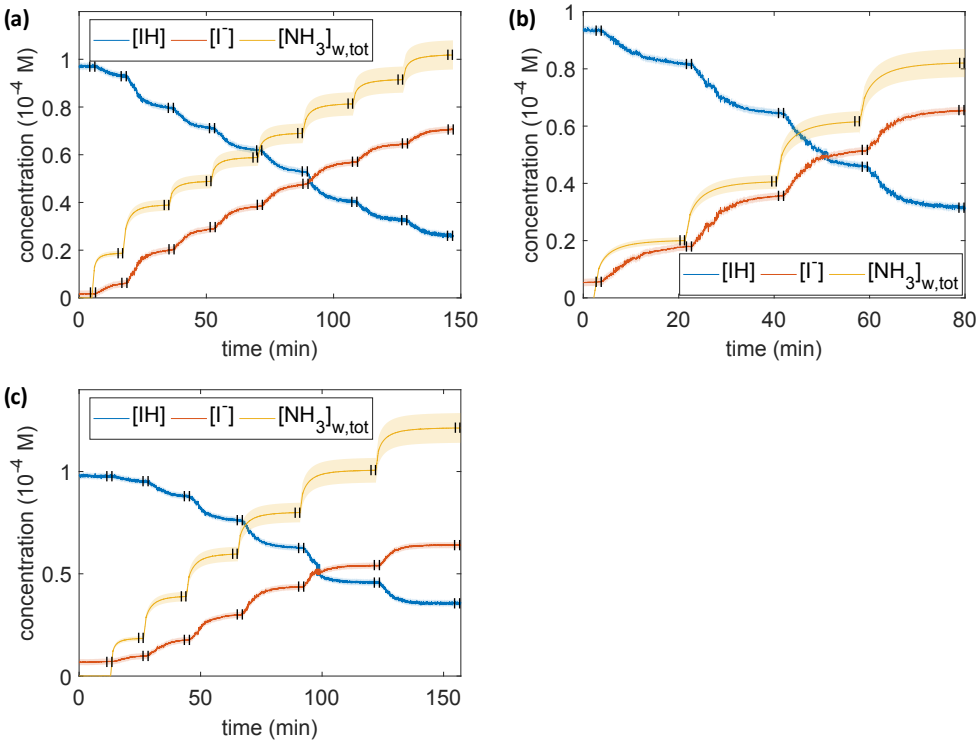

Fig. 8.1: (a)-(c): Temporal evolution of the water-side ammonia concentration $[NH_3]_{w,tot}$ and the concentrations of the pyranine components [IH] and $[I^-]$ for the three measurement series conducted with short ammonia injections (see Tab. 6.1). The shaded areas indicate the respective uncertainties. The black vertical lines indicate the time intervals in which the concentrations were assumed to be equilibrated.

The evaluation of the experiments with short ammonia injections (see Sec. 6.1) focuses on the verification of the linear relationship between the water-side concentration

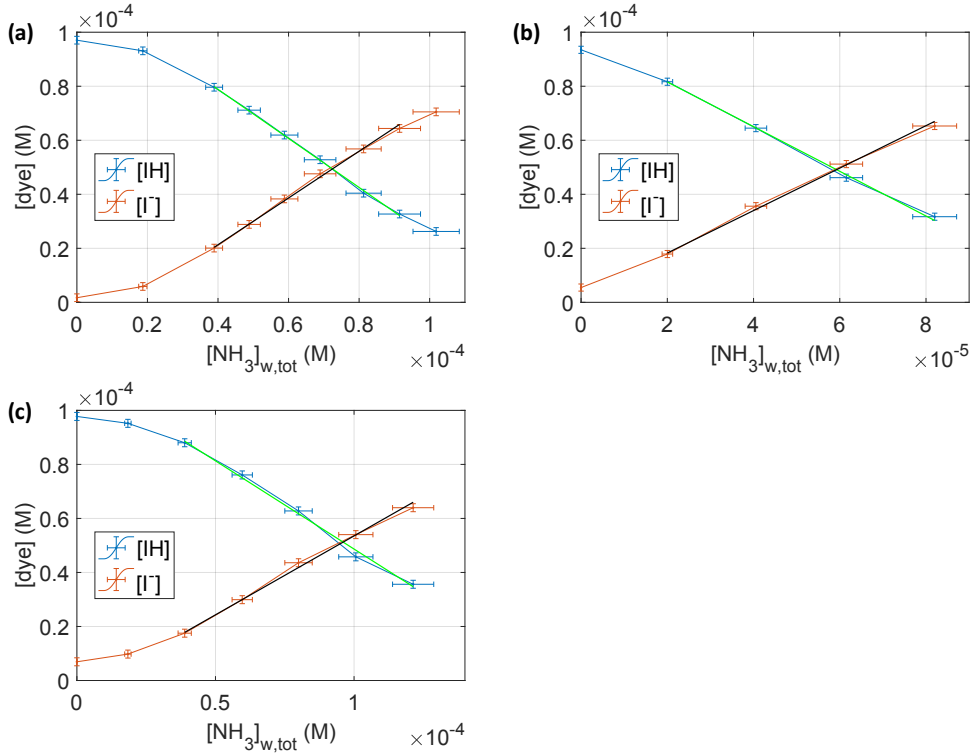

Fig. 8.2: (a)-(c): Concentrations of the pyranine components [IH] and [I$^-$] versus the water-side ammonia concentration $[NH_3]_{w,tot}$ for the three measurement series (see Tab. 6.1). The shown values are the averages after each equilibration. The linear fits depicted in green and black yield the proportionality factor a_{NH3,I^-}.

of ammonia and the concentration of the alkaline pyranine component given in Eq. 3.5. Starting point are the concentration data as shown in Fig. 6.1 (a) and (b), where the water-side ammonia concentration is determined as

$$[NH_3]_{w,tot} = \frac{V_{NH3,input,cum}/V_M - [NH_3]_a V_a}{V_w}, \tag{8.1}$$

with the molar volume V_M and the air and water volumes of the tunnel V_a and V_w. Figure 8.1 shows the temporal evolution of the concentration values $[NH_3]_{w,tot}$, [IH] and [I$^-$] for the three measurement series that were conducted. The time intervals in which equilibration after a gas injection (cf. 6.1) was assumed are marked by black lines. The intervals were chosen such that the concentration values in each interval do not change by more than 10^{-6} M, which corresponds to the error estimate for the values determined with the transmission probe. The values in each interval are averaged. The average values of [IH] and [I$^-$] are plotted against the average values of $[NH_3]_{w,tot}$ in Fig. 8.2. The data reveal the linear regime around the equivalence point of pyranine as expected. In analogy to the evaluation in Sec. 5.6.2, a linear fit

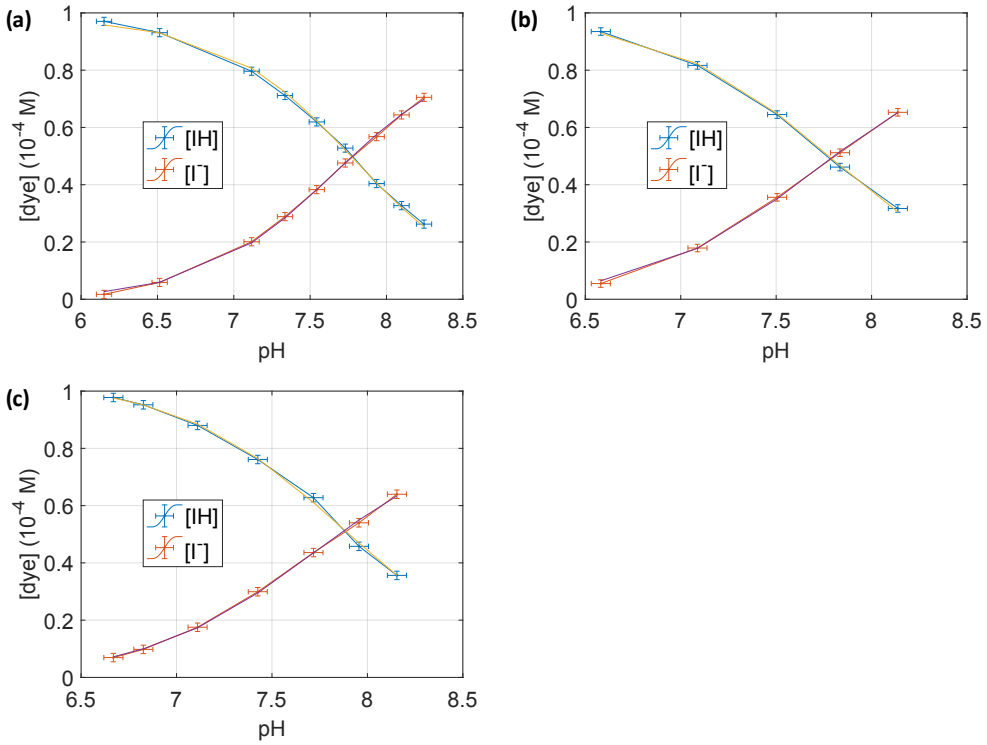

Fig. 8.3: Concentrations of the pyranine components [IH] and [I$^-$] versus the pH value for the three measurement series conducted with short ammonia injections (see Tab. 6.1). The shown values are the averages after each equilibration. The fits depicted in yellow and purple yield the pK_a value of pyranine.

is applied for each series to the [IH] and [I$^-$] data as a function of $[NH_3]_{w,tot}$. The two resulting proportionality factors are averaged and their difference is taken as an error estimate. Furthermore, the concentrations of the pyranine components are plotted versus the measured pH values that are correspondingly averaged (see Fig. 8.3). With these data, the dissociation constant of pyranine is determined in analogy to the evaluation in Sec. 5.1.1.

The results for the proportionality factor a_{NH3,I^-} and the pK_a value are shown in Fig. 8.4 as a function of the initial conductivity κ_{start} at the beginning of each measurement series, which serves as a measure of the ion concentration in the water. Due to the subsequent invasion experiments, the conductivity increased from series no. 1 to 3 (see Tab. 6.1). The values of the proportionality factor a_{NH3,I^-} for the first two series are in good agreement with the calculated value in Eq. 3.15. For the last series, a_{NH3,I^-} drops significantly. It could be expected that this is caused by a change of the pK_a value due to the increase of the ion concentration. However, the measured pK_a values (see Fig. 8.4 (b)) stay constant within the scope of their

uncertainties, which contradicts this explanation. The values are also in good agreement with the reference value measured at a lower ion concentration (see Eq. 5.4). Another possible explanation for the change of $a_{\mathrm{NH3,I^-}}$ is a distorted mass balance. Since the tunnel stayed closed in between the subsequent measurements, more and more condensed water vapor could accumulate at the inside of the tunnel walls, where ammonia could dissolve. This could reduce the amount of ammonia that entered the actual water segment. Because only the total reduction of the air-side ammonia concentration was measured, the amount of ammonia assumed for the mass balance could be overestimated, leading to an apparently lower proportionality factor. This explanation is supported by the fact that the measured relative air humidity was always close to 100 % (see Tab. 6.1). The effect is considered to be favored in the used wind-wave tunnel because the area of the walls $A_{\mathrm{walls}} \sim 20\,\mathrm{m}^2$ is significantly larger than the water surface area $A_{\mathrm{ws}} = 1.38\,\mathrm{m}^2$. Probably, the cooling of the water segment which provided a temperature difference of around 2 °C (see Tab. 6.1) and the flushing of the air space with dry air in between the measurements were not sufficient to compensate this effect.

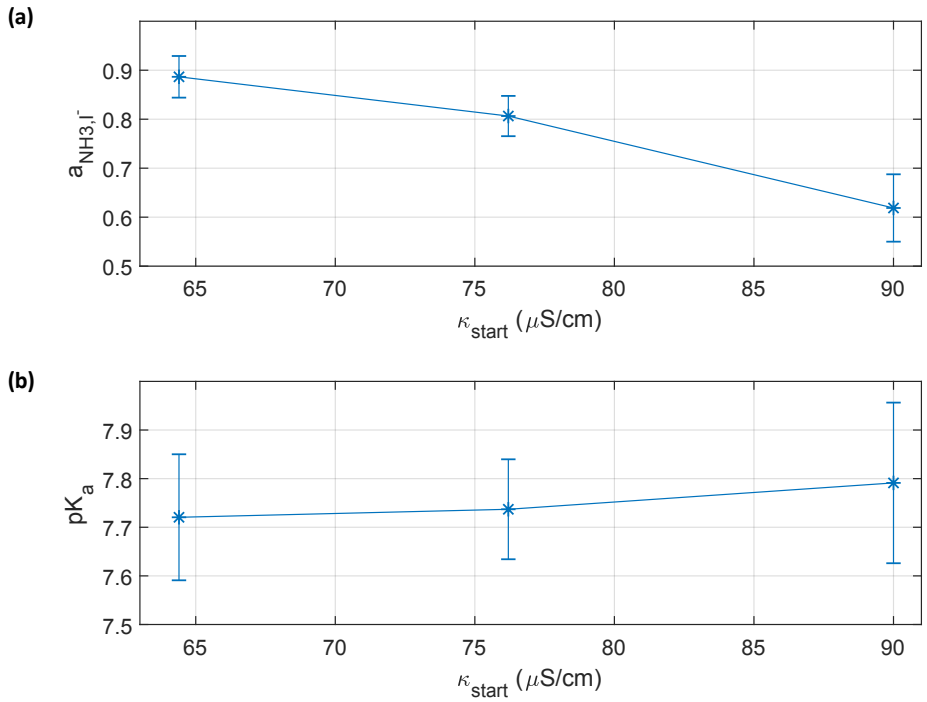

Fig. 8.4: Proportionality factor $a_{\mathrm{NH3,I^-}}$ (a) and $\mathrm{pK_a}$ value of pyranine (b) as a function of the conductivity κ_{start} at the beginning of a measurement series. The conductivity increased from series no. 1 to 3 (see Tab. 6.1)

8.2 Results of the experiments with constant gas flux

Main goal of the evaluation of the constant flux measurements is to verify that the water-side flux of the alkaline pyranine component is proportional to the air-side flux of ammonia (see Eq. 3.6). The presentation of results is divided into three parts. In the first two parts, the BLI and the LIF results are discussed. In each section, the temporal evolution of relevant parameters and the dependency of their temporal averages on the air-side flux are addressed in turn. Using the results of the BLI setup, it is shown how the water-side flux of I^- is determined. Moreover, it is shown how local concentration changes of dissolved ammonia are estimated. In the third part, exemplary results of the stereo imaging realized with the bottom BLI cameras are shown and discussed with regard to results of the LIF imaging.

8.2.1 BLI

Temporal evolution

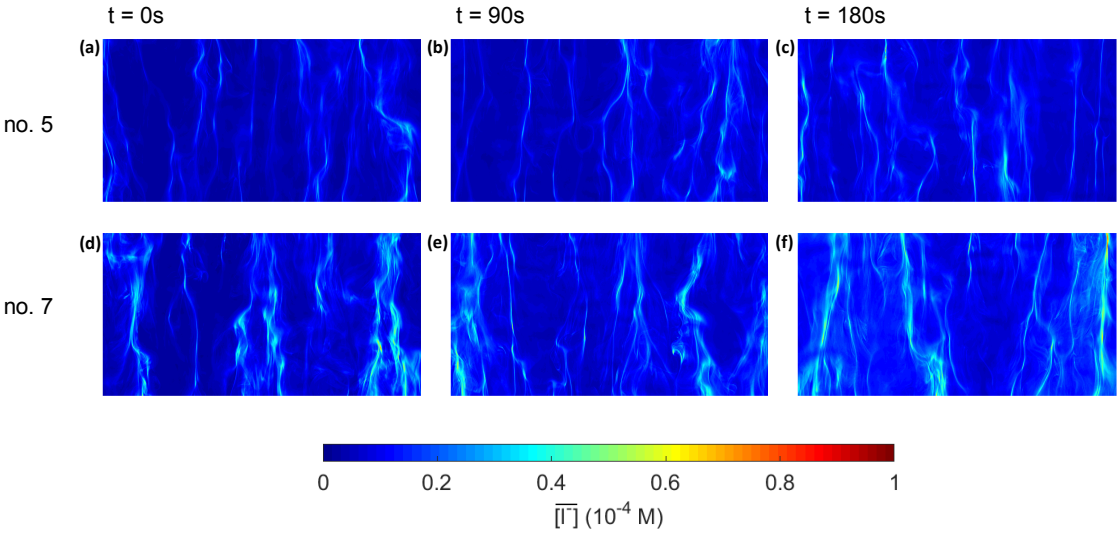

Fig. 8.5: BLI images recorded by the top camera (B4) at times $t = 0\,\mathrm{s}$, $t = 90\,\mathrm{s}$ and $t = 180\,\mathrm{s}$ since the beginning of the image acquisition for two different measurements at constant air-side ammonia flux (see Tab. 6.2). The flux in measurement no. 5 ((a)-(c)) was lower than in no. 7 ((d)-(f)).

The results of the BLI images will be discussed exemplarily for data recorded by the top camera (B4) in the measurements no. 5 and 7 (see Tab. 6.2). Figure 8.5 shows concentration images for times $t = 0\,\mathrm{s}$, $t = 90\,\mathrm{s}$ and $t = 180\,\mathrm{s}$ since the start of the

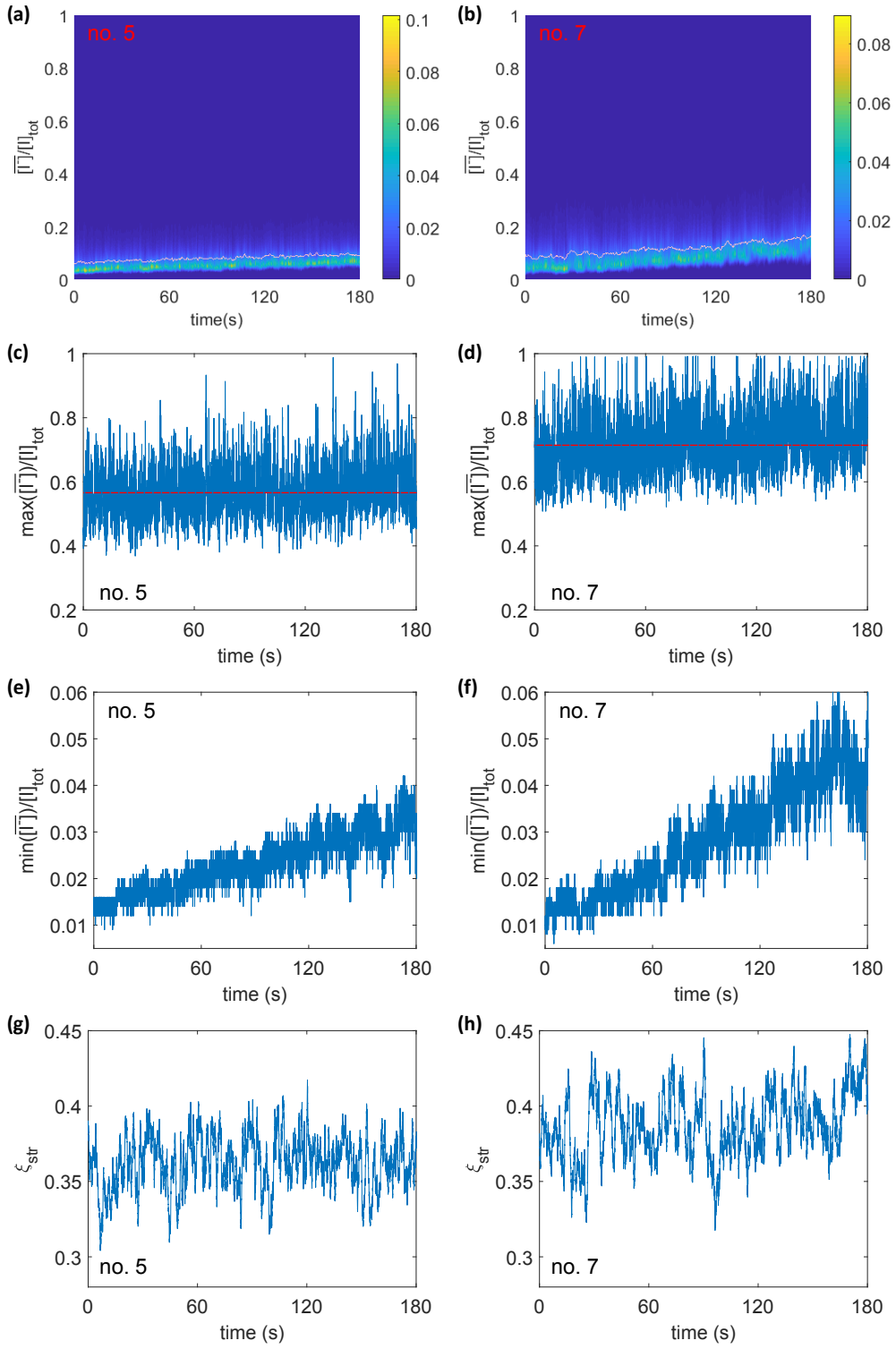

Fig. 8.6: Temporal overview of the data extracted from the BLI images recorded by the top camera (B4) in the measurements no. 5 and 7 (see Tab. 6.2). (a)-(b): Histograms of the concentration data $\overline{[I^-]}$ normalized to the total indicator concentration $[I]_{tot}$. The counts illustrated by the color are normalized to the total number of pixels. The pink curve indicates the mean values of the distributions. Minimum values $\min(\overline{[I^-]})$ ((c)-(d)) and maximum values $\max(\overline{[I^-]})$ ((e)-(f)) of the histograms. The temporal averages of $\max(\overline{[I^-]})$ are marked by red lines. (g)-(h): Streak coverage ξ_{str}.

image acquisition. The data is obtained from the gray scale images as described in Sec. 7.1.1. It is evident that brighter streaks occur if the ammonia flux is higher. The background signal increases with time because of the increasing bulk fluorescence.

The temporal change of the $\overline{[\mathrm{I}^-]}$ data is shown in Fig. 8.6 (a)-(d). Each column in the color plots in (a) and (b) represents a histogram of $\overline{[\mathrm{I}^-]}$ data of a concentration image. The diagrams reveal the increase of the modal value and the mean value of the distributions with time as well as the positive skewness. The minimum and the maximum values of the histograms are illustrated in (c)-(f). While the minimum $\min(\overline{[\mathrm{I}^-]})$ increases with time, the maximum $\max(\overline{[\mathrm{I}^-]})$, which corresponds to the brightest streaks in an image, scatter around a rather constant average value. Similarly, the streak coverage ξ_{str}, that is defined in Sec. 7.1.2 and illustrated in (g) and (h), shows no clear trend. Since these two parameters are a measure of the ammonia uptake and show no distinct temporal trend, the flux dependency of their temporal averages $\langle\max(\overline{[\mathrm{I}^-]})\rangle_t$ and $\langle\xi_{\mathrm{str}}\rangle_t$ will be examined in Sec. 8.2.1.

Figure 8.7 illustrates how the air-side flux of ammonia and the water-side flux of the alkaline pyranine component are determined. For the air side, the concentration data $[\mathrm{NH_3}]_{\mathrm{a}}(t)$ recorded with the UV spectroscopy setup and the corrected input flow rates, yielding the input volume $V_{\mathrm{NH3,input}}(t)$, are used to determine the water-side volume $V_{\mathrm{NH3,w,tot}}(t) = V_{\mathrm{NH3,input}}(t) - [\mathrm{NH_3}]_{\mathrm{a}}(t)V_{\mathrm{a}}/V_{\mathrm{M}}$. The volume of the air space and the molar volume are denoted by V_{a} and V_{M}, respectively. Neglecting the leakage term, the mass balance in Eq. 3.19 can be then rewritten as

$$j_{\mathrm{a,NH3}} = \frac{\dot{V}_{\mathrm{NH3,w,tot}}(t)/V_{\mathrm{M}}}{A_{\mathrm{ws}}}, \tag{8.2}$$

where A_{ws} denotes the area of the water surface in the water segment. The amount of ammonia that enters the water per time $\dot{V}_{\mathrm{NH3,w,tot}}(t)$ is determined as the slope of the line fitted to the data $V_{\mathrm{NH3,w,tot}}(t)$ as a function of time (see Fig. 8.7 (a)-(b)).

For the water side, the temporal evolution of the concentration data $\overline{[\mathrm{I}^-]}$ from the recorded BLI images is used. The average of each concentration image $\mathrm{avg}(\overline{[\mathrm{I}^-]})$ is assumed as the most representative measure. Due to the approximately constant ammonia flux, $\mathrm{avg}(\overline{[\mathrm{I}^-]})$ increases linearly. Thus, the temporal change $\frac{\mathrm{d}\,\mathrm{avg}(\overline{[\mathrm{I}^-]}}{\mathrm{d}t}$ can be determined as the slope of a linear fit (see Fig. 8.7 (c)-(d)) and used to infer the water-side flux $j_{\mathrm{w,I^-}}$ by

$$j_{\mathrm{w,I^-}} = \frac{\mathrm{d}\,\mathrm{avg}(\overline{[\mathrm{I}^-]})}{\mathrm{d}t} z_{\mathrm{ws},0}, \tag{8.3}$$

where for the length of the water column the mean water level $z_{\mathrm{ws},0} = 9.2\,\mathrm{cm}$ is assumed. The average streak signal $(\mathrm{avg}(\overline{[\mathrm{I}^-]}_{\mathrm{str}}))$ and the average background signal $(\mathrm{avg}(\overline{[\mathrm{I}^-]}_{\mathrm{bg}}))$, that are obtained from the segmentation described in Sec. 7.1.2, show a similar temporal evolution (see Fig. 8.7 (c)-(d)).

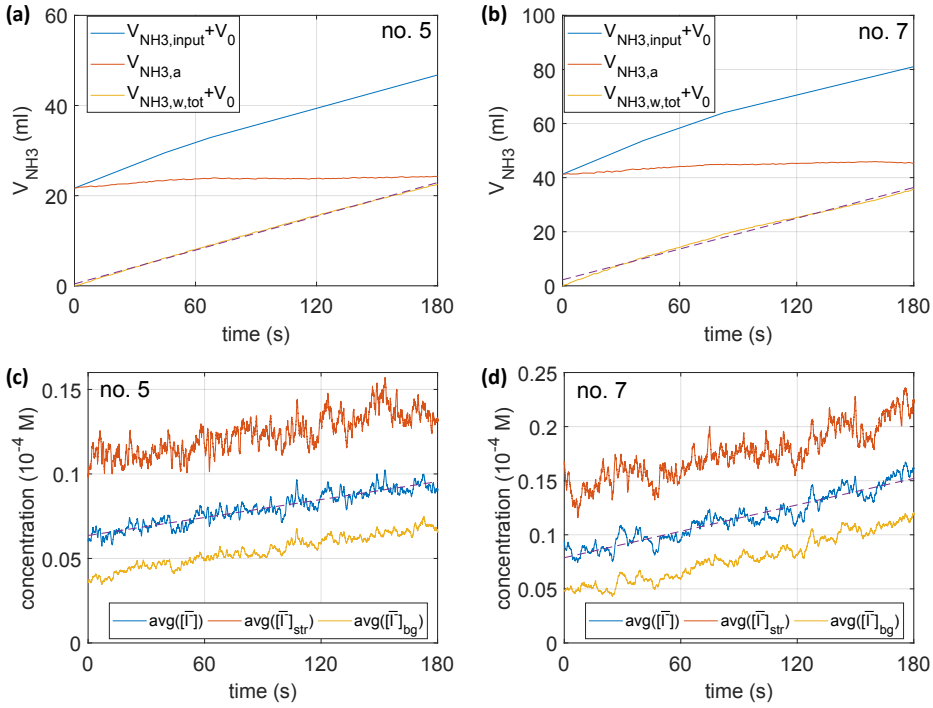

Fig. 8.7: Determination of the air-side and water-side fluxes for measurement no. 5 and 7 (see Tab. 6.2). (a)-(b): Volume of input, air- and water-side ammonia, where V_0 is an offset that accounts for the amount of ammonia that has already entered the water. The change of $V_{\mathrm{NH3,w,tot}}$ with time is determined with a linear fit depicted as a dashed line. (c)-(d): Average of all values in a concentration image (avg($\overline{[\mathrm{I}^-]}$)) as well as the averages of the separated streak (avg($\overline{[\mathrm{I}^-]}_{\mathrm{str}}$)) and background signals (avg($\overline{[\mathrm{I}^-]}_{\mathrm{bg}}$)) as a function of time. The temporal change of avg($\overline{[\mathrm{I}^-]}$) is determined with a linear fit, that is depicted by a dashed line.

Flux dependency

Figure 8.8 gives an overview of the concentration images for the different ammonia fluxes recorded by the top camera (B4) at the beginning of the image acquisition. With increasing flux, the dynamic range of the concentration data increases significantly. Higher concentrations occur in the streak regions and the streak coverage increases as well. The contrast of the streaks in the image of measurement no. 8 is lower because of a higher initial pH value (see. Tab. 6.2).

The flux dependency of four relevant extracted parameters is summarized in Fig. 8.9. The steady-state concentration $[\mathrm{NH_3}]_{\mathrm{a,ss}}$ in (a) shows an approximately linear dependency. As the air-side ammonia concentration is directly measured during an

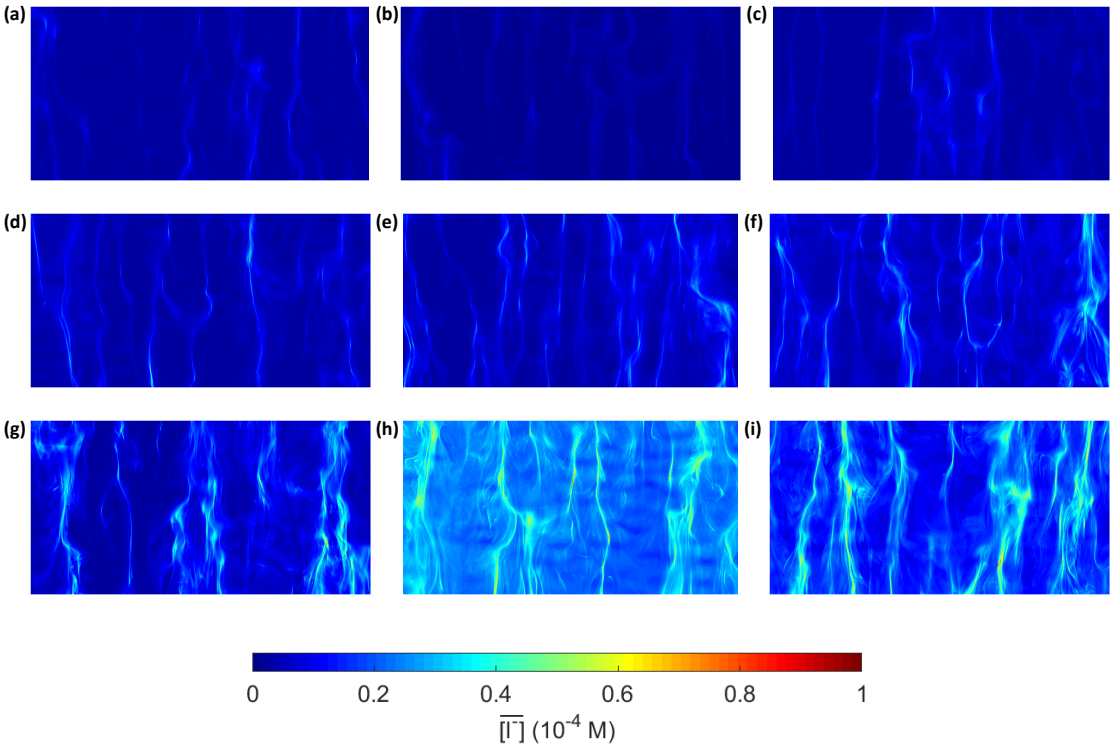

Fig. 8.8: Overview of the concentration images for the measurements no. 1 to 9 with different constant ammonia fluxes into the water (see. Tab. 6.2), recorded by the top camera (B4) at the beginning of the image acquisition. The flux increases from (a) to (i).

experiment, the applied linear fit can be used as a calibration line for future experiments at this wind-wave tunnel and with the used wind speed to set a certain flux.

The water-side flux $j_{\mathrm{w,I^-}}$ of the alkaline pyranine component in Fig. 8.9 (b) determined from the BLI images increases with the air-side ammonia flux as expected from the considerations presented in Sec. 3.1. The data of measurement no. 8 correspond to the outliers in the plot, which are marked by the plus symbols. This is presumably related to the too high initial pH of this measurement. To obtain the proportionality factor $a_{\mathrm{NH3,I^-}}$ in Eq. 3.6, linear fits are applied to the data sets of the BLI cameras B1, B2, B3 and B4, excluding measurement no. 8. The results with the respective uncertainties obtained from the fits are

$$a^{\mathrm{B1}}_{\mathrm{NH3,I^-}} = 0.76 \pm 0.04, \tag{8.4a}$$
$$a^{\mathrm{B2}}_{\mathrm{NH3,I^-}} = 0.74 \pm 0.03, \tag{8.4b}$$
$$a^{\mathrm{B3}}_{\mathrm{NH3,I^-}} = 0.77 \pm 0.04, \tag{8.4c}$$
$$a^{\mathrm{B4}}_{\mathrm{NH3,I^-}} = 0.68 \pm 0.03. \tag{8.4d}$$

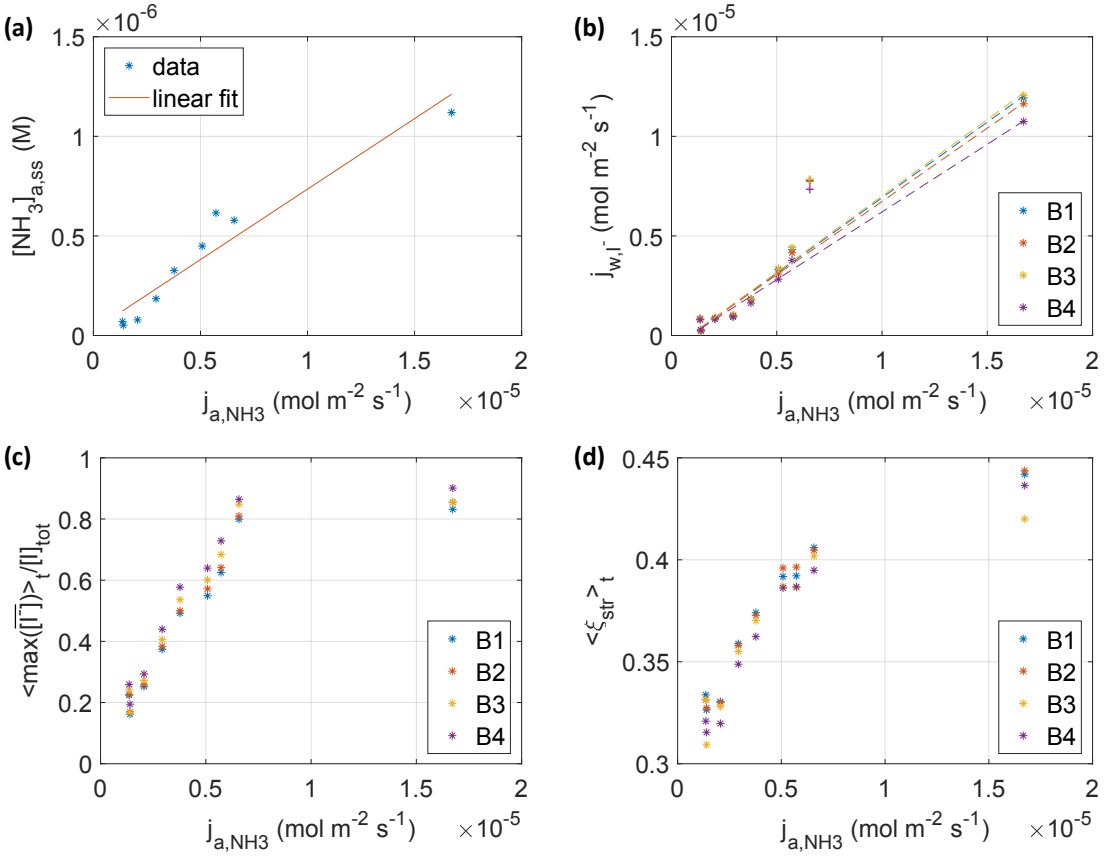

Fig. 8.9: (a) Steady-state ammonia concentration $[NH_3]_{a,ss}$, (b) water-side flux of the alkaline pyranine component j_{w,I^-}, (c) temporal average of the maximum concentration values $\langle \max(\overline{[I^-]}) \rangle_t$ and (d) temporal average of the streak coverage $\langle \xi_{str} \rangle_t$ as a function of the air-side ammonia flux $j_{a,NH3}$. The diagrams (b)-(d) show the results for the BLI cameras B1, B2, B3, B4.

While the results for the bottom cameras (B1,B2,B3) are almost identical, the result for the top camera (B4) exhibits a deviation from them, which could be related to optical effects due to the presence of waves. Overall, the data confirm the linear relationship formulated in Eq. 3.6. The found proportionality factors are at least close to the theoretical estimation in Eq. 3.15. The deviation could be caused by the fact that this estimate assumes a perfect steady-state flux and completely ignores the dynamics of the gas exchange process. The comparison with the results from the short gas injections (see Fig. 8.4 (a)) shows that the values are in a similar range.

As mentioned in Sec. 8.2.1, the temporal average value of the highest concentrations $\langle \max(\overline{[I^-]}) \rangle_t$ in the concentration images represent a measure of the brightest streaks occurring during an experiment. Thus, their behavior as a function of the ammonia flux can be studied to examine the saturation of the indicator (see Sec. 3.3). It is

expected that if the flux is high enough, the maximum concentration values level off. Figure 8.9 (c) confirms this consideration. The parameter $\langle \max(\overline{[I^-]}) \rangle_t$ increases nearly linearly with the flux up to measurement no. 8 and levels off at values around $0.85{\cdot}10^{-4}$ M. The saturation occurs at a flux of $j_{a,NH3} \simeq 6.6{\cdot}10^{-6}$ M which corresponds to a steady-state concentration of $[NH_3]_{a,ss} \simeq 0.6 \cdot 10^{-6}$ M. This value is in the same order of magnitude as the rough approximation in Eq. 6.3. For higher ammonia fluxes, it is expected that the indicator becomes more and more saturated such that the supply of IH molecules from the water bulk is not sufficient to protonate dissolved ammonia immediately at the water surface. As a consequence, the proportionality between the concentrations of the pyranine components and dissolved ammonia will not hold anymore. In accordance with these considerations, the temporal average of the streak coverage $\langle \xi_{str} \rangle_t$ shown in Fig. 8.9 (d) shows the tendency to saturate for higher fluxes.

Determination of water-side ammonia concentrations

The proportionality between the air-side flux of ammonia and the water-side flux of the alkaline pyranine component I^- is confirmed by image data shown in the last section. Using Eq. 3.16, this implies that a change of the water-side ammonia concentration $\overline{[NH_3]}_{w,tot}$, averaged along the water column, can be determined from the concentration images showing the local distribution of $\overline{[I^-]}$. Considering one of the measurements with constant ammonia flux (see Tab. 6.2), a certain concentration of dissolved ammonia $[NH_3]_{w,tot}$ is possibly already present from a previous measurement.

During the adjustment of the ammonia flux, the water-side ammonia concentration increases locally at the water surface. Also in the water bulk, the concentration of dissolved ammonia and the alkaline pyranine component may change. The values of these bulk concentrations $[NH_3]_{w,tot,start}$ and $[I^-]_{start}$ at the beginning of the image recording are considered as the initial concentrations in Eq. 3.16. The value of $[I^-]_{start}$ is measured with the transmission probe. Assuming the proportionality factors in Eq. 8.4, the change $\Delta\overline{[NH_3]}_{w,tot}$ relative to $[NH_3]_{w,tot,start}$ can be obtained for each pixel in the concentration images. Figure 8.10 shows two examples of the resulting images for the top camera (B4). Because of the discrepancy between the factors in Eq. 8.4, an error of 10 % is assumed. Despite the large uncertainty, the developed method provides a first approach to obtain quantitative information on the local concentration changes of a gas in the water-side mass boundary layer with a horizontal resolution.

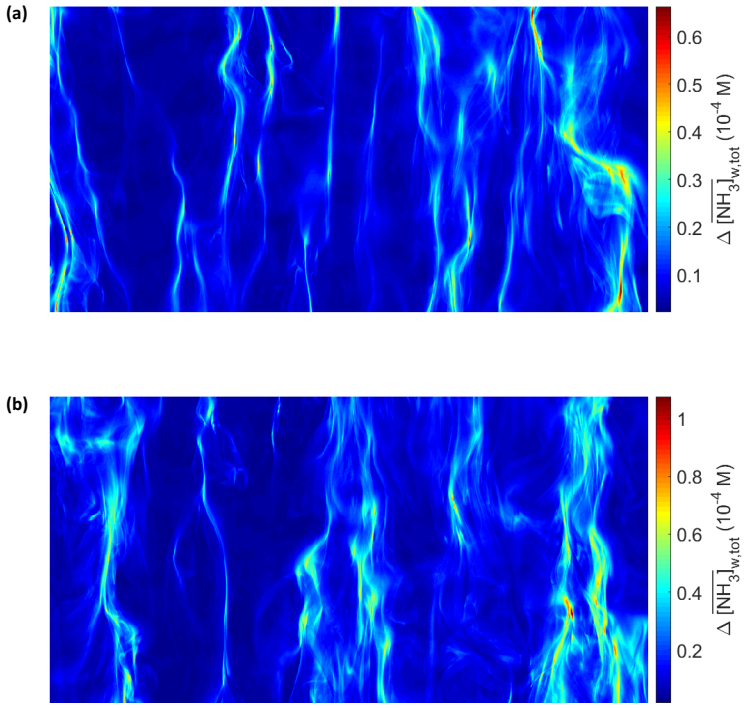

Fig. 8.10: Example images showing the change of the ammonia concentration averaged along the water column $\Delta\overline{[\mathrm{NH_3}]}_{\mathrm{w,tot}}$, that is obtained from the images recorded by the top BLI camera (B4) for two different measurements at constant air-side ammonia flux (see Tab. 6.2). The flux in measurement no. 5 (a) was lower than in no. 7 (b).

8.2.2 LIF

Temporal evolution

For the discussion of the LIF results, data of measurement no. 7 (see Tab. 6.2) are presented exemplarily. Due to the high temporal variability of the data, distinct features can not be presented adequately if a whole data set comprising 180 s of recording is shown. Therefore, only short time intervals are chosen.

Figure 8.11 (a)-(b) shows the extracted fluorescence and concentration profiles (cf. Sec. 7.2.2) as a function of the time and the real world depth z_{depth}, where $z_{\mathrm{depth}} = 0$ corresponds to the current height of the water surface. The highest concentrations of I^- occur close to the water surface. The profiles reveal a repetitive build-up of the boundary layer followed by detachment events that are identified as surface renewal events (cf. Sec. 2.2.4). These events can also be read off from the gradual increase and the sudden drop of the determined boundary layer thickness z_* in Fig. 8.11 (c).

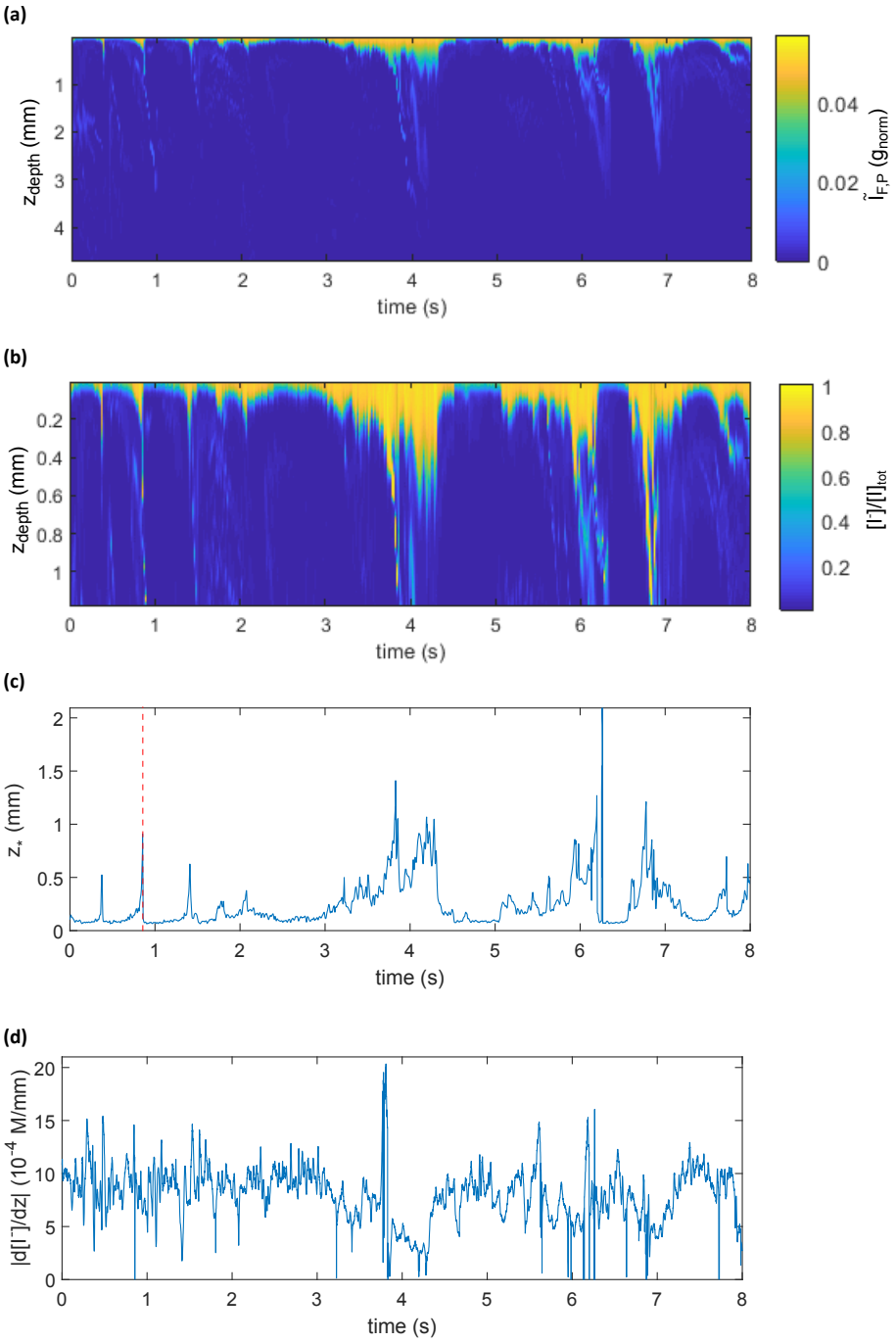

Fig. 8.11: (a)-(b): Color plots of the fluorescence and the concentration profiles $\tilde{I}_{\mathrm{F,P}}$ and $[\mathrm{I}^-]$ as a function of the time and the real world depth z_{depth}. The concentration profiles are normalized by the total concentration $[\mathrm{I}]_{\mathrm{tot}}$. The intensity and the concentration are indicated by the color as shown in the color bar. (c) Boundary layer thickness z_* over time. The red line marks a detachment event. (d) Absolute value of the concentration gradient $|\frac{\mathrm{d}[\mathrm{I}^-]}{\mathrm{d}z}|$ over time. The data are shown for a time interval of measurement no. 7 (see Tab. 6.2).

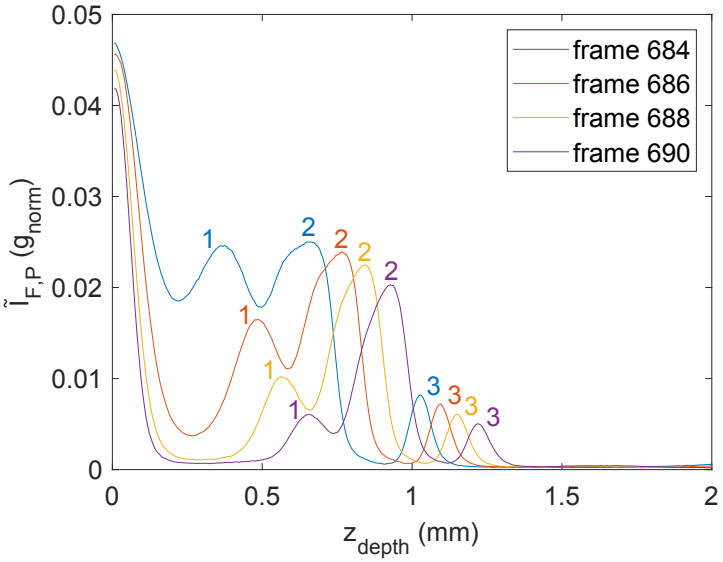

Fig. 8.12: Fluorescence profiles $\tilde{I}_{F,P}$ for every second frame between the frames 684 and 690 of measurement no. 7. The profiles illustrate a detachment event, marked in Fig. 8.11 (c) by the dashed line. Three detachments are indicated, revealing that their position can be tracked as a function of time.

As the concentration of I^- decreases with depth, the gradient $\frac{d[I^-]}{dz}$ is always negative. Its absolute value is shown in Fig. 8.11 (d). The gradient reveals rapid fluctuations and shows no clear trend with time.

Figure 8.12 shows the fluorescence profile at a detachment event that is marked by the dashed line in Fig. 8.11 (c). As the position of the detachment peaks in the single images could already be determined (see Sec. 7.2.2), a tracking of them with time seems feasible.

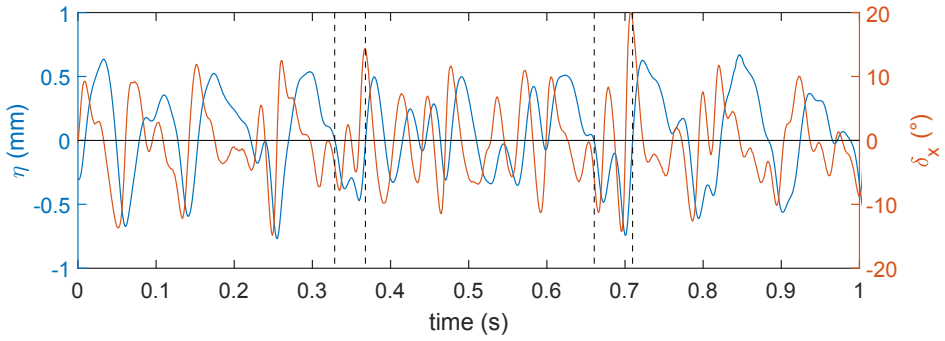

Fig. 8.13: Water surface displacement η and inclination angle in wind direction δ_x in a chosen time interval of measurement no. 7 (see Tab. 6.2). The black dashed lines mark exemplary zeros of η

The displacement η and the inclination angle δ_x of the water surface in wind direction, which are determined as decribed in Sec. 7.2.1, are shown Fig. 8.13. A few zeros of η are marked by dashed lines. At the used wind speed the amplitude of the displacement does not exceed 1 mm, while the inclination typically ranges from $-10\,°$ to $10\,°$. The

rapid oscillations between two zeros of η correspond to capillary waves. The the inclination angle shows the tendency to reach extreme values when the displacement crosses the zero line as it is expected, considering a sine wave. This type of setup could be compared with an established measurement technique like the image slope gauge (see e.g [Kiefhaber et al., 2014]). If the agreement is satisfying, the setup could be used independently as a compact, auxiliary measurement technique to determine the displacement and the inclination of the water surface at a specific spot.

Flux dependency

As the wind speed was the same for all conducted measurements, the level of turbulence and hence the mean of the boundary layer thickness z_* is expected to be constant. In contrast, the concentration gradient is supposed to increase with the air-side ammonia flux. The average boundary layer thickness $\langle z_* \rangle_t$ and the average gradient $\langle \frac{\mathrm{d}[\mathrm{I}^-]}{\mathrm{d}z} \rangle_t$ are determined for the measurements performed at different ammonia fluxes. As a comparison, z_* and $\frac{\mathrm{d}[\mathrm{I}^-]}{\mathrm{d}z}$ are also determined from the temporally averaged concentration profiles $\langle [\mathrm{I}^-] \rangle_t$ (see Fig. 8.14 (b)). These are calculated from averaged fluorescence profiles $\langle \tilde{I}_{\mathrm{F,P}} \rangle_t$ (see Fig. 8.14 (a)) by using the same evaluation steps as for the single images (see Sec. 7.2.2).

The obtained data of the boundary layer thickness is shown in Fig. 8.14 (c). The values seem to increase with the ammonia flux, which is not expected. The data that are determined as temporal averages are significantly higher than the data obtained from the averaged profiles. Since the algorithm finds the position of the steepest gradient in a profile, the boundary layer thickness is determined wrongly if this position is located at a detachment peak at larger depth.

The values of the gradient in Fig. 8.14 (d), determined as temporal averages, increase with the flux as expected. In contrast, the values obtained from the average profiles show no clear dependency. Again, the values from the averaged profiles are lower than the temporal averages.

Because of the inconsistency of the results of the boundary layer thickness and the concentration gradient, the data should be considered as estimates only. Presumably, the used approximation of the concentration gradient at the water surface by the slope of the tangent at the steepest gradient of the profile was not as good as expected.

For each air-side ammonia flux, the depths at which the detachment peaks were detected in the images are averaged, yielding the plot shown in Fig. 8.14 (e). Similarly, the number of peaks found in each image is averaged over an image sequence, which results in the diagram in Fig. 8.14 (f). Both parameters show the tendency to increase with the ammonia flux. This is expected, as a higher flux increases the concentration

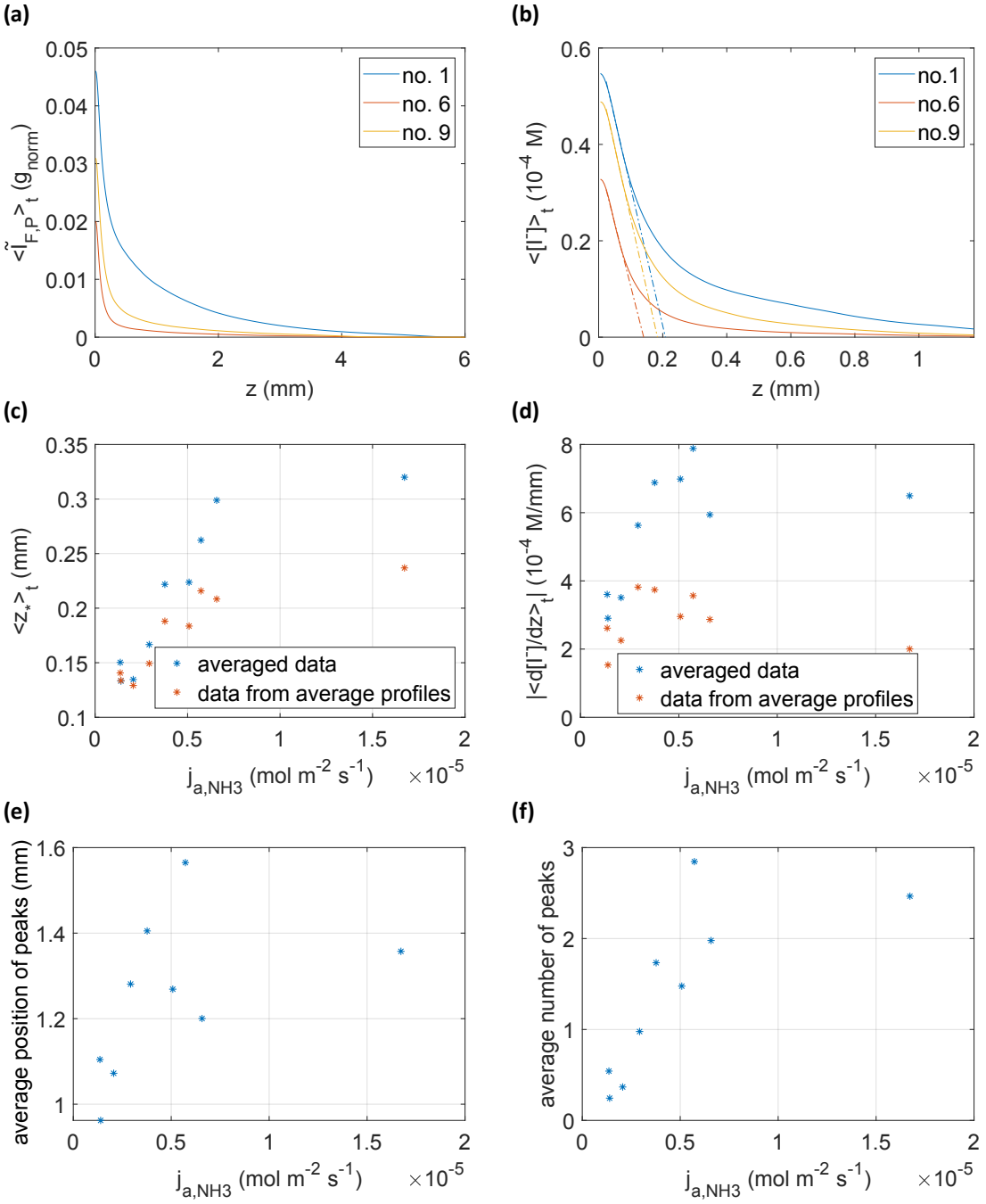

Fig. 8.14: (a)-(b): Temporally averaged fluorescence profile $\langle \tilde{I}_{\mathrm{F,P}} \rangle_t$ and concentration profile $\langle [\mathrm{I}^-] \rangle_t$ for three measurements at constant ammonia flux. (c)-(d): Average boundary layer thickness $\langle z_* \rangle_t$ and absolute value of the average concentration gradient $|\langle \frac{\mathrm{d}[\mathrm{I}^-]}{\mathrm{d}z} \rangle_t|$ as a function of the air-side ammonia flux $j_{\mathrm{a,NH3}}$. The data in blue are determined as temporal averages, while the data in red are obtained from the average concentration profiles. (e)-(f): Temporally averaged depth position and number of the detachment peaks as a function of the flux $j_{\mathrm{a,NH3}}$.

of fluorescent I^- molecules close to the water surface, which improves the visibility of the detachments at larger depths.

8.2.3 Stereo imaging

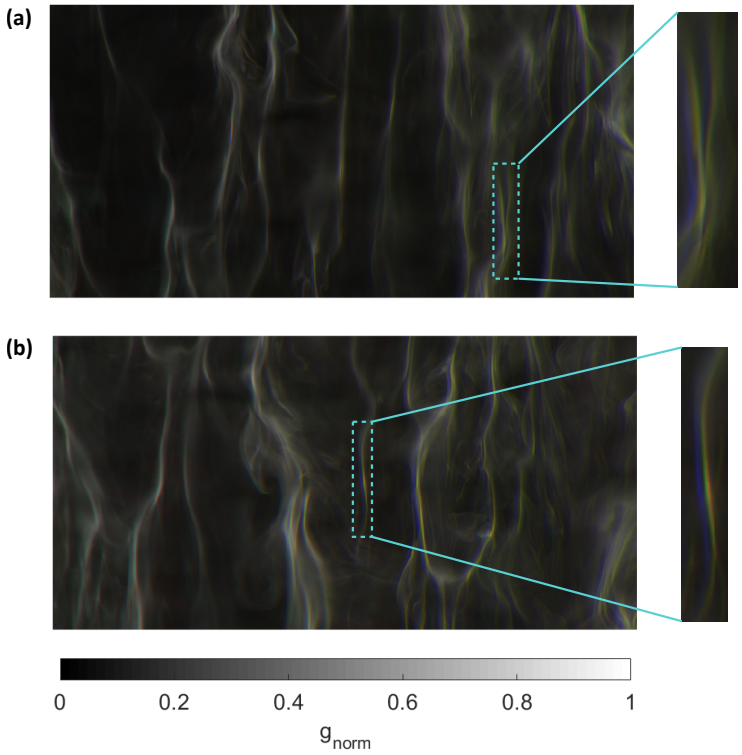

Fig. 8.15: (a)-(b): Exemplary RGB images resulting from a matching of the images recorded by the bottom BLI cameras, where B1, B2 and B3 are assigned to the red, blue and green channel, respectively. The displayed intensity values of each channel correspond to the normalized values g_{norm}. The magnified structures, which are visible three times due to the parallax between the cameras, are located at a different vertical position than the standard water level $z_{\mathrm{ws},0} = 9.2\,\mathrm{cm}$.

To demonstrate for exemplary data that the images recorded by bottom BLI cameras contain depth information, their images are combined to RGB images (see Fig. 8.15). For this, the images of B1, B2 and B3 are assigned to the red, blue and green channel and matched such that the parallax at the standard water level $z_{\mathrm{ws},0} = 9.2\,\mathrm{cm}$ vanishes (cf. Sec. 5.5.1). As a consequence, streaks that are close to the position of the resting water surface appear as gray structures. If structures are located at a different vertical position, they are visible three times in the colors of the three channels with a relative displacement corresponding to the parallax. In the shown

images, such structures are marked. The parallax is typically 2 px. Using the results of the calibration measurement for the stereo pairs (B1,B2) and (B2,B3) (see Eq. 5.14), this corresponds to a vertical displacement of about 3 mm with respect to the standard water level. If the wave field is known, displacements caused by the waves can be excluded. With the calibration measurement described in Sec. 5.5.1, the spatial information that is contained in the BLI images can be used in a future review to attempt a three-dimensional reconstruction of the fluorescent structures.

Structures that are not located directly at the water surface could correspond to the detachments that were also observed with the LIF setup. Therefore, the data of the fluorescence profiles can be used to estimate the necessary depth resolution. According to the averaged data in Fig. 8.14 (e), most detachments are visible at depths between 1 mm and 1.6 mm. It is concluded that a depth resolution of around 10 px/mm would be required for a stereo- or multi-view geometry to resolve the dynamics of the detachments with the goal of performing a three-dimensional reconstruction of them.

9. Conclusion and outlook

Using the fluorescent pH indicator pyranine, a novel measurement method (Sec. 3.1) based on the boundary layer imaging (BLI) method was realized and verified by conducting invasion experiments with the alkaline trace gas ammonia at the Heidelberg linear wind-wave tunnel. A new chemical system was established by using a high total indicator concentration of $[\mathrm{I}]_{\mathrm{tot}} \simeq 10^{-4}\,\mathrm{M}$ and an initial pH value of ~ 6.

Subsequent measurement series with short gas injections were performed using spectroscopy setups. The results (Sec. 8.1) demonstrate, that a linear regime between the concentrations of the indicator components (IH, I^-) and dissolved ammonia could be accessed. The determined values of the proportionality factor $a_{\mathrm{NH3,I^-}}$ are in agreement with the theoretical estimate $a_{\mathrm{NH3,I^-}} = 0.85$ resulting from calculations (Sec. 3.3). A change of the $\mathrm{pK_a}$ value of pyranine could be excluded as a possible cause of the deviation found for one measurement series. Instead, it was concluded that the condensation of water vapor at the inside of the tunnel walls could lead to a distorted mass balance. It is considered that the effect is favored by the geometry of the used wind-wave tunnel, where the area of the walls is much larger than the area of the water surface ($A_{\mathrm{walls}}/A_{\mathrm{ws}} \sim 20$). To clarify this issue, a similar measurement in a wind-wave tunnel like the *Aeolotron* with a lower ratio of $A_{\mathrm{walls}}/A_{\mathrm{ws}} \sim 5$ could be performed. The described effect is expected to be smaller here.

Furthermore, measurements for different constant ammonia fluxes into the water were performed, where a boundary layer imaging (BLI) and a laser-induced fluorescence (LIF) imaging setup were used in addition to the spectroscopy setups. With these, horizontal images of the fluorescent streaks and vertical fluorescence profiles were acquired with a high temporal and spatial resolution. By means of a simulation (Sec. 5.6), concentration values of the alkaline pyranine I^- component were obtained.

From the recorded images of the BLI cameras (Sec. 8.2.1), concentration values $\overline{[\mathrm{I}^-]}$, averaged along the water column, were inferred pixelwise and used to determine the water-side flux $j_{\mathrm{w,I^-}}$. These values were found to be linear to the air-side ammonia flux $j_{\mathrm{a,NH3}}$, as expected. The proportionality factors $a_{\mathrm{NH3,I^-}}$ between $j_{\mathrm{a,NH3}}$ and $j_{\mathrm{w,I^-}}$ determined for the different BLI cameras were found to be in a range between 0.68 and 0.77. Thus, they are similar to the proportionality factors between the concentrations $[\mathrm{NH_3}]_{\mathrm{w,tot}}$ and $[\mathrm{I}^-]$ obtained from the experiments with short gas injections. It was demonstrated that from the concentration images which show the horizontal distribution of $\overline{[\mathrm{I}^-]}$ a change of the water-side ammonia concentration can be estimated $\Delta\overline{[\mathrm{NH_3}]}_{\mathrm{w,tot}}$. Thus, the developed method provides a first approach to obtain

quantitative information on the local concentration changes of a dissolved gas with a horizontal resolution during a gas exchange experiment.

From the measured fluorescence profiles extracted from the LIF images (Sec. 8.2.2), concentration depth profiles $[I^-](z)$ were determined to estimate the boundary layer thickness and the concentration gradient at the water surface. Moreover, detachment events characterized by a gradual increase and a rapid drop of the boundary layer thickness were observed. By enhancing the evaluation algorithm, the recorded data can be used to study typical time constants of these events which are expected to be related to the surface renewal rate. Furthermore, the position and the orientation of the detected fluorescence profile were used to infer the displacement and the slope of the water surface at the observed spot.

With the bottom BLI cameras, stereo vision was realized and it was shown that depth information can be extracted (Sec. 8.2.3). The recorded images can be reviewed to study, if the visible turbulent structures can be assigned to different water depths. Moreover, it can be tested if the observation of detachments from the boundary layer is feasible with the BLI cameras. With the results from the LIF images, the required depth resolution was estimated to be 10 px/mm.

With the developed method, turbulent structures close to the water surface are made visible locally by fluorescence during a gas exchange experiment. At the same time, the imaged fluorescence intensity can be used to obtain information on the concentration of the trace gas. The combination of these two aspects makes the new method a powerful tool to investigate gas exchange processes. The results and findings of this thesis can be used to employ the new method for future experiments at different wind speeds and in different wind-wave tunnels. More importantly, the first steps that were taken in this thesis concerning the observation of detachments from the boundary layer can serve as a starting point to perform measurements with a large array of cameras. This would give the perspective for a three-dimensional reconstruction of the turbulent structures to gain more insights in the local dynamics of gas exchange.

Bibliography

[Cheng et al., 2006] Cheng, B.-M., Lu, H.-C., Chen, H.-K., Bahou, M., Lee, Y.-P., Mebel, A. M., Lee, L. C., Liang, M.-C., and Yung, Y. L. (2006). Absorption cross sections of NH_3, NH_2D, NHD_2, and ND_3 in the spectral range 140–220 nm and implications for planetary isotopic fractionation. *The Astrophysical Journal*, 647(2):1535–1542. DOI: https://doi.org/10.1086/505615.

[Clegg and Brimblecombe, 1989] Clegg, S. and Brimblecombe, P. (1989). Solubility of ammonia in pure aqueous and multicomponent solutions. *Journal of Physical Chemistry*, 93:7237–7248. DOI: https://doi.org/10.1021/j100357a041.

[Cussler, 2009] Cussler, E. L. (2009). *Diffusion - Mass Transfer in Fluid Systems*. Cambridge University Press, Cambridge, 3 edition.

[Danckwerts, 1951] Danckwerts, P. V. (1951). Significance of a liquid-film coefficients in gas absorption. *Ind. Eng. Chem.*, 43:1460–1467. DOI: https://doi.org/10.1021/ie50498a055.

[Deacon, 1977] Deacon, E. L. (1977). Gas transfer to and across an air-water interface. 29:363–374. DOI: https://doi.org/10.3402/tellusa.v29i4.11368.

[Degreif, 2006] Degreif, K. (2006). *Untersuchungen zum Gasaustausch - Entwicklung und Applikation eines zeitlich aufgelösten Massenbilanzverfahrens*. Dissertation, Institut für Umweltphysik, Fakultät für Physik und Astronomie, Univ. Heidelberg. DOI: https://doi.org/10.11588/heidok.00006120.

[Donelan and Wanninkhof, 2002] Donelan, M. A. and Wanninkhof, R. (2002). Gas transfer at water surfaces - conepts and issues. In Donelan, M. A., Drennan, W. M., Saltzman, E. S., and Wanninkhof, R., editors, *Gas Transfer at Water Surfaces*, pages 1–10. American Geophysical Union. DOI: https://doi.org/10.1029/GM127p0001.

[Fick, 1855] Fick, A. E. (1855). Über Diffusion. *Annalen der Physik*, 170:59–86. DOI: https://doi.org/10.1002/andp.18551700105.

[Fogg and Sangster, 2003] Fogg, P. G. T. and Sangster, J. (2003). *Chemicals in the Atmosphere: Solubility, Sources, and Reactivity*. Wiley, Chichester.

[Friedl, 2013] Friedl, F. (2013). *Investigating the Transfer of Oxygen at the Wavy Air-Water Interface under Wind-Induced Turbulence*. Dissertation, Institut für Umweltphysik, Fakultät für Physik und Astronomie, Univ. Heidelberg. DOI: https://doi.org/10.11588/heidok.00014582.

[Hales and Drewes, 1979] Hales, J. M. and Drewes, D. R. (1979). Solubility of ammonia in water at low concentrations. *Atmospheric Environment*, 13:1133–1147. DOI: https://doi.org/10.1016/0004-6981(79)90037-4.

[Harned and Davis, 1943] Harned, H. S. and Davis, R. (1943). The ionization constant of carbonic acid in water and the solubility of carbon dioxide in water and aqueous salt solutions from 0 to 50°. *Journal of the American Chemical Society*, 65(10):2030–2037. DOI: https://doi.org/10.1021/ja01250a059.

[Harned and Scholes, 1941] Harned, H. S. and Scholes, S. R. (1941). The ionization constant of HCO_3^- from 0 to 50°. *Journal of the American Chemical Society*, 63(6):1706–1709. DOI: https://doi.org/10.1021/ja01851a058.

[Herzog, 2010] Herzog, A. (2010). *Imaging of Water-sided Gas-Concentration Fields at a Wind-Driven, Wavy Air-Water Interface*. Dissertation, Institut für Umweltphysik, Fakultät für Physik und Astronomie, Univ. Heidelberg. DOI: https://doi.org/10.11588/heidok.00011220.

[Higbie, 1935] Higbie, R. (1935). The rate of absorption of a pure gas into a still liquid during short periods of exposure. *Trans. Am. Inst. Chem. Eng.*, 31:365–389.

[Jähne and Haußecker, 1998] Jähne, B. and Haußecker, H. (1998). Air-water gas exchange. *Annu. Rev. Fluid Mech.*, 30:443–468. DOI: https://doi.org/10.1146/annurev.fluid.30.1.443.

[Jessup et al., 1997] Jessup, A. T., Zappa, C. J., and Yeh, H. H. (1997). Defining and quantifying microscale wave breaking with infrared imagery. 102(C10):23145–23153. DOI: https://doi.org/10.1029/97JC01449.

[Jähne, 1980] Jähne, B. (1980). *Zur Parametrisierung des Gasaustauschs mit Hilfe von Laborexperimenten*. Dissertation, Institut für Umweltphysik, Fakultät für Physik und Astronomie, Univ. Heidelberg. DOI: https://doi.org/10.11588/heidok.00016796.

[Jähne, 1985] Jähne, B. (1985). *Transfer processes across the free water interface*. Habilitation thesis, Institut für Umweltphysik, Fakultät für Physik und Astronomie, Univ. Heidelberg. DOI: https://doi.org/10.11588/heidok.00016798.

[Jähne, 2012] Jähne, B. (2012). *Digitale Bildverarbeitung und Bildgewinnung*. Springer.

[Jähne, 2013] Jähne, B. (2013). Compression by noise equalization. zenodo. DOI: https://doi.org/10.5072/zenodo.12761.

[Jähne et al., 1984] Jähne, B., Huber, W., Dutzi, A., Wais, T., and Ilmberger, J. (1984). Wind/wave-tunnel experiments on the schmidt number and wave field dependence of air-water gas exchange. In Brutsaert, W. and Jirka, G. H., editors, *Gas transfer at water surfaces*, pages 303–309, Hingham, MA. Reidel. DOI: https://doi.org/10.1007/978-94-017-1660-4_28.

[Jähne et al., 1989] Jähne, B., Libner, P., Fischer, R., Billen, T., and Plate, E. J. (1989). Investigating the transfer processes across the free aqueous viscous boundary layer by the controlled flux method. 41B(2):177–195. DOI: https://doi.org/10.1111/j.1600-0889.1989.tb00135.x.

[Jähne et al., 1987] Jähne, B., Münnich, K. O., Bösinger, R., Dutzi, A., Huber, W., and Libner, P. (1987). On the parameters influencing air-water gas exchange. 92:1937–1950. DOI: https://doi.org/10.1029/JC092iC02p01937.

[Karastogianni et al., 2016] Karastogianni, S., Girousi, S., and Sotiropoulos, S. (2016). pH: Principles and measurement. *Encyclopedia of Food and Health*. DOI: https://doi.org/10.1016/B978-0-12-384947-2.00538-9.

[Kiefhaber et al., 2014] Kiefhaber, D., Reith, S., Rocholz, R., and Jähne, B. (2014). High-speed imaging of short wind waves by shape from refraction. 9:14015. DOI: https://doi.org/10.2971/jeos.2014.14015.

[Klein, 2019] Klein, A. (2019). *The fetch dependency of small-scale air-sea interaction processes at low to moderate wind speeds*. PhD thesis, Institut für Umweltphysik, Fakultät für Physik und Astronomie, Univ. Heidelberg. DOI: https://doi.org/10.11588/heidok.00026559.

[Kolmogorov, 1941] Kolmogorov, A. N. (1941). The local structure of turbulence in incompressible viscous fluid for very large Reynolds numbers. *Compt.Rend.Akad.Nauk SSSR*, 30:301. URL: https://www.jstor.org/stable/51980.

[Kolmogorov, 1962] Kolmogorov, A. N. (1962). A refinement of previous hypotheses concerning the local structure of turbulence in a viscous incompressible fluid at high reynolds number. *Journal of Fluid Mechanics*, 13:82–85. DOI: https://doi.org/10.1017/S0022112062000518.

[Krall, 2013] Krall, K. E. (2013). *Laboratory Investigations of Air-Sea Gas Transfer under a Wide Range of Water Surface Conditions*. Dissertation, Institut für

Umweltphysik, Fakultät für Physik und Astronomie, Univ. Heidelberg. DOI: https://doi.org/10.11588/heidok.00014392.

[Kräuter, 2015] Kräuter, C. (2015). *Visualization of air-water gas exchange*. Dissertation, Institut für Umweltphysik, Fakultät für Physik und Astronomie, Univ. Heidelberg. DOI: https://doi.org/10.11588/heidok.00018209.

[Kräuter et al., 2014] Kräuter, C., Trofimova, D., Kiefhaber, D., Krah, N., and Jähne, B. (2014). High resolution 2-D fluorescence imaging of the mass boundary layer thickness at free water surfaces. 9:14016. DOI: https://doi.org/10.2971/jeos.2014.14016.

[Kundu et al., 2012] Kundu, P., Cohen, I., and Dowling, D. (2012). *Fluid Mechanics*. Elsevier Science.

[Lakowicz, 2006] Lakowicz, J. R. (2006). *Principles of Fluorescence Spectroscopy*. Springer, 3. edition.

[Lamont and Scott, 1970] Lamont, J. C. and Scott, J. C. (1970). An eddy cell model of mass transfer into the surface of a turbulent liquid. *AIChE Journal*, 16:513–519. DOI: https://doi.org/10.1002/aic.690160403.

[Langmuir, 1938] Langmuir (1938). Surface motion of water induced by wind. *Science*, 87:119–124.

[Lide and Frederikse, 1995] Lide, D. R. and Frederikse, H. P. R. (1995). *CRC Handbook of Chemistry and Physics*. CRC Press, Inc. Boca Raton , FL.

[Mesarchaki et al., 2014] Mesarchaki, E., Kräuter, C., Krall, K. E., Bopp, M., Helleis, F., Williams, J., and Jähne, B. (2014). Measuring air-sea gas exchange velocities in a large scale annular wind-wave tank. 11:1643–1689. DOI: https://doi.org/10.5194/osd-11-1643-2014.

[Mischler et al., 2015] Mischler, W., Krall, K. E., and Jähne, B. (2015). Experimental studies of the parameters controlling bubble-induced air-sea gas exchange. In *7th International Symposium on Gas Transfer at Water Surfaces, Seattle, May 18–21, 2015*. abstract, accepted as poster. DOI: https://doi.org/10.5281/zenodo.17671.

[Motch et al., 2006] Motch, C., Giuliani, A., Delwiche, J., Limão-Vieira, P., Mason, N., Hoffmann, S., and Hubin-Franskin, M.-J. (2006). Electronic structure of hexafluorobenzene by high-resolution vacuum ultraviolet photo-absorption and He(I) photoelectron spectroscopy. *Chemical Physics*, 328(1):183 – 189. DOI: https://doi.org/10.1016/j.chemphys.2006.05.032.

[Myhre, 2013] Myhre, G. e. a. (2013). *Anthropogenic and natural radiative forcing, in: Climate Change 2013: The Physical Science Basis. Contribution of Working Group I to the Fifth Assessment Report of the Intergovernmental Panel on Climate Change*. Cambridge University Press, Cambridge, United Kingdom and New York, NY, USA. DOI: https://doi.org/10.1017/CBO9781107415324.018.

[Pearson, 1905] Pearson, K. (1905). The problem of the random walk. *Nature*, 72(294). DOI: https://doi.org/10.1038/072342a0.

[Perez-Urquiza and Beltran, 2001] Perez-Urquiza, M. and Beltran, J. L. (2001). Determination of the dissociation constants of sulfonated azo dyes by capillary zone electrophoresis and spectrophotometry methods. *J. Chromatogr. A*, 917:331–336. DOI: https://doi.org/10.1016/S0021-9673(01)00707-5.

[Platt et al., 1979] Platt, U., Perner, D., and Pätz, H. W. (1979). Simultaneous measurement of atmospheric CH_2O, O_3, and NO_2 by differential optical absorption. 84:6329–6335. DOI: https://doi.org/10.1029/JC084iC10p06329.

[Pope, 2009] Pope, S. B. (2009). *Turbulent Flows*. Cambridge University Press, 6 edition.

[Prandtl, 1957] Prandtl, L. (1957). *Strömungslehre*. Vieweg.

[Reichardt, 1951] Reichardt, H. (1951). Vollständige Darstellung der turbulenten Geschwindigkeitsverteilung in glatten Leitungen. *Zeitschrift für angewandte Mathematik und Mechanik*, 31:208–219. DOI: https://doi.org/10.1002/zamm.19510310704.

[Richmond and Wolanski, 2011] Richmond, R. H. and Wolanski, E. (2011). *Coral Research: Past Efforts and Future Horizons*, pages 3–10. Springer Netherlands, Dordrecht.

[Riedel and Janiak, 2011] Riedel, E. and Janiak, C. (2011). *Anorganische Chemie*. De Gruyter.

[Roedel, 2000] Roedel, W. (2000). *Physik unserer Umwelt: die Atmosphäre*. Springer-Verlag, 3 edition.

[Sander, 2015] Sander, R. (2015). Compilation of henry's law constants (version 4.0) for water as solvent. *Atmospheric Chemistry and Physics*, 15(8):4399–4981. DOI: https://doi.org/10.5194/acp-15-4399-2015.

[Schimpf, 2000] Schimpf, U. (2000). *Untersuchung des Gasaustausches und der Mikroturbulenz an der Meeresoberfläche mittels Thermographie*. Dissertation, Institut

für Umweltphysik, Fakultät für Physik und Astronomie, Univ. Heidelberg, Heidelberg, Germany. DOI: https://doi.org/10.11588/heidok.00000545.

[Shi et al., 1999] Shi, Q., Davidovits, P., Jayne, J., Worsnop, D., and E., K. C. (1999). Uptake of gas-phase ammonia. 1. uptake by aqueous surfaces as a function of ph. *Journal of Physical Chemistry A*, 103:8812–8823. DOI: https://doi.org/10.1021/jp991696p.

[Sonntag, 1990] Sonntag, D. (1990). Important new values of the physical constants of 1986, vapour pressure formulations based on its-90, and psychrometer formulae. *Zeitschrift für Meteorologie*, Bd. 40(Nr. 5):S. 340–344.

[Stokes, 1850] Stokes, G. (1850). *On the effect of the internal friction of fluids on the motion of pendulums*, volume 9. Transactions of the Cambridge Philosophical Society.

[T. Ho et al., 2011] T. Ho, D., Wanninkhof, R., Schlosser, P., Ullman, D., Hebert, D., and F. Sullivan, K. (2011). Towards a universal relationship between wind speed and gas exchange: Gas transfer velocities measured wit $^3H/SF_6$ during the southern ocean gas exchange experiment. *Journal of Geophysical Research*, 116. DOI: https://doi.org/10.1029/2010JC006854.

[Thorpe, 2004] Thorpe, S. A. (2004). Langmuir circulation. 36(1):55–79. DOI: https://doi.org/10.1146/annurev.fluid.36.052203.071431.

[Tsai et al., 2005] Tsai, W.-T., Chen, S.-M., and Moeng, C.-H. (2005). A numerical study on the evolution and structure of a stress-driven, free-surface turbulent shear flow. 545:163–192. DOI: https://doi.org/10.1017/S0022112005007044.

[Walker and Peirson, 2008] Walker, J. W. and Peirson, W. L. (2008). Measurement of gas transfer across wind-forced wavy air–water interfaces using laser-induced fluorescence. 44:249–259. DOI: https://doi.org/10.1007/s00348-007-0398-8.

[Wallace and Hobbs, 1977] Wallace, J. M. and Hobbs, P. V. (1977). *Atmospheric Science: An Introductory Survey*. Academic Press.

[Wanninkhof et al., 2009] Wanninkhof, R., Asher, W., T Ho, D., Sweeney, C., and R McGillis, W. (2009). Advances in quantifying air-sea gas exchange and environmental forcing*. *Annual review of marine science*, 1:213–44. DOI: https://doi.org/10.1146/annurev.marine.010908.163742.

[Whitman, 1923] Whitman, W. G. (1923). The two-film theory of gas absorption. *Chemical and Metallurgical Engineering*, 29(4):146–148. DOI: https://doi.org/10.1016/0017-9310(62)90032-7.

[Wolfbeis et al., 1983] Wolfbeis, O. S., Fürlinger, E., Kroneis, H., and Marsoner, H. (1983). Fluorimetric analysis 1. a study on fluorescent indicators for measuring near neutral ("physiological") pH-values. *Fresenius Z. Anal Chem*, 314:119–124. DOI: https://doi.org/10.1007/BF00482235.

[Wolfbeis and Posch, 1986] Wolfbeis, S. and Posch, E. (1986). Fibre-optic fluorescing sensor for ammonia. *Analytica Chimica Acta*, 185:321–327. DOI: https://doi.org/10.1016/0003-2670(86)80060-5.

[Xia et al., 1998] Xia, P., Bungay, P. M., Gibson, C. C., Kovbasnjuk, O. N., and Spring, K. R. (1998). Diffusion coefficients in the lateral intercellular spaces of madin-darby canine kidney cell epithelium determined with caged compounds. *Biophysical Journal*, 74(6):3302 – 3312. DOI: https://doi.org/10.1016/S0006-3495(98)78037-3.

[Yaws, 1999] Yaws, C. L. (1999). *Chemical Properties Handbook: physical, thermodynamic, environmental, transport, safety, and health related properties for organic and inorganic chemicals*. McGraw-Hill.

[Zeebe and Wolf-Gladrow, 2001] Zeebe, R. E. and Wolf-Gladrow, D. A. (2001). CO_2 *in seawater: equilibrium, kinetics, isotopes*, volume 65 of *Elsevier Oceanography Series*. Elsevier, Amsterdam.

A. Appendix

A.1 Spectrophotometer

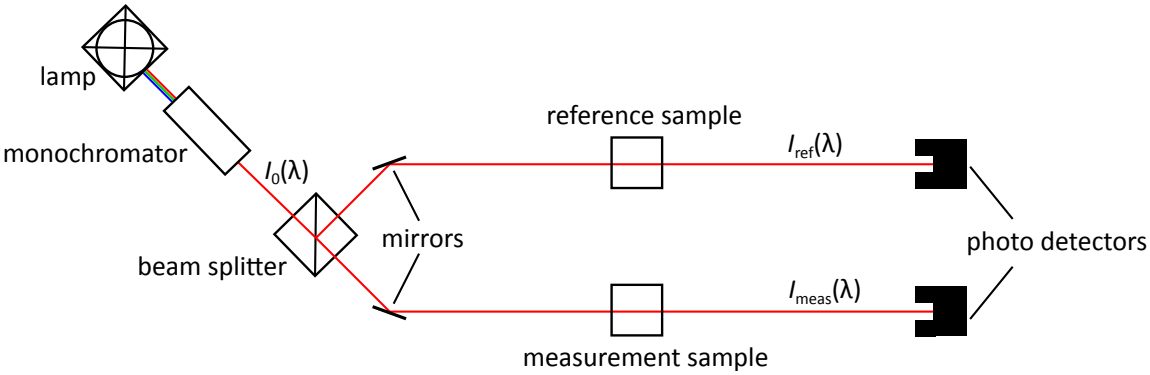

Fig. A.1: Schematic illustration of a two beam spectrophotometer as used in the scope of this thesis for preliminary absorption measurements of the dyes and optical filters. Its functional principle is explained in the text.

To measure absorbance spectra of pyranine and tartrazine as well as the transmission of optical filters, a two beam spectrophotometer (*UV-2700* by *Shimadzu*) was used. With such an instrument, schematically shown in Fig. A.1, high-precision absorption measurements can be performed. Its functional principle is explained in the following.

Light of the broadband light source (typically a halogen lamp) enters the monochromator which allows only light $I_0(\lambda)$ of a certain wavelength to pass through. The beam is then split into a reference and a measurement beam. The beams pass the reference and the measurement sample in the measurement compartments, respectively. The transmitted intensities $I_{\mathrm{ref}}(\lambda)$ and $I_{\mathrm{meas}}(\lambda)$ are measured by photo detectors. In this way the absorbance of the measurement sample is directly measured with respect to the reference sample according to

$$A(\lambda) = -\lg(I_{\mathrm{meas}}(\lambda)/I_{\mathrm{ref}}(\lambda)), \tag{A.1}$$

with the decadic logarithm lg. In this way, changes of the lamp spectrum are automatically corrected for. To acquire the whole absorbance spectrum, the monochromator performs a wavelength sweep within the set range.

Danksagung

An dieser Stelle möchte ich allen Personen danken, die zum Gelingen dieser Arbeit beigetragen haben.

Mein besonderer Dank gilt Prof. Bernd Jähne für die Ermöglichung und Betreuung eines so interessanten und interdisziplinären Projektes. Danke für die vielen inspirierenden Anregungen und die Freiräume.

Ebenfalls bedanke ich mich bei Prof. Werner Aeschbach für die Erstellung des Zweitgutachtens für diese Arbeit.

Bei der gesamten Windkanal Arbeitsgruppe bedanke ich mich für den hilfsbereiten Umgang untereinander sowie die positive Arbeitsatmosphäre.

Im Einzelnen danke ich Kerstin Krall für die Beantwortung unterschiedlichster Fragen und ihre Fähigkeit, alles im Labor zu finden. Außerdem danke ich ihr sowie Günther Balschbach für das Korrekturlesen dieser Arbeit. Maximilian Bopp für seine hilfreichen Anregungen und die tatkräftige Unterstützung, Angelika Klein für die Unterstützung in der Anfangszeit und Sonja Friman für das Korrekturlesen, Ratschläge und das stete Interesse an meiner Arbeit. Philipp Voigt für einige interessante und unterhaltsame Gespräche.

Zuletzt möchte ich meiner Familie für die uneingeschränkte Unterstützung danken, auf die ich mich zu jeder Zeit des Studiums verlassen konnte.

Ich versichere, dass ich diese Arbeit selbständig verfasst und keine anderen als die angegeben Quellen und Hilfsmittel benutzt habe.

Heidelberg, den 14. Oktober 2019 .....

(Maximilian Papst)